Real-Time Tracking of Atomic Electron Dynamics

vorgelegt von
M.Sc. Mursal Baggash
geboren in Taiz, Jemen

Von der Fakultät II - Mathematik und Naturwissenschaften -
der Technischen Universität Berlin
zur Erlangung des akademischen Grades

Doktor der Naturwissenschaften
- Dr. rer. nat. -

genehmigte Dissertation

Promotionsausschuss:

Vorsitzende: Prof. Dr. Janina Maultzsch
Gutachterin: Prof. Dr. Maria Krikunova
Gutachter: Prof. Dr. Emad Aziz
Gutachter: Dr. Horst Rottke

Tag der wissenschaftlichen Aussprache: 15.08.2016

Berlin 2016

Contents

Zusammenfassung

In dieser Arbeit wird die zeitliche Entwicklung korrelierter Elektronendynamik in elektronischen Wellenpaketen im Ionisationskontinuum von Atomen dargestellt. Das Wellenpaket wird durch Absorption von extrem ultravioletten (XUV) Lichtpulsen durch Atome im Grundzustand gestartet. Diese XUV Pulse werden mittels hoher harmonischer Erzeugung, ausgehend von ultra-kurzen infraroten (IR) Laserpulsen, gebildet. Die zeitliche Entwicklung der Wellenpakete wird verfolgt, indem man mit einem schwachen IR Laserpuls mit variabler Zeitverzögerung einen Kontinuum-Kontinuum Übergang induziert wird. Diese Photoelektronen werden dann unter Verwendung eines Elektronenspektrometers, das auf dem Prinzip einer magnetischen Flasche basiert, nachgewiesen.

Der erste Teil dieser Arbeit (Kapitel 4) stellt experimentelle Ergebnisse zur Zweielektronendynamik in Wellenpaketen im Ionisationskontinuum des Xenonatoms dar. Dieses Experiment verwendet hohe harmonische Pulse, um Wellenpakete in einem Energiebereich zu starten, der durch Fano-Resonanzen strukturiert ist. Zu diesen Wellenpaketen tragen mehr als zwei Fano-Resonanzen bei. Die zeitliche Entwicklung dieser Wellenpakete wird mit einem schwachen IR Impuls mit variabler Verzögerungszeit zum XUV Puls getestet. Die mit den angeregten Fano-Resonanzen zusammenhängende Zweielektronendynamik, die der Zeitentwicklung der Wellenpakete eine Oszillationsstruktur aufprägt, zerfällt durch Autoionisation. Die Abhängigkeit der Photoelektronenausbeute von der Verzögerungszeit der Probe- (IR Pulse) zu den Pump-Pulsen (XUV Pulse) wird theoretisch durch eine Zweiphotonenübergangswahrscheinlichkeit beschrieben, die auf der Grundlage von Fano's Theorie abgeleitet wird.

Der zweite Teil dieser Arbeit (Kapitel 5) verwendet die RABBITT-Technik (reconstruction of attosecond beating by interference of two-photon transitions), um mögliche RABBITT-Phasendifferenzen zwischen den Ionisationskanälen $^2P_{1/2}$ und $^2P_{3/2}$ von Kryptonatomen zu untersuchen. Die Phasendifferenzen werden für Anregungsenergien zwischen $\approx 18\,\mathrm{eV}$ und $\approx 29\,\mathrm{eV}$ vermessen. Sie hängen kritisch von der kinetischen Energie der Photoelektronen ab, insbesondere im unteren Energiebereich. Sie zeigen ebenfalls eine signifikante Abhängigkeit von den linearen Polarisationsrichtungen der XUV-Pump- und IR-Probepulse relativ zueinander. Die experimentell bestimmten Phasendifferenzen werden mit berechneten verglichen, die auf Dipolmatrixelementen für die Photoionisation und Streuphasen für Elektronenstreuung beruhen, die für Krypton aus vorhergehenden Experimenten bekannt sind. Die Ergebnisse zeigen, dass gemessene RABBITT-Phasendifferenzen für Krypton keinen direkten Zugriff auf Zeitverzögerungen in der Photoemission im primären Photoionisationsschritt des Atoms erlauben.

Abstract

This thesis presents real-time observations of correlated electron dynamics in electronic wavepackets in the continuum energy range of atoms. The atomic electron dynamics is initiated by extreme ultraviolet (XUV) light pulses generated by high harmonic generation (HHG). Its evolution in time is probed by inducing a continuum-continuum transition with delayed weak infrared (IR) pulses. The photoelectrons which have interacted with the IR pulses are then detected using a magnetic bottle electron spectrometer.

The first part of this thesis (Chapter 4) presents experimental results of real-time tracking of two-electron dynamics in electronic wavepackets in the ionization continuum of the xenon atom. This experiment utilizes harmonic XUV pulses from a generated harmonic pulse train to launch electronic wavepackets in an energy range structured by Fano resonances. The launched wavepackets encompass more than two Fano resonances. The evolution in time of these wavepackets is probed with a weak IR pulse at a controllable delay time between the XUV and IR pulses. Coherent two-electron dynamics appears in the time evolution of the wavepackets as an oscillatory beating imprinted on their autoionization decay. The dependence of the measured photoelectron yields on the pump-probe delay time is analyzed by using a two-photon transition probability derived on the basis of Fano's theory.

In the second part of this thesis (Chapters 5) the RABBITT (reconstruction of attosecond beating by interference of two photon transitions) technique is used to investigate a continuum energy dependent RABBITT phase difference in the ionization channels $^2P_{1/2}$ and $^2P_{3/2}$ of krypton atoms. The phase difference is investigated for excitation energies ranging between $\approx 18\,\mathrm{eV}$ and $\approx 29\,\mathrm{eV}$. The measured phase difference critically depends on the photoelectron kinetic energy, specifically in the lower energy range. It also shows a significant dependence on the relative directions of linear polarization of the XUV-pump and IR-probe pulses with respect to each other. The experimental phase differences are compared with those obtained from calculations based on dipole matrix elements for photoionization and scattering phase shifts known for krypton from previous experiments. The results indicate that the RABBITT phase differences for krypton can not map directly time-delay differences which may appear in the photoionization step of the atom.

Parts of this thesis have been published in the following articles:

- M. Baggash and H. Rottke. „Real-time tracking of two-electron dynamics in the ionization continuum of Xe“. In: *Phys. Rev. A.* 91 (2015), Page 053403.
- M. Baggash and H. Rottke. „Phase differences in the photoemission from krypton in the fine-structure-split ionization channels $^2P_{3/2}$ and $^2P_{1/2}$ “. In: *Phys. Rev. A.* 92 (2015), Page 013424.

1 Introduction

Development of scientific and practical applications in biology, chemistry and physics rely mainly on a complete comprehension of the atomic and molecular structure. This structure is usually explored by spectroscopic analysis of the interaction of the atomic or molecular sample with light. The point in this interaction that links these three scientific fields is the microscopic motion of electrons in atoms and molecules [1, 2, 3, 4]. Investigating their dynamical behavior is necessary for understanding the atomic and molecular structure and explaining light-matter interaction as well. Electron motion explains coherent light emission from atoms, for instance: specific electron motion is responsible for the emission of extreme ultraviolet (XUV) light pulses following the interaction of an atom with intense femtosecond laser pulses [5]. In biology and chemistry the study of electron dynamics is of great importance for understanding and tracking the course of biological and chemical reactions. An example in this direction are the achievements of Ahmed A. Zewail, who was able to resolve chemical reactions on the femtosecond time scale which earned him the Nobel prize in chemistry in 1999 [6]. Electron dynamics in atoms occurs on an ultrafast attosecond time scale (as) ($1\,\mathrm{as} = 10^{-18}\,\mathrm{s}$). It takes an electron in a hydrogen atom 150 as to complete one period on its orbit. Since there is no existing camera able to photographically track such an ultrafast dynamics, it is only possible to track the electron motion with a so called pump-probe technique [6, 3]. This technique utilizes a light pulse (pump pulse) to initiate the electron dynamics of interest in an atomic or molecular system and a second light pulse (probe pulse) to probe the system at a controllable delay time with respect to the initiation time. Probing the system dynamics at several values of the time delay resolves the electron motion in the time domain and produces a movie of its dynamics.

The emergence of high-intensity femtosecond laser pulses and their nonlinear interaction with matter have led to the advent of attosecond light pulses. These attosecond light pulses are produced by high harmonic generation (HHG) via an interaction of the high-intensity laser pulses with a nonlinear medium [7, 8]. HHG became a main source of ultrashort pulses of carrier frequency in the extreme ultraviolet and soft X-ray spectral regions with a high degree of coherence. Free electron lasers (FEL) represent an alternative XUV and X-ray light source. While free electron lasers allow only very limited access for researchers, HHG is relatively easy to implement in laboratories and its output XUV light pulses represent a powerful tool for directly tracking ultrafast dynamics in the time domain [1, 2].

The work presented in this thesis employs XUV light pulses produced by HHG with a temporal width of sub-30 fs and a bandwidth, limited by this temporal duration, of about 100 meV to launch electron dynamics in atoms. The evolution of this dynamics in time is tracked by inducing a subsequent probe-transition with a weak infrared (IR) laser pulse at an arbitrary delay time. One issue investigated concerned the real time tracking of an electronic wavepacket in the ionization continuum in a spectral range structured by Fano resonances. The Fano resonances that were involved can be attributed

to either two-valence-electron excited states of the atom or to single inner-valence-electron excited states. The dynamics of an electron wavepacket launched in such an energy range therefore usually involves fast relaxation, i. e. autoionization due to electron-electron interaction and correlation effects. Besides this the evolution in time of the wavepacket may give information on the discrete excited electron configurations embedded in the ionization continuum and on a possible residual interaction among them. These discrete configurations represent either two-valence-electron or one-inner-valence-electron excited configurations. Electron-electron interaction and correlation effects are of major interest, not only in physics, but also in understanding fundamental chemical reactions, condensed matter and charge transfer in biological systems. In an atomic system, investigation of electron-electron interaction and correlation effects leads to a detailed understanding of its energy level structure and of the corresponding eigenstates of the Hamilton operator [9].

Several previous experimental investigations of electron dynamics in the photoionization continuum of many-electron atoms in real time have been done [4, 3, 10]. For example, Auger decay in xenon atoms after photoionization of an inner-shell electron has been experimentally investigated in [3]. Another experimental work in this direction has been done in our group and published in [9]. In this work an interference between one- and two-electron excitation channels in an excited wavepacket in the krypton atom appeared as an oscillation of the photoelectron yield in a pump-probe experiment superimposed on the wavepacket's autoionization decay during its evolution in time. The work presented here aims at extending this to real-time tracking of coherent electron dynamics in electronic wavepackets that involve more than two excitation channels.

Another exciting topic, which is investigated in this work, is the electron temporal dynamics in photoemission from atoms. This Wigner-time-delay difference in the emission of photoelectron wavepackets formed in photoionization from different atomic subshells has been experimentally observed by employing XUV harmonic and infrared (IR) pulses in a pump-probe experiment [4, 3, 11, 12]. The Wigner-time delay in photoemission is related to the first energy derivative of the phase acquired by an electron which scatters off a Coulomb potential of a positively charged ionic core. The investigations, which intend to measure a time delay in photoemission, mainly have used either a streaking technique [13] or the reconstruction of attosecond beating by interference of two-photon transitions (RABBITT) technique [14]. For the noble gases neon [4] and argon [11, 15, 12], these experimental techniques indicate an emission time-delay difference for photoelectrons emitted from the np and ns valence orbitals, with $n = 2$ for Ne and $n = 3$ for Ar, respectively. The experiments based on the RABBITT technique [11] have to assume that the photoelectron leaves the ion core predominantly in one partial wave channel to be able to extract the Wigner time delay in photoemission for just this partial wave channel. This however may be questionable for the noble gases. Therefore, a second goal of this thesis is the experimental investigation of the effect of photoemission in two partial wave channels on the outcome of a RABBITT experiment. The noble gas krypton allows this investigation by photoionization of an electron in the $4p$-valence orbital. In this case s- and d-partial waves contribute to the photoelectron wavepacket. RABBITT time delay differences can then be determined between ionization channels where the ion core is left in the $^2P_{1/2}$ and $^2P_{3/2}$ states.

Chapter 2 of this thesis presents a short review of the theoretical background related

to the interaction of an atom with intense laser pulses as far as it is necessary to understand HHG. For most of the strong field physical phenomena the reader is referred to related articles and text books where they are amply explained. The phenomenon of high harmonic generation is described based on the three step classical model (re-scattering model) as well as on a quantum mechanical model. Attention is paid here to spectral and temporal properties of the generated harmonic pulses and to the optimization of the conversion efficiency by manipulating phase matching conditions. Apart from HHG, all intensities of the light pulses used in the experiments are low enough to describe their interaction with atoms by perturbation theory which is briefly reviewed at end of this chapter.

The experimental setup used for data acquisition in all experiments is described in chapter 3. In addition to the femtosecond laser system used for HHG and for the probe pulses this setup consists of mainly four parts. The first one is a beamsplitter and delay stage unit. In this part of the setup the main laser beam is split into two parts one of which carries most of the beam power used for HHG while the weak second beam serves as a probe pulse. The second part consists of a HHG chamber where high harmonics of the fundamental laser frequency are generated. In the third part only the generated high harmonic pulse train and the weak IR probe beam pass a filter chamber while the laser beam used for HHG is blocked. The chamber, where the target gas is ionized, and the magnetic bottle electron spectrometer constitute the fourth part of the setup and are described at the end of this chapter.

Chapter 4 presents experimental results of real-time tracking of the time evolution of electronic wavepackets in the xenon atom. In this experiment the 15^{th} and 17^{th} harmonics XUV pulses from the generated harmonic pulse train are used to launch electronic wavepackets in an energy range structured by Fano resonance. Both wavepackets encompass more than two Fano resonances. The evolution in time of these wavepackets is probed at discrete delay times with a low-intensity IR pulse. The time evolution of both wavepackets shows coherent two-electron dynamics appearing as an oscillatory beating imprinted on their autoionization decay. In the analysis of these oscillations, Fano resonances contributing to the wavepackets are assigned and the life time (line width) of the most populated resonance in each wavepacket is determined.

Chapters 5 employs the RABBITT technique [14] to measure a continuum energy dependent phase difference in the fine-structure-split ionization channels $^2P_{1/2}$ and $^2P_{3/2}$ of krypton atoms, i. e. when one electron is removed from the valence $4p$ orbital of the atom. The phase difference is investigated for excitation energies between $\approx 18\,\text{eV}$ and $\approx 29\,\text{eV}$. It is found to sensitively depend on the photoelectron kinetic energy, specifically in the lower energy range close to the ionization threshold. Additionally, it shows a significant dependence on the relative directions of linear polarization of the XUV-pump and IR-probe pulses (i. e. whether they are perpendicular or parallel to each other). The experimental phase differences are compared with calculated ones using dipole matrix elements for photoionization and scattering phase shifts known for krypton from previous experiments. The theoretical analysis shows that the non-zero measured RABBITT time delay differences arise from the presence of two photoelectron partial waves ($l = 0, 2$) reached upon the bound-continuum transition. The two partial waves have differing scattering phase shifts and participate in different ways in the following continuum-continuum transition.

2 Theoretical Background: Atoms in Strong Laser Fields

Light-matter interaction is a main tool in understanding and developing many applications in different fields. Laser-atom interaction forms the fundamental building block for light-matter interaction. Pulsed lasers that deliver pulses with a duration down to few femtoseconds and focused intensities of up to $10^{16}\,\mathrm{W/cm^2}$, corresponding to an electric field strength comparable to the interatomic field ($5.1 \times 10^9\,\mathrm{V/m}$), are routine in laser laboratories. Atoms subjected to such an electric field respond non-perturbatively and get immediately ionized even if the photon energy is much less than the energy required for ionization. However, the way the electron leaves the atom depends on the frequency and the intensity of the driving laser field. Two limiting cases may be distinguished by the Keldysh parameter [16]

$$\gamma = \sqrt{\frac{I_P}{2\,U_P}}, \tag{2.1}$$

where I_P is the ionization potential of the atom and U_P the cycle-averaged kinetic energy gained by a free electron in an oscillating electric field (ponderomotive energy). While $\gamma \gg 1$ characterizes the regime of multiphoton ionization (MPI), a tunneling ionization model is applicable for the opposite case. Figures 2.1 and 2.2**(a)** show schematic views of strong field ionization in both MPI and tunneling regimes, respectively. In the first case: a bound electron absorbs a number of photons in order to overcome the ionization threshold. This phenomenon was first explored in [17] where the number of the detected ions was observed to increase with a specific power of the laser intensity. The photoelectron spectrum was then measured by Agostini *et al.* [18] revealing even further photon absorption by the photoelectron in the ionization continuum (free-free transition) or what is called above threshold ionization. This phenomenon is well known and has been extensively studied by many researchers [19, 20, 21] (see also famous reviews [22, 23] for a detailed explanation).

The point related to this work is the second limiting case: $\gamma \ll 1$, when the time the electron takes to pass the bent Coulomb potential is shorter compared to the oscillation period of the electric field, the electron has a finite probability to tunnel into a free state. One possible outcome of the laser-atom interaction in this limiting case ($\gamma \ll 1$) is the generation of high harmonics of the driving laser field. The process of high harmonic generation occurs when the freed electron is driven back by the laser electric field to the ion core and releases its kinetic and potential energy as a high energy photon. High harmonic generation has become an important coherent source of XUV and x-ray light and has found a broad range of applications in physics, biochemistry and biology [24, 25]. This coherent source is currently the most useful tool in the investigation of ultrafast atomic and molecular dynamics on an attosecond time scale [3].

Experimental investigations done in this work utilize the $11^{\mathrm{th}} - 19^{\mathrm{th}}$ harmonics of infrared (IR) radiation (photon energy 1.55 eV) together with the infrared fundamental

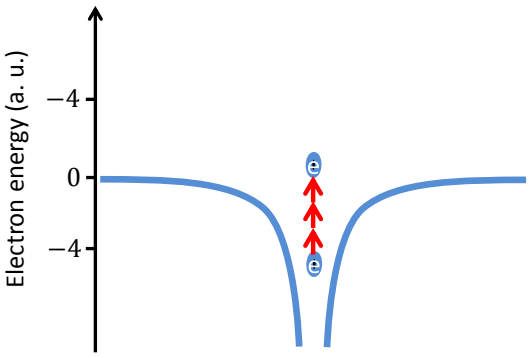

Figure 2.1: Schematic representation of the multiphoton ionization (MPI) of an atom in a strong laser field.

laser pulses, to track electron dynamics in xenon and krypton atoms in real time in pump-probe experiments. The intensities of the IR as well as of the XUV pulses are well inside the perturbative regime. This chapter gives a brief introduction to high harmonic generation and the time dependent perturbation theory necessary for an analysis of the experimental results.

Tunnel ionization

With the above mentioned light intensities, the corresponding electric field strength is comparable to the atomic field felt by an atomic valence electron. The Coulomb potential binding the electron gets distorted (see figure 2.2) and the electron has a finite probability to tunnel into the continuum. For $\gamma \ll 1$ the carrier frequency of the laser pulse is small compared to the instantaneous intensity-dependent tunneling frequency ($\omega_T = F_0/\sqrt{2I_p}$ [26], with F_0 the peak electric field strength in the laser pulse and I_p the ionization potential). Thus the potential seen by a valence electron while it tunnels can be approximated by a quasistatic effective potential which corresponds to the Coulomb potential suppressed by the instantaneous electric field in the laser pulse. The ionization rate (for $\gamma \ll 1$) for a valence electron in an atom under the influence of an alternating electric field has been derived by Perelomov *et al.* [27] by averaging the instantaneous tunnel ionization rate in a static field over one period of the applied oscillating laser electric field. Ammosov *et al.* [28] further derived the ionization rate for an electron in an arbitrary electronic state characterized by its angular momentum l and magnetic quantum number m as:

$$\omega_{ADK} = C^2_{n^*l^*} \left(\frac{3F_0}{\pi\mathcal{E}_0}\right) I_P \frac{(2l+1)\,(l+|m|)!}{2^{|m|}\,(|m|)!\,(l-|m|)!} \left(\frac{2\mathcal{E}_0}{F_0}\right)^{2n^*-|m|-1} \exp\left(-\frac{2\mathcal{E}_0}{3F_0}\right), \qquad (2.2)$$

where n^*, l and m are the effective principal, orbital angular momentum and magnetic quantum numbers of the initial electronic state, respectively. $\mathcal{E}_0 = (2I_P)^{3/2}$. The

coefficients $C^2_{n^*l^*}$ are expressed as

$$C^2_{n^*l^*} = \frac{2^{2n^*}}{n^*\Gamma\left(n^* + l^* + 1\right)\Gamma\left(n^* - l^*\right)}. \tag{2.3}$$

$l^* = n^* - 1$ is the effective angular momentum quantum number, n^* the effective principle quantum number of the initial state. The exponential dependence of 2.2 on the applied electric field amplitude indicates that the instantaneous ionization probability has the same exponential dependence on the time dependent electric field $E(t)$. This means that the tunneling ionization probability in an alternating electric field has sharp peaks at the electric field maxima. The freed electron is accelerated in the electric field and depending on the emission time in the electric field it may be driven back and revisit its parent ion. One of the recollision outputs is high harmonics generation of the fundamental laser frequency.

2.1 Three step model: high harmonic generation

The three step model describes the dynamics that accompany strong field ionization in the tunneling regime and gives a classical explanation of high harmonic generation through the classical trajectories the electron follows in the continuum in the presence of the strong electric field in three steps [5, 29], as shown in figure 2.2: first the electron is set free in the continuum with negligible initial velocity by tunneling ionization, second, its subsequent motion is governed only by the oscillating laser electric field. In this model the effect of the ion's Coulomb potential on the free electron is neglected compared to that of the strong external electric field (*Strong Field Approximation* SFA). The electron is then accelerated in the field and, depending on the phase of the laser electric field at the instance of ionization, it gains kinetic energy (ponderomotive energy) and when the electric field reverses its sign the electron may be driven back to its parent ionic core and recombine with it. These processes occur every half cycle of the periodically oscillating laser electric field. Revisiting the ion core may lead to several possible outcomes [30]: The ionized electron may elastically scatter off its parent ion core gaining high total kinetic energy (*High order Above Threshold Ionization* HATI [31]).

A second possible process is that the returning electron kicks out another bound one leading to ($Non - Sequential\ Double\ Ionization$ NSDI) of the parent ion [32]. If at the end of the laser pulse, the kinetic energy gained by the electron in the electric field is low, the electron may still be left bound in an excited Rydberg state. This indicates that some atoms may survive the interaction with the high intensity laser field (*Frustrated Tunneling Ionization* FTI [33, 34]). Another possible phenomenon related to this work occurs when the rescattered electron recombines with its ground state emitting a high harmonic photon whose energy equals the kinetic energy the electron gained in the oscillating electric field plus the ionization potential of the atom I_p (*High Harmonic Generation* HHG) [5, 29]. Assuming the electron starts after ionization at time t_0 with zero initial velocity $v(t_0) = 0$ at $X(t_0) = 0$ in the presence of a linearly polarized laser pulse with an electric field $E(t) = E_0\ \cos(\omega t)$ pointing along the $x-$axis,

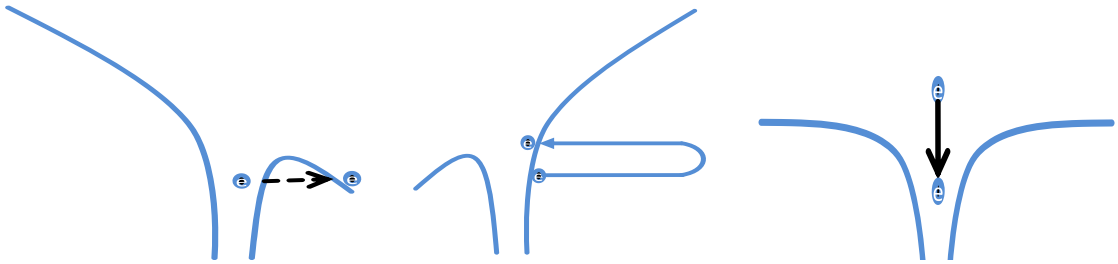

(a) (b) (c)

Figure 2.2: Three step model: taking into account a single active electron in the presence of the strong laser electric field. The electron is set free with zero velocity along the applied electric field **(a)**, and then accelerated in the laser electric field. Its kinetic energy depends on the time of the ionization with respect to oscillating external electric field **(b)**. When the electric field reverses its sign, the accelerated electron which corresponds to a certain emission phase ωt_0 (see text below), may be driven back and recombine with ion core with its total energy passed to a high harmonic photon which is emitted **(c)**.

the electron trajectory can be described classically by [5, 29]:

$$\begin{aligned} X(t) &= \frac{E_0}{\omega^2}\left[-\cos(\omega t) + \cos(\omega t_0) - \omega(t-t_0)\sin(\omega t_0)\right] \\ v_x(t) &= \frac{E_0}{\omega}\left[-\sin(\omega t) + \sin(\omega t_0)\right], \end{aligned} \tag{2.4}$$

where atomic units are used here. These equations clearly show that depending on the instant of ionization t_0 in the electric field, the freed electron may revisit its parent ion core i. e. $X(t_{recom}) = 0$.

Figure 2.3 shows trajectories of the electron released at different times within one optical cycle in the electric field of a laser pulse for initial conditions $X(t_0) = 0$, $v_0(t_0 = 0) = 0$. The ionized electron starts at the tunnel exit at $X(t_0) = 0$ and depending on the phase ωt_0 of the electric field at the instant of ionization t_0, it can turn back to the nucleus or escape and never return to the ion core. Three electron trajectories at three different phases ωt_0 are shown: for the black curve $\omega t_0 = -0.1$ the electron was released slightly prior to the electric field maximum at $\omega t = 0$. It never returns to its initial position $X(t_0) = 0$. The electron release times for trajectories represented by the red and blue curves are $\omega t_0 = 0.25, 0.06$, i. e. slightly after the electric field maximum. These trajectories intersect the time axis one and multiple times, respectively. Here it was assumed that the electron start times are restricted to one optical cycle $[0, 2\pi/\omega])$. However, these trajectories are repeated in every half laser cycle. The highest possible electron kinetic energy upon its first return to the ion core is $3.17U_p$. Recombination with the ion core at this kinetic energy leads to the generation of the highest energy photon at a harmonic order called "cutoff harmonic order". The cutoff harmonic order is determined by $q = (I_p + 3.17U_p)/\hbar\omega$ provided the electron recombines with the ion core by emitting a photon. This cutoff order can be extended by increasing the kinetic energy, namely U_p gained by the electron in the laser field. This can be accomplished through increasing

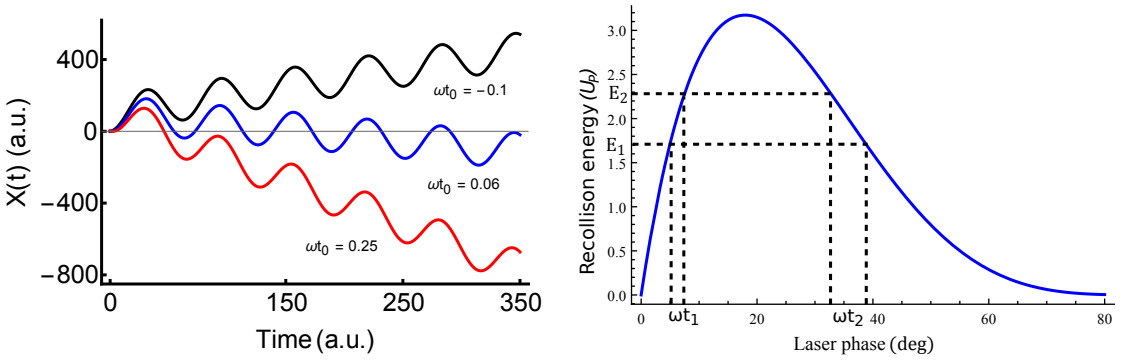

(a) (b)

Figure 2.3: **(a)** Classical trajectories of an electric field ionized electron born in a laser electric field $E(t) = E_0 \cos(\omega t)$ at three different phases ($\omega t_0 = -0.1, 0.06, 0.25$). The black curve shows an electron trajectory that never returns to its initial position $X(t) = 0$. On the red and blue trajectories the electron returns to its initial position $X(t) = 0$ one and multiple times, respectively. **(b)** the electron kinetic energy upon its first return to the ion core as a function of the phase ωt_0 at the moment of ionization. The maximum kinetic energy the electron can gain up to its first return in the electric field is $3.17U_p$. It is gained at an emission phase of $\omega t_0 = 17°$.

the intensity and wavelength of the fundamental driving laser beam [7, 35]. At a fixed wavelength of the driving laser radiation, it is also possible to extend this cutoff order by using atoms with a higher ionization potential.

Quantum formulation of the three step model

The three step model faces some limitations to explain some spectral and phase characteristics of the high harmonic spectrum. In order to better understand the details of the HHG features, Lewenstein and his co-workers have developed a quantum picture of the three step model by solving the time dependent Schrödinger equation in a strong field under the following assumptions [36]:

- After the electron is released into the continuum, it oscillates as a free particle in the externally applied oscillating electric field of the laser radiation (The atomic potential has no effects on its motion in the laser electric field).
- Ground state depletion is neglected.
- Contribution from all bound states, except from the ground state, can be neglected.

This model states that, using Feynman's path integral, the dipole moment at the q^{th} harmonic frequency can be written as a sum over all quantum paths leading to the same harmonic emission [37]

$$d_q = \Sigma_j \, a_j^q \, e^{\left[i\phi_j^q(r_j(t_0,t,P))\right]}, \tag{2.5}$$

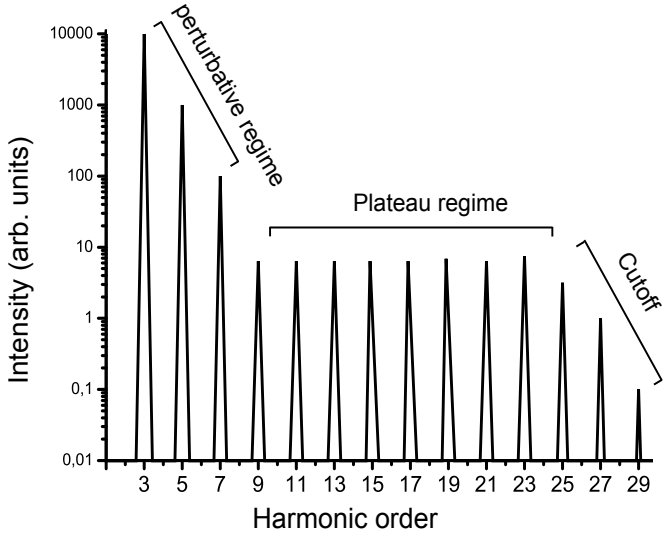

Figure 2.4: A high harmonic spectrum consists of three spectral regimes. A perturbative , plateau and cutoff regime [38].

a_j^q is the contributing amplitude of the j^{th} trajectory r_j to the emission of the q^{th} harmonic and P the electron drift momentum. ϕ_j^q is the dipole phase of the q^{th} harmonic field accumulated along the j^{th} trajectory of an electron ionized at t_0 and recombining to the ground state at t. This phase can be written as a classical action along the path $r_j(t_0, t, P)$ [37]:

$$\phi_j^q(r_j(t_0, t, P)) = q\omega t - \int_{t_0}^{t} \left(\frac{[P + A(t')]^2}{2} + I_p \right) dt', \tag{2.6}$$

$A(t') = -\int E(t)dt$ is the vector potential of the electric field $E(t)$ of the laser pulse. These phases are accumulated by the electron on its quantum path in the laser electric field. Only those paths have a stationary phase and correspond to momenta P, which start at the electron birth time t_0 and recombine at $X(t) = 0$ at time t, enter the integral. The expected cutoff energy in the harmonic spectrum is slightly higher than the one expected on the basis of the classical three step model. This model expects an intensity dependent phase of the harmonic dipole moment which allows the interpretation of more features of harmonic spectra.

2.2 Spectral and temporal characteristics of harmonic pulses

As mentioned above, the process leading to electron recombination and hence emission of high harmonic photons is repeated within every half optical cycle of the driving laser electric field. This results in bursts of short XUV pulses separated by half a laser period in the time domain and thus in the frequency domain structures separated by twice the driving laser frequency. Moreover, consecutive bursts result from recombination events where the electron approaches the ion core from opposite directions leading to spectral

components with the same spectral amplitudes but at opposite phases. This results in an interference that is destructive for even harmonics and constructive for odd ones. Therefore, we observe only odd harmonic orders in the spectrum. Figure 2.4 shows the typical high harmonic spectrum. It consists of three spectral regimes: the low harmonic orders (long wavelength), the plateau and cutoff regime. The intensity of the few first low harmonics in the first regime decreases with the harmonic order according to a power law which allows to describe this part of the harmonic spectrum using perturbation theory. The plateau harmonics are produced at higher driving laser intensities [1] and hence their intensities do not follow the power law any more due to the breakdown of the perturbation theory. The intensities of the plateau harmonics are relatively constant toward higher orders in this regime. In this regime two different electron trajectories contribute to the emission of individual harmonics: long and short trajectories interfere in the emission of the same harmonic order [39, 37]. This can be seen in figure 2.3**(b)**, at one given recollision kinetic energy E_1 there are two possible laser phases ωt_1 and ωt_2 at which the electron can start its trajectory and gain the same recollision energy. However, they have different ionization and recombination times and hence different excursion times in the electric field implying different harmonic emission times. This is classically expected in equation 2.4. The contribution of more than one trajectory to the emission of one harmonic means that every harmonic field generated by one of the two electron trajectories has a different dependence on the phase [39, 37]. The phase ϕ_j^q depends also on the light intensity, which is determined by the pulse envelope. On the short trajectories the intensity dependence of the phase $\partial\phi_j^q/\partial I$ is smaller than on the long ones.

For one harmonic order q the corresponding phase ϕ^q varies with the laser intensity over its pulse envelope leading to what is called harmonic chirp. Since the time scale of the harmonic chirp is the laser pulse envelope, this chirp can be compensated by imposing an opposite chirp to the laser pulse. Harmonic chirp leads to a temporal modulation of the harmonic phase which results in a broadening of the harmonic pulse width (non-transform-limited) [37, 40].

At a given laser intensity $\partial\phi_j^q/\partial q$ changes approximately linearly with harmonic order with positive sign for short trajectories and negative for the long ones [41]. This means that harmonics of different order q are produced at different return kinetic energies and thus from different electron trajectories within one laser cycle. This is shown in figure 2.3**(b)** where different recollision energies E_1 and E_2 corresponding to different harmonic orders are both generated at different laser phases ωt_1 and ωt_2 which are associated with different electron trajectories. This result is called chirp of the attosecond pulse (attochirp). Attosecond chirp leads to a non-transform-limited width and distorted temporal profile of the attosecond pulse.

So far we have discussed the effects of the single atom response on the phase of the harmonic field. However, the total harmonic field is built up in a dense gaseous generating medium and hence it is also affected by macroscopic propagation effects. Thus we will see in the next section that HHG can be optimized by minimizing the phase mismatch between the driving laser pulse and the generated harmonic field using various medium or laser parameters.

[1] Compared to lower order harmonics in the perturbative regime which are generated at low light intensities in the leading or trailing edges of the laser pulse.

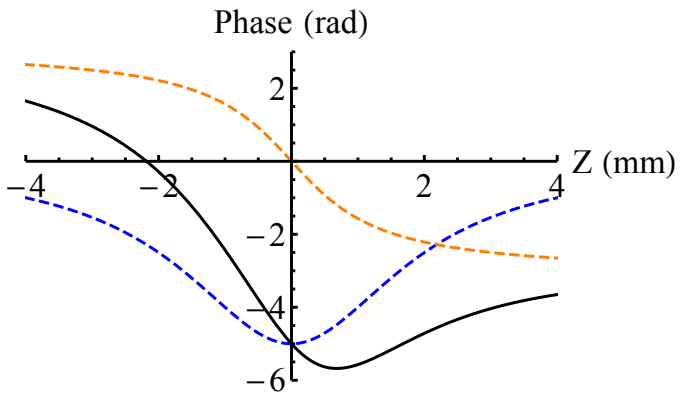

Figure 2.5: Two contributions to the phase mismatch as a function of the propagation distance z with respect to the focus position at $z = 0$. The orange-dashed curve represents the Gouy phase shift, the blue-dashed curve shows the dipole phase. The overall phase of the nonlinear polarization is represented by the sum of the two contributions (black curve). It shows a small phase mismatch around $z \approx 2.5\,\mathrm{mm}$ which means that an improved generation efficiency can be obtained by placing the focus by approximately this distance in front of the generating medium.

2.3 Phase matching

The single-atom response discussed above does not describe the whole harmonic generation processes in an atomic sample in the generating medium. It hence can not account for the total harmonic yield obtained in the experiment. It is the result of a coherent superposition of all individual harmonic fields generated by all atoms subjected to the driving laser pulse. Furthermore, in applications of high harmonics one needs an intense enough harmonic radiation to perform a certain experimental task. This can be achieved by generating the harmonics in a dense gaseous medium. Therefore, propagation effects of the harmonic and fundamental driving laser fields in the medium have to be taken into account. Efficient, coherent generation of harmonics necessitates the phase velocity difference between the driving and the generated fields to be minimized, i.e. they must be phase matched [42, 40, 43]. The length in the generating medium over which the harmonic field builds up constructively is called coherent length L_c. The phase mismatch $\Delta\phi_j^q$ between the driving laser field and q^{th} harmonic field generated is given by [37]:

$$\delta\Phi_j^q = k_q z - q\, k_1 z + q\, \arctan\left(\frac{2z}{b}\right) + \Phi_j^q\left(I\left(r,z,t\right)\right), \tag{2.7}$$

where k_q is the wave vector of the harmonic, k_l that of the driving laser, z the axial coordinate along in the propagation direction and b the confocal parameter of the laser focus. The electron trajectory, short or long, is identified by the index j. The first two terms describe the phase mismatch due to dispersion generated mainly by the free electrons produced in the medium during the ionization process.

This phase mismatch contribution can be minimized by applying appropriate gas pressure [44, 45]. Another main contribution to $\delta\Phi_j^q$ comes from the third term which represents the Gouy phase shift of the driving field along the propagation direction, induced by

focusing a Gaussian beam. This phase shift can be controlled by carefully choosing the focus position with respect to that of the generating medium. This allows an optimization of the phase-matching conditions for either the short or the long electron trajectory and thus to optimize the harmonic temporal and spectral features [40].

The fourth term in equation 2.7 represents a trajectory-dependent dipole phase mismatch. This phase is a function of the laser intensity distribution $I(z, r, t)$ in the focal spot, indicating that different quantum paths give rise to different phase matching conditions. If the short and the long trajectories contribute to the generation of the harmonics this results, as mentioned above, in distorted spectral and temporal harmonic profiles as well as in a poor harmonic intensity, since the phase mismatches are significantly different. On the other hand, this difference in phase matching conditions allows one to control the experimental parameters so as to optimize the phase matching for harmonic generation where only one of the trajectories contributes significantly while the contribution from the other one is nearly extinguished.

Different parameters can be manipulated in order to minimize the phase mismatch such as the laser intensity, generating medium geometry and gas pressure. For example, assuming that the gas density is low enough such that the linear dispersion terms in equation 2.7 can be ignored, taking into account only the Gouy phase shift and dipole phase contributions, the phase mismatch can be minimized by manipulating the focus position with respect to the nonlinear medium. Since the short trajectory has a phase varying slowly with the light intensity [37, 46], placing the laser focus slightly before the generating medium optimizes the phase matching for harmonics generated by the short trajectory at the expense of those generated by the long one. This leads to the generation of harmonics with regular spatial and spectral profiles. Figure 2.5 shows the variation of the phase of the driving polarization (dipole phase) at maximum pulse envelope as a function of the distance to the focal spot position along the propagation axis [40]. Positive values on the Z axis indicate a focus position in front of the nonlinear medium. The blue-dashed curve shows the atomic dipole phase (phase of the driving polarization) variation along the propagation direction. The atomic dipole phase varies significantly with laser intensity through the focus in the interval ($-2.5\,\mathrm{mm} < Z < 2.5\,\mathrm{mm}$). The orange-dashed curve shows the Gouy phase shift for the fundamental laser field across the focus. The sum of both phase mismatch contributions is represented by the black curve. For $Z > 0$ these two phases have opposite signs and they compensate each other (i. e. smaller slope), as shown by their sum (black curve). The variation of the total phase of the nonlinear polarization is small (i. e. smaller slope) around $Z \approx 2.5\,\mathrm{mm}$. This indicates that the phase mismatch can be minimized by placing the laser focus 2.5 mm in front of the nonlinear medium. For $Z < 0$ the two contributions have the same sign and add resulting in a fast variation (i. e. higher slope) of the total phase of the nonlinear polarization. Another advantage of selecting the short electron trajectories to generate the harmonic radiation is the possibility to avoid (minimize) the expected blue shift in the harmonic wavelength that is induced by the long trajectory owing to its increased sensitivity to the light intensity due to a longer excursion time in the electric field [47].

Finally, even in the case of phase match, generated harmonic radiation is reabsorbed in the generating nonlinear medium, leading to a limitation in the conversion efficiency [48]. In typical phase matched high harmonic generation experiments the harmonic radiation builds up over the length of the medium. At the same time it is reabsorbed by the medium

and therefore the harmonic yield is attenuated. Eventually the reabsorption overtakes the conversion efficiency thus limiting the usable length of the nonlinear medium for HHG. The attenuation is proportional to $(e^{-L\sigma_a(\lambda)n})$, where L is the medium length, $\sigma_a(\lambda)$ the wavelength dependent absorption cross section and n the gas density.

2.4 Second order time dependent perturbation theory

Experiments presented in this thesis are based on two-photon transitions in a pump-probe detection scheme. The electric field strength of the laser pulses, which are used in the pump and probe processes, are weak enough for their interaction with the matter to be described by perturbation theory. Explicitly, second order perturbation theory will be sufficient. This allows one to assume that the population in the atomic ground state does not change significantly and only a small fraction is transferred to excited states.

If at time $t = 0$ a perturbation (harmonic and infrared laser pulses for the work done here) is turned on the Hamiltonian of the system is given by:

$$H(t) = H_0 + H'(t), \tag{2.8}$$

with $H'(t)$ being the time dependent light pulse/atom interaction part of the Hamiltonian, which may be assumed to be different from zero in a time interval $[0, T]$. H_0 represents the non-perturbed atomic Hamiltonian. The evolution of the system for $t > 0$ can be obtained by solving the time dependent Schrödinger equation:

$$i\hbar\frac{\partial\Psi(t)}{\partial t} = H(t)\Psi(t). \tag{2.9}$$

In equation 2.9 $\Psi(t)$ is replaced by

$$\Psi(t) = e^{-iH_0t}\overline{\Psi}(t), \tag{2.10}$$

with $\overline{\Psi}(0) = \phi_i$ and ϕ_i being the system ground state. At the initial time $t = 0$ the system is thus in the ground state, i. e. $\Psi(t_0) = \phi_i$. The time derivative of equation 2.10 is given by:

$$i\dot{\Psi}(t) = H_0\Psi + e^{-iH_0t}\, i\dot{\overline{\Psi}}(t) = H_0\Psi(t) + V(t)e^{-iH_0t}\overline{\Psi}(t). \tag{2.11}$$

Subtracting the identical terms in this equation and multiplying both sides by e^{iH_0t} one obtains:

$$i\dot{\overline{\Psi}}(t) = e^{iH_0t}V(t)e^{-iH_0t}\overline{\Psi}(t). \tag{2.12}$$

Integrating both sides of equation 2.12 and applying lowest order perturbation theory by setting $\overline{\Psi}(t) = \phi_i$ on the right hand side we get:

$$\overline{\Psi}^{(1)}(t) = \phi_i - i\int_0^t dt' e^{iH_0t'}V(t')e^{-iH_0t'}\phi_i, \tag{2.13}$$

the lowest order perturbative result for $\Psi(t)$. Similarly, the nth perturbative result for $\overline{\Psi}(t)$ can be constructed successively by writing:

$$\overline{\Psi}^{(n)}(t) = \phi_i - i\int_0^t dt' e^{iH_0t'}V(t')e^{-iH_0t'}\overline{\Psi}^{(n-1)}(t'), \tag{2.14}$$

with $n = 1, 2, ...$ The first $\overline{\Psi}^{(1)}(t)$ and second $\overline{\Psi}^{(2)}(t)$ order perturbations are expressed, respectively, by:

$$\begin{aligned}
\overline{\Psi}^{(1)}(t) &= \phi_i - i\int_0^t dt' e^{iH_0t'}V(t')e^{-iE_it'}\phi_i & (2.15)\\
\overline{\Psi}^{(2)}(t) &= \phi_i - i\int_0^t dt' e^{iH_0t'}V(t')e^{-iH_0t'}\overline{\Psi}^{(1)}(t'). & (2.16)
\end{aligned}$$

Where $\exp(-iH_0t)\phi_i = \exp(-iE_it)\phi_i$ and $H_0\phi_i = E_i\phi_i$ with E_i the ground state energy. Substituting from equation 2.15 in equation 2.16 one gets for the time dependent second order perturbation:

$$\begin{aligned}
\overline{\Psi}^{(2)}(t) &= \phi_i - i\int_0^t dt' e^{iH_0t'}V(t')e^{-iH_0t'}\left[\phi_i - i\int_0^{t'} dt'' e^{iH_0t''}V(t'')e^{-iE_it''}\phi_i\right]\\
\overline{\Psi}^{(2)}(t) &= \phi_i - i\int_0^t dt' e^{iH_0t'}V(t')e^{-iE_it'}\phi_i\\
&\quad - \int_0^t dt'\int_0^{t'} dt'' e^{iH_0t'}V(t')e^{-iH_0t'}e^{iH_0t''}V(t'')e^{-iE_it''}\phi_i. \qquad (2.17)
\end{aligned}$$

At the end of the experimental pulse sequence at $t = T$ the probability to find the atomic system in a certain final state ϕ_f is determined, where ϕ_f is an eigenstate of the Hamiltonian H_0 of the unperturbed system. To second order this probability is given by the transition matrix element:

$$\begin{aligned}
M_{fi}^{(2)}(T) &= \langle\phi_f|\Psi^{(2)}(T)\rangle = \langle\phi_f|e^{-iH_0T}|\overline{\Psi}^{(2)}(T)\rangle\\
&= e^{-iE_fT}\langle\phi_f|\overline{\Psi}^{(2)}(T)\rangle\\
&= -ie^{-iE_fT}\int_0^T dt'\langle\phi_f|V(t')|\phi_i\rangle e^{i(E_f-E_i)t'}\\
&\quad -e^{-iE_fT}\int_0^T dt'\int_0^{t'} dt'' e^{i(E_ft'-E_it'')}\langle\phi_f|V(t')e^{-iH_0t'}e^{iH_0t''}V(t'')|\phi_i\rangle.
\end{aligned} \tag{2.18}$$

In the experiment $V(t) = \overrightarrow{d}\cdot\overrightarrow{F}(t)$ with d the dipole operator for the atomic system and F(t) the electric field strength of the applied laser pulses. Explicitly, $\overrightarrow{F} = \overrightarrow{F}_{XUV} + \overrightarrow{F}_{IR}$. Here $\overrightarrow{F}_{XUV}$ and $\overrightarrow{F}_{IR}$, for the experiments done in this work, represent the electric fields of an extreme ultraviolet (XUV) and an infrared (IR) laser pulse, respectively. Thus the transition matrix element $\langle\phi_f|V(t)|\phi_i\rangle$ vanishes. One can therefore express the relevant second-order transition matrix elements as:

$$\begin{aligned}
M_{fi}^{(2)}(T) &= -e^{-iE_fT}\sum_{k\neq i}\int_0^T dt'\int_0^{t'} dt'' e^{i(E_f-E_k)t'}e^{i(E_k-E_i)t''}\\
&\quad \times\langle\phi_f|V(t')|\phi_k\rangle\langle\phi_k|V(t'')|\phi_i\rangle
\end{aligned} \tag{2.19}$$

The sum runs over all possible intermediate states. The system is excited to an intermediate state which is then considered as an initial state for the second transition to the final state. In chapters 4 and 5 equation 2.19 is used to further derive the two-photon transition probabilities according to the specific experimental situation corresponding to the measurements presented in each chapter.

3 Experimental setup

Experiments done in this work have been performed using an existing experimental setup which will be briefly described in this chapter. An outline of the utilized experimental setup is shown in figure 3.1. It employs a Ti:Sapphire laser system from Spectra-Physics to generate high order harmonics in the extreme ultra-violet (XUV) spectral regime in noble gases. The generated XUV radiation is then used in combination with low intensity infrared (IR) laser pulses in pump-probe time-resolved experiments, where the XUV light pulses are used to initiate the desired electron dynamics in the atom under study and delay controlled IR pulses probe the system by inducing further continuum-continuum transition. Both pump and probe beam paths and the delay between them are implemented in a delay stage presented in detail in section 3.2. All measurements done in this work rely on detecting the time of flight (TOF) of photoelectrons of interest using a magnetic bottle electron spectrometer (MBES).

3.1 Laser system

The experiments presented in this thesis have been performed using a Ti:Sapphire chirped pulse amplification (CPA) laser system (Spactra-Physics, Spitfire Pro) delivering pulses with a temporal width of 42 ± 5 fs and 2.6 mJ pulse energy at 798 nm carrier wavelength and 1 kHz repetition rate. A Ti:Sapphire oscillator (Tsunami) pumped by a *Millennia Vs* solid state high power cw laser is used in the laser system. The oscillator delivers output pulses with an energy of 5 nJ and < 30 fs in duration. The output pulses from this oscillator are CPA amplified: the pulses are first stretched by two-pass passages over a diffraction grating to reduce their peak power in order to avoid any crystal damage during the amplification process. The pulses are amplified by multiple passes through a gain medium (Ti:Sapphire crystal) pumped by an EMPOWER frequency-doubled diode-pumped Nd:YLF laser system. The amplified pulses are compressed using a pair of diffraction gratings. The output beam has a diameter of ≈ 7 mm (at the laser exit) and is magnified by a telescope to ≈ 9 mm to avoid self focusing effects in the beam profile and to adapt the beam to the needs of the delay line used (see the next paragraph).

3.2 Beamsplitter and Delay Stage

The expanded Ti:Sapphire laser beam is directed into a Mach–Zehnder interferometer where it is split into two parts as shown in figure 3.2. The beam is split by a drilled mirror into a central part passing through the hole and a reflected annular part. The hole diameter is 8 mm. The central part of the beam carries most of the laser pulse energy (≈ 1.6 mJ) while the reflected annular beam part pulse energy is $\approx 400\,\mu$J. It is important to carefully choose the angel of incidence of the main beam onto the drilled mirror so as to get a rotationally-symmetric central as well as annular beam profile. The

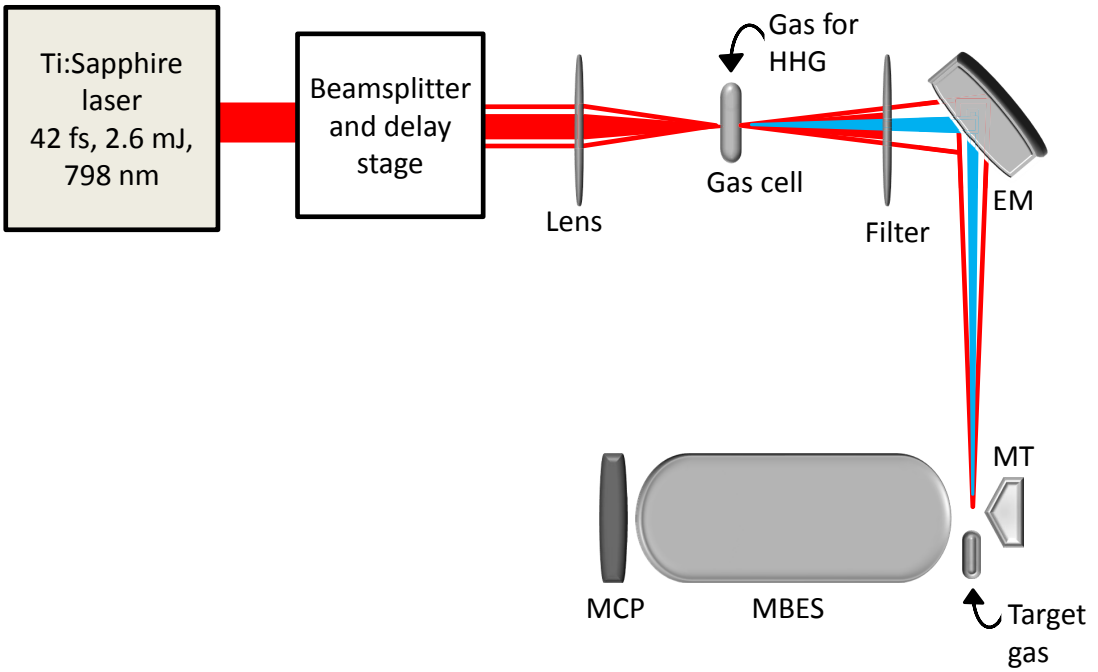

Figure 3.1: The setup used for the experiments presented in this thesis. The output beam of a Ti:Sapphire laser system is split into annular and central parts in order to introduce a variable delay-time between the pulses propagating in these two beam parts through a delay stage. The central part carrying most of the laser power is used for harmonic generation whereas the low power annular beam part is used as a probe beam. High harmonics (XUV) and the annular IR beams further propagate into an optical filter chamber with an aluminum-glass combined filter assembly. This filter is passed by the high harmonic XUV beam and the annular part of the IR beam (probe laser beam) while the IR central beam part used for HHG is blocked. An elliptical mirror focuses both XUV and IR beams at a position where they intersect a target atomic beam. Photoelectrons released from the interaction of the XUV and IR beam pulses with the atoms are directed via a magnetic tip (permanent magnet) into a magnetic bottle time of flight electron spectrometer (MBES) where they are detected by a multichannel plate detector (MCP).

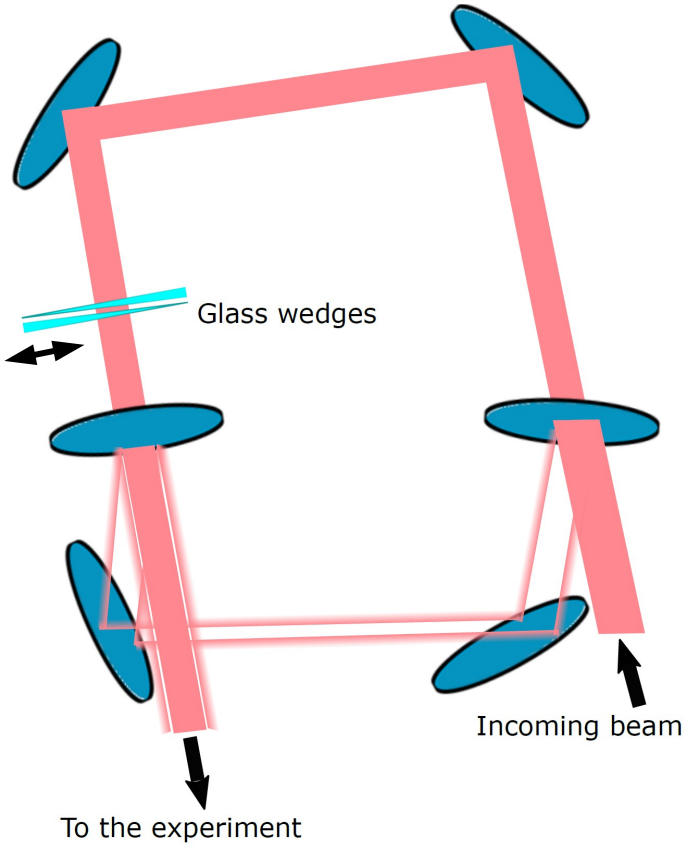

Figure 3.2: The delay stage and beamsplitter unit. The incoming beam is split at the first mirror into central and annular parts. The transmitted central part is time-delay controlled using a pair of glass wedges one of them is mounted on a translation stage which is driven with a computerized piezoelectric motor. The ring part is reflected from the same mirror and guided to recombine with the central part at a second drilled mirror which has the same hole diameter as the first one.

more powerful central part of the beam is used for high order harmonic generation and the low power annular beam part is used as a probe laser pulse. The interferometer arm where the annular part of the beam propagates consists of two plane mirrors mounted on a translation stage which can be adjusted with micrometer precision. This delay stage is used for the coarse adjustment of the time-delay between the two beam parts. For easy adjustment of the coarse time delay it is necessary to keep the angle of incidence of the beam on these mirrors as close as possible to 90°. This arrangement provides a stable beam pointing while moving the translation stage. The beam passing through the drilled mirror passes a pair of glass wedges for fine tuning of the time delay. The glass wedges are made of *Suprasil* with a wedge angle of 2.48°. The glass wedges are aligned to be perfectly parallel to each other to compensate residual dispersion. In order to keep a stable pointing of the laser beam passing the wedges a normal angle of incidence on to these wedges is chosen. In the measurements done in this work the time delay was introduced by fixing one of the wedges and moving the other one across the laser beam. The moving wedge was mounted on a translation stage that was driven by a piezo motor (Newport-*SMC100*). This enabled a position resolution for the wedge setting of 0.1 µm. Moving the whole length of the glass wedge through the beam path allows for a maximum delay range of ≈ 1100 fs. After passing the glass wedges the central beam part passes a second drilled mirror, with a hole diameter equal the one used for beam splitting. On this mirror the pump and probe beams are recombined. In the experiment presented in chapter 5 an additional half wave plate was placed in the path of the annular beam in order to flip the direction of the linear polarization of this beam from parallel to crossed with respect to the other beam. The whole delay stage setup was built on a separate breadboard which gives full flexibility to move the delay stage into any other optical setup if needed.

3.3 High Harmonic Generation Chamber

The generation of high harmonics is accomplished by focusing the central part of the laser beam into a vacuum chamber where the interaction of the strong electric field in the laser focus with a nonlinear medium takes place. This setup has already been described and used in several experiments in [49, 50, 51, 52]. The settings of the laser beam and medium parameters (focus position, pressure, generating medium,...etc.) play a significant role for HHG efficiency, see section 2.3 for a related discussion.

For HHG from noble gas atoms a high enough light intensity is needed in order to overcome their high binding energy. Therefore, the output beam from the delay stage is focused by a lens with 125 cm focal length mounted on a translation stage to adjust the focus position with respect to a windowless gas cell containing the nonlinear medium. A telescope was introduced in front of this lens to expand the beam's diameter by a factor of 1.5 in order to enhance the light intensity in the focal spot. The beam enters the HHG vacuum chamber through a glass window and is focused a few millimeter in front of the gas cell. The cell consists of an iron (Fe) tube with 4.5 mm inner diameter and 0.25 mm wall thickness. Apart from the beam responsible for HHG, also the annular probe laser beam passes through the gas cell. The openings of the cell are drilled into the walls of the initially closed tube by the focused laser beam within a few seconds. The annular

beam part has low power such that it does not contribute to the HHG processes except in the case when both the central and annular beam parts are overlapping in time in the gas cell. The exit hole in the iron tube burned by the central, high intensity part of the laser beam is wide enough to also pass the annular part of the beam. On the other hand, these holes through the iron tube walls have to be kept narrow enough to keep the background gas pressure in the surrounding HHG chamber as low as possible in order to minimize XUV beam absorption during its propagation. The input gas (nonlinear medium) is continuously supplied to the iron tube and pumped out of the surrounding HHG chamber using a turbo molecular pump *Pfeiffer* TMU with a pumping speed of 1500 l/s. An important parameter is the adjustment of the gas pressure in the HHG cell since it critically influences the conversion efficiency for those high harmonics of interest to the experiment.

Generated XUV pulses leave the HHG chamber through a small hole of 5 mm diameter connecting it to another vacuum chamber where an aluminum-glass combined filter is placed for further beam processing.

3.4 IR-XUV Filter Chamber

The hole connecting the IR-XUV filter chamber with the HHG chamber (see section 3.3) allows to differentially pump these two stages. In this way the background pressure in the filter chamber is kept at around 10^{-4} mbar while operating the HHG source. The center of this chamber was separated by 90 cm from the gas cell of the HHG source. The light filter consists of an aluminum foil of 400 nm thickness and 8 mm diameter combined with an annular glass plate (thickness = $200 \pm 50\,\mu$m) with a central hole of 7.5 mm diameter. This filter is aligned in such a way that the aluminum foil's diameter matches the diameter of the IR central part of the beam used for HHG. The foil blocks this part of the IR beam completely. The generated harmonics beam passes through the aluminum foil with a transmission depending on the harmonic order (harmonic wavelength). The transmission bandwidth of the aluminum foil, as shown in figure 3.4, extends from the 11^{th} harmonic ($\hbar\omega = 17$ eV) of the Ti:Sapphire laser radiation ($\hbar\omega$ =1.55 eV) with a transmission of ∼14% up to the 45^{th} harmonic ($\hbar\omega = 69.9$ eV) with a transmission of ∼34%. Transmission of the filter starts to rapidly increase with the harmonic order and reaches an approximately constant value of around 40% in the range between the 13^{th} and 29^{th} harmonics. Towards higher photon energy it increases linearly up to the high energy transmission limit. The thickness of the aluminum foil is chosen to completely suppress the 9^{th} harmonic. Otherwise it would add photoelectrons to the low kinetic energy range of the photoelectron spectra we take in the experiments and thus would interfere with those photoelectrons we are looking for. The harmonics used in the experiments in this work range from the 11^{th} harmonic (17 eV) up to the 19^{th} harmonic (29.5 eV). The glass filter delays the pulses in the IR annular beam by 400 fs compared to those in the XUV beam. This delay time interval is the time difference between the overlap in time of the XUV and IR annular beams in the HHG chamber and in the ionization chamber where the investigated interaction takes place. The glass filter, which does not transmit the XUV harmonic beam, also serves as an XUV beam phase cleaner. Choosing its hole's diameter sufficiently small, residual contributions to the high harmonics beam generated

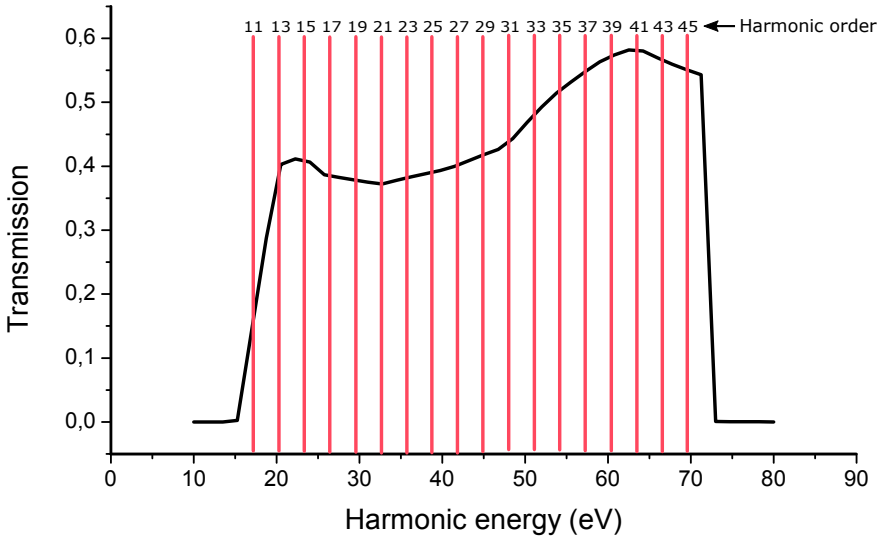

Figure 3.3: Transmission curve of the aluminum filter with 400 nm thickness.

from the long electron trajectory, which have a fast phase variation with the laser pulse intensity and are thus more divergent than those generated by the short trajectory, are absorbed in the glass part of the filter [53].

After both the XUV and annular IR beams passed through the filter they propagate to a third chamber through a second differential pumping hole which allows to pump this chamber down to a background pressure of $\approx 10^{-6}$ mbar. A computer controlled, gold coated, grazing incidence elliptical mirror is placed in this chamber. It is aligned so as to map the focal spot of the annular IR and of the XUV beams in the HHG chamber to a focus in the interaction chamber. This vacuum chamber is connected to the chamber containing the elliptical mirror through a third small opening for differential pumping. This allows to reach a background pressure of $\approx 10^{-8}$ mbar in the interaction chamber while the HHG source is in operation. Connected to the interaction chamber is a magnetic bottle electron spectrometer (MBES) used to detect the photoelectrons of interest which are created in the interaction of the laser beams with a target gas.

3.5 Data acquisition: Magnetic Bottle Spectrometer

A magnetic bottle spectrometer employs a magnetic field gradient and MCPs detectors in order to guide and detect the time of flight (TOF) of charged particles which here result from photoionization of a gas target. Such an instrument was first constructed and used in [54] and further developed by [55, 56]. In the experiments presented in chapter 4 and 5 a magnetic bottle electron spectrometer (MBES), that was designed and described in [38], is used to detect the TOF of photoelectrons of interest.

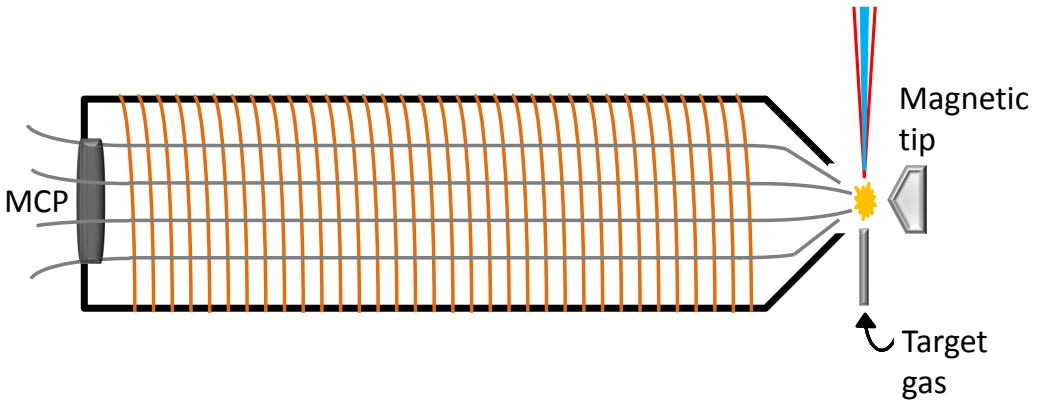

Figure 3.4: Magnetic bottle electron spectrometer. Two magnetic field regions: a strong inhomogeneous magnetic field is applied at the ionization point (beam focus) generated by a permanent magnet tip and a weak magnetic field in the bottle which is generated by a current flow in a coil represented by the orange vertical lines. The photoelectrons generated in the laser focal spot are forced by the strong magnetic field to undergo a helical motion along the magnetic field lines into the homogeneous weak field region where their direction of motion is almost parallel to the magnetic field lines. The photoelectrons are detected by an MCP detector located at the end of the flight tube.

Principle of Operation

The MBES consists of two regions of a significant magnetic field difference in which the electron motion follows helical trajectories according to the magnetic force (Lorentz force). An inhomogeneous strong magnetic field B_i ($\sim 782\,\mathrm{mT}$) is applied in the interaction volume of the laser beams with the target gas by means of a permanent magnet with a soft iron tip as shown in figure 3.4. This magnetic field is rapidly decreasing when moving few millimeters away from the soft iron tip. This field region is connected through a small hole of 2.5 mm diameter with a flight tube (bottle) with a weak ($\sim 0.00012\,\mathrm{T}$) and approximately homogeneous magnetic field B_f, as schematically shown in figure 3.4. Provided the magnetic field changes adiabatically along the electron trajectory (i. e. the change in the magnetic field acting on an electron during consecutive turns of its helical motion is negligible compared to the average field over the turns), the electron's angular momentum and the energy are conserved quantities. This means that an electron moving in the interaction point with a velocity v at an angle θ_i with respect to the spectrometer axis will experience a decrease in the velocity component transverse to the local magnetic field and an increase in the longitudinal one in the flight tube where the magnetic field is small [54], i. e.

$$\sin(\theta_f) = \left(\frac{B_f}{B_i}\right)^{1/2} \sin(\theta_i). \tag{3.1}$$

This relation indicates that the electrons move on almost parallel trajectories within the homogeneous weak magnetic field region irrespective of their initial direction of motion in the strong field region. The relation implies that increasing the difference between B_i and B_f results in improved parallelism. The maximum angular deviation from the parallelism of the electron trajectories in the homogeneous magnetic field given by equation 3.1 at the above given B_i and B_f values and an initial angle of $\theta_i = 90^\circ$ is $\theta_f = 0.7^\circ$

Settings of the electron spectrometer

In the MBES used in this work, a cylindrical Samarium-Cobalt (Sm_2Co_{17}) permanent magnet with a diameter of 15 mm and height of 10 mm provides the strong inhomogeneous magnetic field of 782 mT. In order to obtain a fast reduction of this high field, a conical soft iron pole is placed on top of the cylindrical cross section of the permanent magnet. The resultant magnetic field drops to 214 mT within only 1 mm above the apex of this tip. The weak homogeneous magnetic field is generated by a simple coil made of copper wire with a rectangular cross section of $4 \times 1.5\,\mathrm{mm}^2$. The copper wire is wound around the flight tube of 1.5 m length with 373 turns of 274 mm diameter. This coil is placed at a distance of 11 cm to the ionization point (focal spot of the laser beam) within the vacuum chamber. The flight tube together with the coil are covered by a cylindrical layer made of *Mumetall* with 2 mm thickness to avoid an effect of the earth magnetic field on the electron trajectories.

The gas under study is fed into the ionization chamber as an effusive atomic beam through a thin capillary (with inner diameter of 125 µm) which is position controlled via a three-axis flexure mount. This capillary is aligned in such a way that the incoming

atomic beam crosses the laser beam at its focus in between the tip of the magnet and the hole separating the flight tube from the interaction chamber. The ionization chamber is pumped by a Turbo pump with 500 l/s pumping speed. The pressure during an experimental run in this chamber is kept around 10^{-6} mbar while in the flight tube, which is pumped by a separated Turbo molecular pump ($Varian$, $Trubo-V301$) with a pumping speed of 250 l/s, is around 10^{-7} mbar, measured with ultra-high vacuum gauges. These gauges are turned off during data acquisition to avoid effects on the experimental results induced by ions and electrons produced by them.

Two microchannel plates (MCP) chevron stacked with their inclined microchannels are used for electron detection [57]. Depending on the high voltage applied across the MCP stack, this configuration can produce up to $\sim 10^8$ secondary electrons in a short pulse per electron hitting the first MCP. The MCP stack is placed at the end of the flight tube. Signal current pulses are picked off at the rear side of the MCP stack and fed into an *Acqiris AP240* digitizer card with 2 Gs/s real time sampling rate. This digitizer card samples a time interval between $[0.0005\,\mu s - 10\,\mu s]$ after each laser pulse. The digitizer card is connected to a computer via a PCI interface. It is controlled by a Labview program to average over 20000 waveforms and send the average TOF data to the computer. The TOF spectrum is transformed into a photoelectron kinetic energy distribution using equation 3.2 below in a separate computer code.

Photoelectron kinetic energy resolution of the spectrometer

In the experiments done in this thesis, the time of flight T of the electrons from the focal spot to the detector is measured. This information and the known separation L of the focal spot (electron source) from the detector are used to determine the velocity v and kinetic energy the photoelectron had after ionization in the focal spot. In the MBES the relation between the TOF and v is approximately given by [54]:

$$T = \frac{L}{v}\left(1 + \frac{B_f \sin^2\theta_i}{2B_i}\right). \tag{3.2}$$

In this equation the TOF depends on the initial emission angle θ_i in the high-field region. This limits the accuracy of the relation between the TOF T and v and thus contributes significantly to the possible velocity (kinetic energy) resolution. Equation 3.2 holds only when the adiabaticity criterion is satisfied (see above in the principle of operation section). Another condition for the validity of equation 3.2 is that a length of the electron trajectory in the region with inhomogeneous magnetic field is short compared to the path length in the homogeneous weak-field region. Assuming these conditions to be fulfilled, only the longitudinal electron velocity (i.e. the electron velocity is parallel to the axis of the flight tube) has to be taken into account and thus equation 3.2 may be rewritten as:

$$T = \frac{L}{v_\parallel}, \tag{3.3}$$

where $v_\parallel$ is the electron velocity component that is parallel to the spectrometer axis (flight tube). The photoelectron kinetic energy can be obtained from the TOF through:

$$E_e = \frac{m_e}{2e}\left(\frac{L}{T - T_t}\right)^2. \tag{3.4}$$

Here T is the flight time and T_t an additional time delay due to the limited signal speed in the electronics. This time was determined to be 10 ns in the measurements presented in chapter 4 and 5. The TOF resolution is determined from relation 3.2 to be:

$$\frac{\Delta T}{T} = \frac{\Delta E_e}{2E_e} = \frac{B_f}{2B_i}, \tag{3.5}$$

this relation represents the lower limit for the TOF and energy resolution. With the above mentioned values of parameters a coil current of 0.4 A creates a homogeneous magnetic field of around 0.1 mT. This results in a lower limit of the relative resolution of the TOF of around 10^{-3}. However, the actual relative resolution in the measurements presented in this work is estimated from the spectral width of the individual harmonics to be around 10^{-2}. The largest contribution to a degradation of the TOF resolution comes from the strong magnetic field region where the electron trajectories are still not parallel to the axis of the flight tube [54]. Therefore, the decrease in B_i at the interaction point must be fast such that it reaches a negligible value over as short as possible a distance. On the other side, this reduction of B_i should not be too fast to keep a satisfied adiabaticity criterion. Other contributions which limit the kinetic energy resolution are the time bin size of the ADC used and the overall width of the response of the electronics including the MCP to a "delta-electron-pulse", which may even depend on the total charge in this pulse through the MCP due to saturation effects. Further contributions may come from stray electric fields which may be different for the individual trajectories of the electrons which pass different regions of space between the focal spot and the detector. The origin of these electric fields are contact potentials of surfaces made of different materials in the spectrometer . This effect can be minimized by coating the inner metal surfaces of the ionization chamber and the poles surfaces of the permanent magnet for example with colloidal graphite.

4 Real-Time Tracking of Two Electron Dynamics in the Ionization Continuum of Xe

This chapter presents experimental results of real-time tracking of coherent two-electron dynamics in broadband electronic wavepackets in the ionization continuum of the Xe atom. Ultra-short extreme ultraviolet (XUV) harmonic pulses are used to excite continuum wavepackets in an energy range structured by Fano resonances. The spectral width of the XUV pulses covers several of these resonances (see figure 4.1). The resonances involved in the excitation processes are of the type of two-valence-electron and single-inner-valence-electron excited-state (see figure 4.3 in section 4.2). The 15th harmonic covers resonances of type $5s5p^6nl$ with principle quantum number n ranging from $n \approx 14$ up to $n \approx 21$ and one resonance of type $5s^25p^4nln'l'$ with fixed n, n' and orbital angular momenta l, l'. At the same time, the 17th harmonic launches a continuum wavepacket well above the Xe $5s5p^6$ ionization threshold where only resonances with two-valence electrons are excited. The evolution in time of the excited wavepackets is probed by inducing a continuum-continuum transition with the IR laser pulses at variable delay times with respect to the XUV pulses. The photoelectrons are detected in the continuum after this two-photon transition. The presence of different electron configurations in each of the excited wavepackets leads to two-electron dynamics in the ionization continuum after the bound-free transition induced by the XUV harmonic pulses. The dependence of the photoelectron yields corresponding to the continuum wavepacket dynamics on the delay time between the XUV-pump and IR-probe pulses is analyzed on the basis of Fano's theory. (Parts of this chapter have been published in [58].)

4.1 Background

Electron-electron correlation/interaction in many electron atoms influences the energy level structure and the corresponding wave functions (eigenstates of the atomic Hamiltonian). This correlation and interaction can be accessed either through high resolution spectroscopy or by real-time tracking of the electronic dynamics in broadband electronic wavepackets that are coherently excited by ultrashort laser pulses in an atomic system [2, 1]. The electronic wavepackets which are launched by exterme ultraviolet (XUV) high harmonic pulses usually involve two-electron, single inner-valence-electron, or inner-shell-electron excited states. These highly excited states are usually embedded in the ionization continuum of the atom forming what is called Fano resonances [59]. Therefore, the time evolution of these wavepackets involves two-electron dynamics.

Tracking the time evolution of electron dynamic in many electron atoms in real time started by Drescher *et al.* [3] in an experiment that tracks an Auger decay in xenon atoms after photoexcitation in real time. Time domain tracking of electron dynamics in the spectral range where Fano resonances are present is basically accomplished by exciting an electronic wavepacket by an ultra-short XUV light pulse and tracking its time

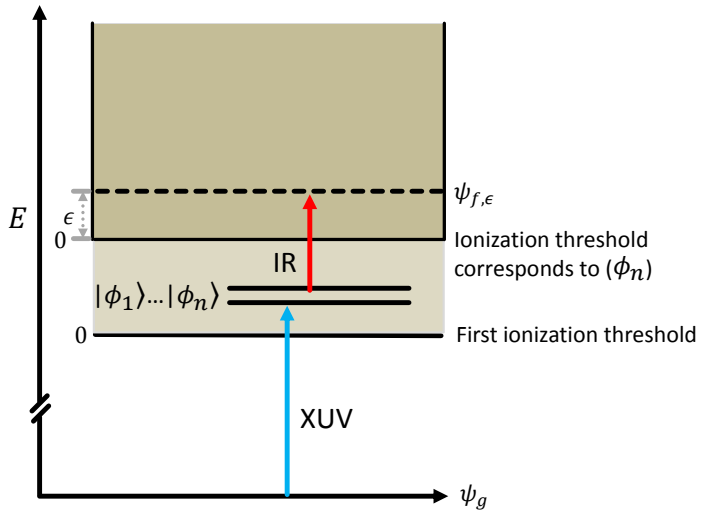

Figure 4.1: The principle excitation scheme addressed in the experiment presented in this chapter.

evolution by inducing a further continuum-continuum transition via a second delayed infrared laser pulse. The evolution in time of the wavepacket may then be obtained either by analyzing changes that occur in the absorption spectrum of the XUV pulse due to the probe pulse [60, 61, 62] or by detecting photoelectrons which have consecutively absorbed a pump and a probe photon [63, 64, 9]. In this chapter the latter technique is employed to experimentally implement real-time tracking of the time evolution of wavepackets in the ionization continuum of xenon where the spectral range covered by an XUV pump-pulse excites wavepackets spanning more than two Fano resonances (see figure 4.1). The evolution of the continuum wavepacket in time is tracked by inducing a continuum-continuum transition with an IR laser pulse at controllable delay time. In the time evolution of such a wavepacket, besides the autoionization decay, one expects to observe superimposed coherences due to two-electron dynamics brought about by the Fano resonance structure of the continuum within the bandwidth of the exciting laser pulse [65, 66, 9]. The dependence of the experimental data on the pump-probe delay time can be approximated by a two-photon transition probability derived on the basis of Fano's theory.

4.1.1 Fano Resonance Structure: more than one discrete state embedded in one continuum

The ultrashort XUV pulses, which are used for photoexcitation in the experiment presented here, cover a broad bandwidth in the energy spectrum of the atom. Such pulses coherently excite broadband electronic wavepackets in the atomic system well above the first ionization threshold. Fano resonances which appear in this continuous part of an atomic absorption spectrum can be characterized in terms of configurations interaction [59]. This section reviews that part of the theoretical work of reference [59], which deals

with the case of more than one discrete electron configuration ϕ_n being embedded in one continuum ψ_ϵ. The Hamiltonian matrix elements describing such a system are given by [59]:

$$\begin{aligned} \langle\phi_m|H|\phi_n\rangle &= E_n\delta_{mn} && (4.1)\\ \langle\psi_\epsilon|H|\phi_n\rangle &= V_{\epsilon n} && (4.2)\\ \langle\psi_{\epsilon'}|H|\psi_\epsilon\rangle &= \epsilon\delta(\epsilon'-\epsilon). && (4.3) \end{aligned}$$

E_n are the discrete system eigenvalues in a subspace of the Hilbert space spanned by the configurations ϕ_n $(n = 1, ...N)$. The $V_{\epsilon n}$ represent the interaction strength between the discrete ϕ_n and the adjoining continuum configurations ψ_ϵ. The eigenstates of the full atomic Hamiltonian H can be written as a linear combination of the discrete ϕ_n and continuum ψ_ϵ configurations:

$$\Psi_E = \sum_n a_n\phi_n + \int d\epsilon' b_{E,\epsilon'}\psi_{\epsilon'}. \tag{4.4}$$

a_n and $b_{E,\epsilon'}$ are energy dependent coefficients. Two types of configuration interactions are involved: one is a second-order interaction between the discrete configurations due to their coupling through the same continuum $\psi_{\epsilon'}$. This interaction perturbs the energy positions E_n of the discrete configurations ϕ_n and modifies them into (see [59])

$$\overline{\phi}_p = \sum_n A_{np}\phi_n, \tag{4.5}$$

where $\overline{\phi}_p$ $(p = 1, ...N)$ are the modified bound configurations corresponding to shifted energy positions F_p. A_{np} are the corresponding coefficients. The coefficients a_n are then given by [59]:

$$a_n = \sum_p A_{np}\overline{a}_p, \tag{4.6}$$

where $\overline{a}_p$ are the new energy dependent coefficients. The energy dependent coefficients $\overline{a}_p$ and $b_{E,\epsilon}$ are given by [59]:

$$\begin{aligned} \overline{a}_p &= \cos\Delta\tan\Delta_p/\pi V_{Ep} && (4.7)\\ b(E,\epsilon') &= \cos\Delta\left(\sum_p \frac{V_{\epsilon' p}\tan\Delta_p}{\pi V_{Ep}(E-\epsilon')} - \delta(E-\epsilon')\right), && (4.8) \end{aligned}$$

with

$$\Delta = -\arctan(\sum_p \frac{\pi|V_{Ep}|^2}{E-F_p}),\ \Delta_p = -\arctan(\frac{\pi|V_{Ep}|^2}{E-F_p}) \tag{4.9}$$

representing phase shifts due to the interaction between discrete and continuum configurations. These phase shifts vary quite sharply when E sweeps an energy range of width $|V_{Ep}|^2$ containing one of the resonances at energies F_p. The sharp variation of Δ and Δ_p at the resonance energies (i.e. at $E = F_p$) causes a rapid variation in the transition matrix element from the ground state ψ_g to the continuum Ψ_ϵ, due to the interference

of the contributions from the matrix elements $\langle\psi_\epsilon|\overrightarrow{d}|\phi_g\rangle$ and $\langle\Phi'_p|\overrightarrow{d}|\psi_g\rangle$, with Φ'_p being defined by equation 4.11. This causes the vanishing of $\langle\Psi_\epsilon|\overrightarrow{d}|\psi_g\rangle$ in any interval between every two successive resonances. These resonances can actually be described by curves that are functions of the following two parameters [59]:

$$\begin{aligned} \varepsilon &= \frac{E - F_p}{\Gamma_p/2} \\ q_p &= \frac{\langle\Phi'_p|d|\psi_g\rangle}{\pi V_{p\epsilon}\langle\psi_\epsilon|\overrightarrow{d}|\psi_g\rangle}, \end{aligned} \tag{4.10}$$

where

$$\Phi'_p = \overline{\phi}_p + PV\int d\epsilon' \frac{\psi_{\epsilon'} V_{\epsilon' p}}{E - \epsilon'}. \tag{4.11}$$

Here $V_{\epsilon' p} = \sum_n V_{\epsilon n} A_{np}$. PV indicates the principle value of the integral to avoid the singularity at the zero of the denominator. F_p in equation 4.10 is the shifted energy, $\Gamma_p = 2\pi|V_{Ep}|^2$. The transition matrix element from the ground state ψ_g to the continuum state Ψ_E is given by [59]:

$$\langle\Psi_E|d|\psi_g\rangle = \langle\psi_E|d|\psi_g\rangle\cos\Delta\left[\sum_p q_p\tan\Delta_p - 1\right]. \tag{4.12}$$

The transition matrix element $\langle\psi_E|d|\psi_g\rangle$ is a slowly varying function of the energy E. In the experiment presented in this chapter this transition is induced by the XUV light pump-pulse. In the next section equation 4.12 will be used to further derive a two-photon transition matrix element corresponding to the pump-probe experiment that is of interest here.

In case of only one discrete configuration being involved the ratio $R(\varepsilon, q)$ between the transition probabilities to the exact continuum Ψ_ϵ state and to the approximate continuum configuration ψ_ϵ can be expressed by:

$$R(\varepsilon, q) = \frac{|\langle\Psi_\epsilon|\overrightarrow{d}|\psi_g\rangle|^2}{|\langle\psi_\epsilon|\overrightarrow{d}|\psi_g\rangle|^2} = \frac{(q_p + \varepsilon)^2}{1 + \varepsilon^2}. \tag{4.13}$$

Figure 4.2 shows this ratio as a function of ε for different values of q_p. In this ratio the denominator $|\langle\psi_\epsilon|\overrightarrow{d}|\psi_g\rangle|^2$ is a slowly varying function of the energy ϵ.

4.1.2 Time evolution of the coherent dynamics of a continuum electronic wavepacket encompassing several Fano resonances

The electron dynamics presented in this chapter are launched with an XUV high harmonic pulse of Ti:sapphire laser pulse. They are then probed with a low intensity IR laser pulse where the delay between the two pulses can be arbitrarily chosen. The applied intensities of both light pulses are weak enough allowing the pump and probe processes to be described, as explained in section 2.4, with second-order time-dependent perturbation theory. This implies that the measured yield of the photoelectrons that consecutively

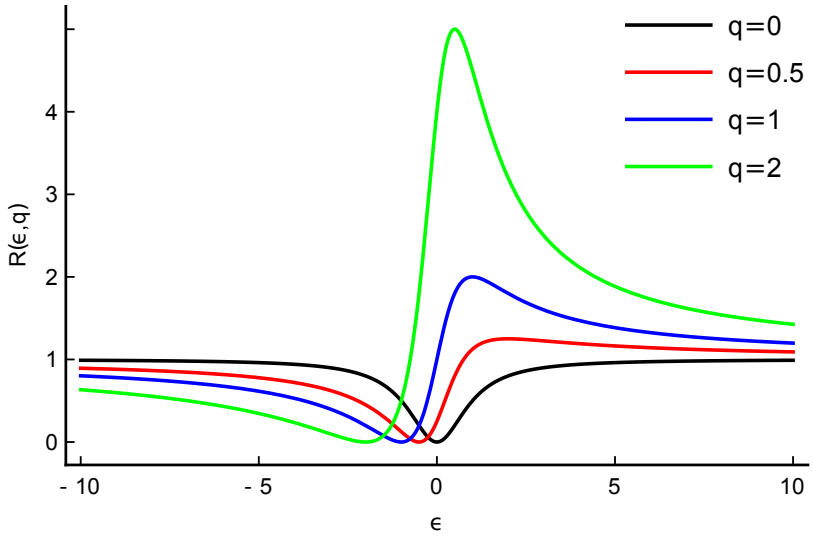

Figure 4.2: The ratio $R(\varepsilon, q)$ as a function of ε plotted for different values of q-parameter.

have absorbed two photons one from the pump and one from the probe pulse can be described by a two-photon transition matrix element $M_{f,g}(\epsilon)$. It represents a transition from the atomic ground state ψ_g to a final continuum states $\Psi_{f,\epsilon}$. f represents all discrete quantum numbers characterizing the final continuum state reached after the two photon transition and ϵ the kinetic energy of the photoelectron in the continuum. It is assumed that these final continuum states $\Psi_{f,\epsilon}$ can only be reached via intermediate continuum states $\Psi_{j,E}$ reached upon the absorption of the XUV-pump pulse. These intermediate continuum states $\Psi_{j,E}$ are eigenstates of the atomic Hamiltonian and according to Fano's theory [59], they can be represented by a linear superposition of the discrete ϕ_k^j and continuum configurations $\psi_{\epsilon'}^j$:

$$\Psi_{j,E} = \sum_{k=1}^{n} a_k^j(E)\,\phi_k^j + \int d\epsilon'\; b^j(E,\epsilon')\,\psi_{\epsilon'}^j, \tag{4.14}$$

here k numbers the discrete configurations involved in the launched wavepacket and j are the discrete quantum numbers that characterize the continuum intermediate eigenstates of the atomic Hamiltonian. $a_k^j(E)$ and $b^j(E,\epsilon')$ are energy dependent coefficients characterizing the atomic eigenstates $\Psi_{j,E}$ in terms of the discrete ϕ_k^j and continuum configurations $\psi_{\epsilon'}^j$. These configurations are assumed to be eigenstates of a particular part of the full atomic Hamiltonian [59]. $a_k^j(E)$ and $b^j(E,\epsilon')$ are given by equations 4.8. These coefficients are fixed using Fano's theory to incorporate the missing part of the full Hamiltonian which is responsible for a residual interaction among the states ϕ_k^j and $\psi_{\epsilon'}^j$ (see section 4.1.1) [59].

The matrix elements for a two-photon transition from the atomic ground state ψ_g to a

final continuum state $\Psi_{f,\epsilon}$ can be expressed as (see section 2.4):

$$T_{f,g}(\epsilon) \propto \sum_j \int dE \int_{-\infty}^{\infty} dt \int_{-\infty}^{t} dt' \, \langle \Psi_{f,\epsilon}|V(t)|\Psi_{j,E}\rangle \langle \Psi_{j,E}|V(t')|\Psi_g\rangle \, e^{i(\epsilon-E)t} \, e^{i(E-\epsilon_g)t'}, \tag{4.15}$$

where an overall phase factor of type e^{ix} with x a real number, which does not influence the transition probability, has been ignored. Assuming that only continuum intermediate states $\Psi_{j,E}$ contribute significantly to $T_{f,g}(\epsilon)$, one can restrict oneself to integrate only over energies E in the ionization continuum as is done in equation 4.15. The sum over j takes into account that several degenerate continua may be important. $V(t)$ represents the time dependent interaction of the atom with the externally applied light pulses. It is given by:

$$V(t) = (\mathbf{d}\hat{\mathbf{e}}_{\mathrm{x}})E_{\mathrm{x}}(t) + (\mathbf{d}\hat{\mathbf{e}}_{\mathrm{ir}})E_{\mathrm{ir}}(t), \tag{4.16}$$

with $\mathbf{d}$ representing the dipole operator of the atomic system and E_{x}, E_{ir} the electric fields of the XUV and IR laser pulses, respectively. $\hat{\mathbf{e}}_{\mathrm{x}}$ and $\hat{\mathbf{e}}_{\mathrm{ir}}$ are unit vectors representing the directions of linear polarization of these pulses. The electric fields E_{x}, E_{ir} of the light pulses can be presented in the form:

$$\begin{aligned} E_{\mathrm{x}}(t) &= A_{\mathrm{x}}(t)\cos(\omega_{\mathrm{x}}t), \\ E_{\mathrm{ir}}(t) &= A_{\mathrm{ir}}(t-\delta)\cos[\omega_{\mathrm{ir}}(t-\delta)]. \end{aligned} \tag{4.17}$$

$A_{\mathrm{x}}(t) = A_0 e^{-\alpha t^2}$ and $A_{\mathrm{ir}}(t) = B_0 e^{-\beta(t-\delta)^2}$ are assumed to be slowly varying Gaussian amplitude functions of the electric field strengths of the pulses. Their durations and spectral widths are fixed by the α and β parameters, A_0 and B_0 represent amplitude factors. ω_{x} and ω_{ir} are the carrier frequencies of the XUV and IR pulses, respectively. δ indicates explicitly the temporal delay of the IR laser pulse with respect to the XUV one.

Substituting from equations 4.16 and 4.17 into equation 4.15 and applying the rotating wave approximation for the transition from the atomic ground state to the intermediate continuum states and for the subsequent continuum-continuum absorption of the IR photon the transition matrix element may be rewritten as:

$$M^{\delta}_{f,g}(\epsilon) \propto \frac{1}{4}\sum_j \int dE \; \underbrace{\langle \Psi_{f,\epsilon}|\mathbf{d}\hat{\mathbf{e}}_{\mathrm{ir}}|\Psi_{j,E}\rangle\langle\Psi_{j,E}|\mathbf{d}\hat{\mathbf{e}}_{\mathrm{x}}|\psi_g\rangle}_{P_{\mathrm{a}}^{f,j}(\epsilon,E)} \underbrace{e^{-iE\delta}\int_{-\infty}^{\infty} dt \int_{-\infty}^{t} dt' e^{i(\epsilon-E-\omega_{\mathrm{ir}})t} \, e^{i(E-\epsilon_g-\omega_{\mathrm{x}})t'} A_{\mathrm{ir}}(t)A_{\mathrm{x}}(t')}_{P_{\mathrm{I}}(\epsilon,E,\delta)}. \tag{4.18}$$

In this equation $M^{\delta}_{f,g}(\epsilon)$ includes two factors under the integral over the intermediate state energies E: one depends only on the characteristics of the laser pulses [$P_{\mathrm{I}}(\epsilon,E,\delta)$ in equation 4.18] and the second factor depends only on the characteristics of the atom and consists of the product of atomic dipole matrix elements [$P_{\mathrm{a}}^{f,j}(\epsilon,E)$ in equation 4.18]. The

phase factor $\exp(-iE\delta)$ in the equation, which depends on the intermediate continuum state energy E, represents the effect of the delay of the IR pulse with respect to the XUV one. $P_{\mathrm{a}}^{f,j}(\epsilon, E)$, the product of atomic dipole matrix elements, can be further evaluated using Fano's theory [59]. We assume that the relevant Fano resonances lying within the spectral bandwidth of the XUV laser pulse can be represented by continuum wave functions as given in equation 4.14 with n discrete electron configurations involved which are assumed to have a residual interaction with one continuum configuration and possibly among each other. The part of the transition matrix element $P_{\mathrm{a}}^{f,j}(\epsilon, E)$ that corresponds to the transition from the atomic ground state to the intermediate continuum states is given by Fano [59] (equation 4.12) as:

$$\langle \Psi_{j,E} | \mathbf{d}\hat{\mathbf{e}}_{\mathrm{x}} | \psi_g \rangle = \langle \psi_E^j | \mathbf{d}\hat{\mathbf{e}}_{\mathrm{x}} | \psi_g \rangle \cos\Delta \left[\sum_{k=1}^{n} q_k^j \tan\Delta_k - 1 \right]. \tag{4.19}$$

It is also assumed here that the final continuum ϵ, which is reached after the subsequent absorption of one IR photon, is free of Fano resonances in the relevant spectral range and the continuum-continuum dipole matrix element in $P_{\mathrm{a}}(\epsilon, E)$ can be approximated by:

$$\langle \Psi_{f,\epsilon} | \mathbf{d}\hat{\mathbf{e}}_{\mathrm{ir}} | \Psi_{j,E} \rangle = \sum_{k=1}^{n} a_k^j(E) \langle \Psi_{f,\epsilon} | \mathbf{d}\hat{\mathbf{e}}_{\mathrm{ir}} | \phi_k^j \rangle = \sum_{k=1}^{n} \frac{\cos\Delta \tan\Delta_k}{\pi V_{Ek}} \langle \Psi_{f,\epsilon} | \mathbf{d}\hat{\mathbf{e}}_{\mathrm{ir}} | \phi_k^j \rangle \tag{4.20}$$

This approximation means that the relevant contribution to the continuum-continuum transition is determined by the discrete configurations in the expansion of the atomic continuum intermediate states $\Psi_{j,E}$ in equation 4.14. This is a reasonable assumption in this experimental situation. Substituting from equations 4.19 and 4.20 in the two-photon transition matrix element $P_{\mathrm{a}}^{f,j}(\epsilon, E)$ [equation 4.18] one obtains:

$$\begin{aligned} P_{\mathrm{a}}^{f,j}(\epsilon, E) &= \langle \psi_E^j | \mathbf{d}\hat{\mathbf{e}}_{\mathrm{x}} | \psi_g \rangle \cos^2\Delta \left[\sum_{k=1}^{n} p_k^{f,j} \tan\Delta_k \right] \left[\sum_{k=1}^{n} q_k^j \tan\Delta_k - 1 \right] \\ &= \langle \psi_E^j | \mathbf{d}\hat{\mathbf{e}}_{\mathrm{x}} | \psi_g \rangle \frac{\left[\sum_{k=1}^{n} p_k^{f,j} \tan\Delta_k \right] \left[\sum_{k=1}^{n} q_k^j \tan\Delta_k - 1 \right]}{1 + \tan^2\Delta}, \end{aligned} \tag{4.21}$$

with

$$p_k^{f,j} = \frac{\langle \Psi_{f,\epsilon} | \mathbf{d}\hat{\mathbf{e}}_{\mathrm{ir}} | \phi_k^j \rangle}{\pi V_{Ek}}. \tag{4.22}$$

Inserting the definitions of $\tan\Delta_k$ and $\tan\Delta$ from equation 4.9 and assuming that all transition matrix elements are real valued equation 4.21 can be expressed as:

$$P_{\mathrm{a}}^{f,j}(\epsilon, E) = D_{Eg}^j \left(\sum_{k=1}^{n} \frac{p_k^{f,j}}{E_k^j} \right) \frac{1 + \sum_{k=1}^{n} \frac{q_k^j}{E_k^j}}{1 + \left(\sum_{k=1}^{n} \frac{1}{E_k^j} \right)^2}, \tag{4.23}$$

where the dependence of the product of dipole matrix elements on the intermediate and final state energies is determined by few parameters. $E_k^j = (E - \epsilon_k^j)/\Gamma_k^j/2$ with ϵ_k^j representing the position of the k-th resonance and Γ_k^j its width. The q_k^j represent Fano q-parameters, which depend on the transition dipole matrix elements from the

atomic ground state to the intermediate discrete configurations ϕ_k^j and to the continuum configuration ψ_E^j. D_{Eg}^j is the dipole matrix element for the transition from the ground state to the intermediate continuum configurations ψ_E^j (see ref. [59]). $p_k^{f,j}$ represent the IR-induced continuum-continuum transition matrix elements which enter equation (4.20). All the parameters are assumed to be independent of the intermediate and final state energies over the spectral widths covered by the XUV and IR laser pulses.

As relation (4.23) obviously shows, the two-photon transition matrix element to a final continuum state when a group of n intermediate Fano resonances is involved is not equal to the sum of transition matrix elements where each summand represents the two-photon transition matrix element via one individual intermediate Fano resonance. This is similar to the bound-continuum absorption cross section for the same situation [59]. Only in case where the individual resonances are well separated from each other, meaning their separations $|\epsilon_k^j - \epsilon_{k'}^j|$ are large compared to their widths Γ_k^j, $P_{\mathrm{a}}^{f,j}(\epsilon, E)$ can be approximated by such a sum as can be seen in equation 4.23. As a function of the intermediate state energy E $P_{\mathrm{k}}^{f,j}(\epsilon, E)$ has n pairs of pairwise complex conjugate poles in the complex plane off the real axis. Each pair is representable by $\bar{\epsilon}_k^j \pm i\bar{\Gamma}_k^j/2,\ k = 1, 2, ..., n$ $(\bar{\Gamma}_k^j > 0)$. Generally the $\bar{\epsilon}_k^j$ and the $\bar{\Gamma}_k^j$ will be different from the width Γ_k^j and resonance position ϵ_k^j parameters entering $P_{\mathrm{k}}^{f,j}(\epsilon, E)$ in equation 4.23. Only in the case of energetically well separated resonances they will tend to be equal.

For all reasonable laser pulses $P_{\mathrm{l}}(\epsilon, E, \delta)$ can be assumed to be an analytic function of the intermediate state energy E with the additional characteristics that, for the delay δ being larger than zero, $P_{\mathrm{l}}(\epsilon, E, \delta)$ approaches zero for $|E| \to \infty$ faster than $1/|E|$ in the lower complex plane ($\mathrm{Im}\, E \leq 0$). With these conditions fulfilled the integral over intermediate state energies in equation 4.18 can be evaluated analytically by calculating the residues of the integrand at the poles of $P_{\mathrm{k}}^{f,j}(\epsilon, E)$ in the lower complex plane. Provided $P_{\mathrm{k}}^{f,j}(\epsilon, E)$ has only simple poles the two-photon transition matrix element $T_{f,g}^{\delta}(\epsilon)$ can be represented by:

$$T_{f,g}^{\delta}(\epsilon) \approx \frac{1}{4} \sum_j \sum_{k=1}^{n} c_k^j(\epsilon) \exp[-i\delta(\bar{\epsilon}_k^j - i\bar{\Gamma}_k^j/2)], \tag{4.24}$$

with the time delay δ being larger than zero, i. e. the IR pulse following the XUV pulse. The delay time only appears in the exponential functions entering the sum thus giving rise to each summand consisting of the product of an oscillatory term $\exp(-i\bar{\epsilon}_k^j\delta)$ and a term $\exp(-\bar{\Gamma}_k^j\delta)$ decreasing exponentially with the delay time due to finite resonance lifetimes. According to equation 4.24 the general form of the two-photon transition probability to a final continuum state becomes:

$$\begin{aligned} |T_{f,g}^{\delta}(\epsilon)|^2 \quad \approx \quad & \sum_{\alpha=1}^{M} b_{\alpha,\alpha}(\epsilon) \exp(-\bar{\Gamma}_\alpha \delta) + \\ & \sum_{\substack{\alpha,\beta=1 \\ \alpha<\beta}}^{M} b_{\alpha,\beta}(\epsilon) \cos[(\bar{\epsilon}_\alpha - \bar{\epsilon}_\beta)\delta + \phi_{\alpha,\beta}(\epsilon)] \exp[-(\bar{\Gamma}_\alpha + \bar{\Gamma}_\beta)\delta/2], \end{aligned} \tag{4.25}$$

where the double sum in equation 4.24 has been suitably renumbered. The $\bar{\Gamma}_\alpha$ are twice the imaginary part and $\bar{\epsilon}_\alpha$ the real parts of the poles of $P_{\mathrm{a}}^{f,j}(\epsilon, E)$ in equation 4.23. The

coefficients $b_{\alpha,\beta}(\epsilon)$, which may be assumed to be positive valued are functions of the final state energy. They have a maximum values close to the final state energy $\epsilon = \epsilon_{\mathrm{g}} + \omega_{\mathrm{x}} + \omega_{\mathrm{ir}}$ with ϵ_{g} the ground state energy of the atom where the excitation process starts. The relation of the $b_{\alpha,\beta}(\epsilon)$ to the complex amplitudes $c_k^j(\epsilon)$ can be derived from equation 4.24. Similarly, the energy dependent phases $\phi_{\alpha,\beta}(\epsilon)$ are determined by these complex amplitudes.

The sum in the first term of equation 4.25 can be interpreted to represent a population loss of "bound" states due to autoionization. The corresponding decay rates are related to the imaginary parts of the poles of $P_{\mathrm{a}}^{f,j}(\epsilon, E)$. The damping of the amplitudes of the oscillating contributions in the sum in the second term may be thought of as a loss of coherence in the coherent "bound" wavepacket motion due to this autoionization. The rate of this loss of coherence is proportional to the sum of the amplitude decay rates $(\Gamma_\alpha + \Gamma_\beta)/2$ of the corresponding "bound" states involved.

Equation 4.25, which represents the delay dependence of the two-photon ionization probability, will be used to analyze and approximate the experimental data with the parameters entering this equation used as adjustable values (see also [9]). Specifically, we use

$$S(\delta) = \int d\epsilon \left| T_{f,g}^{\delta}(\epsilon) \right|^2 \tag{4.26}$$

where the integration is done over the whole range of continuum kinetic energies where photoelectrons are detected after the two-photon absorption. A relation similar to equation 4.25, characterizing the delay dependence of photoelectron spectra, has been derived using the strong-field approximation for the interaction of the IR laser pulse with the atom in reference [65].

Finally, the relation (4.24), with the delay time δ only appearing in the exponential function, is a consequence of the poles of $P_{\mathrm{k}}^{f,j}(\epsilon, E)$ [relation (4.23)] being simple ones. In case $P_{\mathrm{k}}^{f,j}(\epsilon, E)$ comprises of a higher order pole the corresponding exponential function in 4.24 gets multiplied by a polynomial in the delay time δ of the order of this pole minus one. This will have a significant effect on the dependence of the two-photon transition probability 4.25 on the time delay δ. It may, for example, result in a delayed development of a maximum in $|T_{f,g}^{\delta}(\epsilon)|^2$ as a function of δ.

4.2 Experimental setup

The experimental setup described in chapter 3 is used for acquiring the data presented in this chapter. For easier understanding of the experimental results, this section describes the experimental details related to the experiment presented here.

Figure 4.3 shows the Xe excitation scheme relevant to the measurements presented in this chapter. High harmonics of the Ti:Sapphire laser radiation are generated by focusing the output beam of the Ti:Sapphire laser system (see section 3.1 for more details about the laser system) in a Kr gas medium. From the generated harmonics only H_{15} and H_{17}, i. e. harmonics of orders 15 and 17, are of interest in this experiment. The corresponding photon energies are respectively, 23.31 eV and 26.41 eV. The bandwidths of these individual harmonics were approximately 100 meV as estimated from the measured width of photoelectron kinetic energy distributions from photoionizing xenon gas with

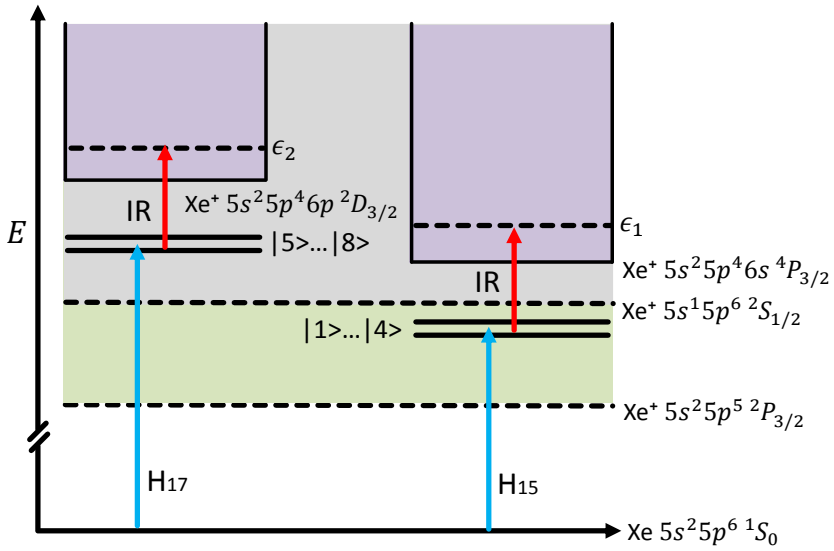

Figure 4.3: The Xe atom excitation scheme investigated in this experiment. The H_{15} ($E_{H_{15}} = 23.31\,\text{eV}$) harmonic pulse starts a wavepacket comprising several Fano resonances slightly below the threshold of ionizing an electron from the $5s$ shell. At the same time H_{17} ($E_{H_{17}} = 26.41\,\text{eV}$) launches a continuum wavepacket encompassing also a number of Fano resonances well above this threshold. The resonances lying within the bandwidths of the these harmonics (H_{15} and H_{17}) are listed in table 4.1. The time evolution of each of the launched wavepackets is then probed with a further continuum-continuum transition induced by a delay-controlled IR pulse to a final continuum $\epsilon_{1,2}$ where photoelectrons are detected.

these harmonics. The directions of polarization of the harmonic and infrared beams were chosen to be parallel. Xe atoms are supplied by means of an effusive expansion of Xe gas through a capillary. The capillary is aligned such that this atomic beam crosses the laser focus at right angles. The laser beam focus is aligned to be as close as possible to the magnetic tip to obtain the best resolution in the TOF spectrum. The Xe background pressure in the ionization chamber was adjusted to be around $1.6 \times 10^{-6}\,\text{mbar}$. It is important to keep this pressure as low as possible to avoid any space charge effects on the photoelectrons by the ions formed during ionization and to keep a much lower pressure in the flight tube.

The wavepackets in the ionization continuum of xenon are excited by the harmonics pulses H_{15} and H_{17}. As schematically depicted in figure 4.3, the fifteenth harmonic H_{15} starts a wavepacket in the Xe atom that involves Fano resonances numbered 51-58 in table 4.1. This wavepacket covers an energy range right below the ionization threshold $5s5p^6\ (^2S_{1/2})$ where one electron is removed from the inner-valence $5s$-shell. Part of the involved Fano resonances belongs to Rydberg series converging at this ionization threshold , i. e. they are brought about by one electron excited configurations. Apart from these resonances, resonances with two valence $5p$-shell electrons excited are mixed into this

no.	Configuration	J	Energy (eV)
51	$5s5p^6\left(^2S_{1/2}\right)14p$	1	23.272
52		1	23.301
53		1	23.313
54	$5p^4\left(^3P\right)6s\left(^4P_{3/2}\right)10p$	1	23.333
55	$5s5p^6\left(^2S_{1/2}\right)19p$	1	23.340
56		1	23.347
57	$5s5p^6\left(^2S_{1/2}\right)21p$	1	23.352
58	$5s5p^6\left(^2S_{1/2}\right)22p$	1	23.357
141	$5p^4\left(^3P\right)6p\left(^4D_{3/2}\right)10d$	1	26.354
142	$5p^4\left(^3P\right)6p\left(^4D_{3/2}\right)11d$	1	26.413
143	$5p^4\left(^3P\right)6p\left(^4D_{3/2}\right)12d$	1	26.454
144	$5p^4\left(^3P\right)6p\left(^4D_{3/2}\right)13d$	1	26.484

Table 4.1: The known xenon atom's Fano resonances within the bandwidths of the 15^{th} (resonance nos. 51, .., 58) and 17^{th} harmonics (resonance nos. 141, .., 144). Their energies with respect to the Xe ground state, electron configurations and resonance identification numbers are taken from [67, 68]. Not all resonances have been identified up to now.

wavepacket. The seventeenth harmonic launches a wavepacket motion which involves the resonances 141-144 in table 4.1. This wavepacket spans an energy range already higher than the Xe $5s5p^6\,(^2S_{1/2})$ ionization threshold and beyond several thresholds where one $5p$-valence shell electron is removed and a second one remains in a bound, excited state of Xe^+ (figure 4.3). Thus only Fano resonances which have two valence $5p$ electrons excited are found within the spectrum of the harmonic H_{17}. The evolution of each of these wavepackets is then tracked in time through inducing a continuum-continuum transition by absorption of an infrared (IR) Ti:Sapphire laser photon from a delayed IR pulse (figure 4.3). The pulse energy of the IR probe pulse is chosen in a range of up to $\approx 15\,\mu$J. The TOF of the photoelectrons created in the focus is detected using the MBES described in section 3.5. In this experiment we are looking for photoelectrons in the Xe ionization channels $5s5p^6$ or $5s^25p^4nl$ with $n > 5$. Therefore, since the probe IR photon has an energy of 1.55 eV, we expect that the photoelectrons are found in a kinetic energy range below 1.55 eV in the photoelectron spectrum. Therefore, the adjustments and alignment of the MBES were optimized for an optimum resolution in the low energy part of the TOF spectrum of the generated photoelectrons. The measurements presented here were performed using delay time scans with a step width of 8.2 fs and a data acquisition time of 250 s for every time delay. Since the wavepackets started here by the XUV pulses cover more than two Fano resonances, other than an exponential decay due to autoionization, we expect to observe coherences in the evolution in time of such a wavepacket [65, 66, 9]

4.3 Experimental Results

From the detected photoelectron distributions, only the part of the photoelectron yield, which critically depends on the delay time between the XUV and IR laser pulses, is of interest in this experiment. Two distinct ranges of the kinetic energy, where the photoelectron yield significantly depends on the delay time between the XUV and IR laser pulses, are found. These two kinetic energy ranges are shown in figures 4.4(a) and (b), respectively. The photoelectron yield is shown for two different delay times. Figure 4.4(a) shows this signal at negative delay (gray curve) [$\delta_1 = -172\,\text{fs}$] where the IR pulses arrive prior to the XUV ones and at positive delay [$\delta_2 = 50\,\text{fs}$] where the IR pulses follow the XUV ones, while figure 4.4(b) shows the same signal at a different kinetic energy of the photoelectrons for the same negative delay and with a positive delay time of [$\delta = 74\,\text{fs}$]. In both figures 4.4(a) and (b) a clear enhancement of the photoelectron yield in the ranges marked with (red) data markers is observed for positive delay times, i. e. when the IR pulse follows the XUV one. The widths of the spectral ranges, where the photoelectron yield enhancement is observed, approximately corresponds to the bandwidth of the individual harmonics.

4.3.1 Identification of the resonances involved in the wavepackets

The lowest order of harmonics of the pulse train generated in the Kr gas and passing through the aluminum filter to the interaction chamber is the harmonic 11 with a photon energy of 17.09 eV, while the 19^{th} harmonic with a photon energy of 29.51 eV is the highest order harmonic which passes into this chamber, however, with a very weak intensity. Hence, this harmonic is not expected to contribute significantly to the photoelectron spectrum in the low kinetic energy ranges shown in figure 4.4. A significant contribution to the interaction with the Xe atoms is therefore only expected from H_{11} - H_{17}. Photoionization of a Xe valence electron by these harmonic pulses with the Xe^+ ion core left in the lowest electronic states $5s^25p^5$ ($^2P_{3/2}$, $^2P_{1/2}$) does not contribute to the low kinetic energy photoelectron spectra shown in figure 4.4(a) and (b), since the photoelectrons from these main ionization channels of Xe have a significantly higher kinetic energy due to the small ionization potentials involved, namely 12.13 eV and 13.44 eV, respectively [69]. In the same way one-photon ionization of Xe by the harmonic H_{17} leaving the Xe^+ ion core in a state with one electron removed from the $5s$-shell, i. e. with an ionic electron configuration $5s5p^6$, also does not contribute to the photoelectron spectra in figure 4.4(a) and (b). The kinetic energy of these photoelectrons would be $\approx 3\,\text{eV}$, according to the corresponding ionization potential of 23.4 eV [69].

However, one-photon ionization of the Xe atom by the harmonic H_{17} with the Xe^+ ion left in excited states with electron configurations $5s^25p^4nl$, where one electron is removed from the 5p shell and a second one is left in an excited bound orbital (nl), may contribute to the photoelectron spectra in figures 4.4(a) and (b). Possible excited orbitals nl are $6s$, $5d$, and $6p$. In the energy interval between the $5s5p^6$ ionization threshold at 23.4 eV and the photon energy of the harmonic H_{17} (26.41 eV) there are many Xe ionization thresholds found which are based on these Xe^+ electron configurations [69]. Just these thresholds are responsible for a significant background photoelectron yield found in figures 4.4(a) and (b) spread out over the whole spectra. This photoelectron background is independent

of the delay time between the XUV and IR pulses. The photoelectron yield for negative delay times in the figures 4.4(a) and (b) represents this background. The photon energy of the harmonic H_{15} (23.31 eV) is right below the $5s5p^6$ ionization threshold, which is the lowest one above the thresholds $5s^25p^5$ ($^2P_{3/2}$, $^2P_{1/2}$). Therefore, this ionization threshold ($5s5p^6$) does not contribute to the photoelectrons in the low kinetic energy range.

The photoelectron yield enhancement in figure 4.4(a) (kinetic energy interval: $\approx 1.2\,\text{eV} - \approx 1.3\,\text{eV}$) when the IR follow the XUV pulses is generated by the absorption of one XUV and one IR photon. It depends critically on the delay time between these pulses. Moreover, the yield enhancement critically depends on the intensity of the harmonic H_{15}. This yield enhancement maximizes provided the intensity of H_{15} is maximized by adjusting the harmonic generation for optimum H_{15} output even if the harmonic H_{17} is generated at a reduced level. Thus this enhancement is attributed to the absorption of one H_{15} photon followed by the absorption of an IR photon.

The center photon energy of the harmonic H_{15} (23.31 eV) is only slightly (100 meV) lower than the ionization threshold that leaves the Xe^+ ion in the lowest excited electron configuration $5s5p^6$ (23.4 eV) where one electron is removed from the $5s$ inner valence orbital. Within the bandwidth of this harmonic, several Fano resonances are found, see table 4.1. Table 4.1 lists all resonances within this bandwidth which have been observed experimentally in [67, 68], which are the only high resolution measurements of the Xe absorption cross section close to the $5s5p^6$ ionization threshold available. The resonances listed in the first column of table 4.1 are numbered according to the numbering used in [67, 68]. A theoretical analysis of these resonances has been done recently in [70] in an energy range partly covering the range where the harmonic H_{15} excites the Xe atom. The three resonances nos. 52, 53 and 56 have not been identified up to the time of writing this thesis. Except one, all other resonances, which have been identified, belong to a Rydberg series $5s5p^6\,(^2S_{1/2})\,np$, which converges at the ionization threshold $5s5p^6\,(^2S_{1/2})$.

The principal quantum numbers n involved range from $n = 14$ up to $n = 21$. Only those with $n = 14, 19 - 21$ have actually been identified using experimental data [67, 68]. They are listed in table 4.1. The position of the other resonances of this Rydberg series within the bandwidth of H_{15} can only be estimated using the quantum defects of the known members of this series [67, 68, 70]. The assignment made to the Fano resonance with identification number 54 in table 4.1 can only be viewed as being tentative [67, 68, 70].

Absorption of an IR photon by the continuum wavepacket started by the harmonic H_{15}, which encompasses the Fano resonances introduced in the previous paragraph, gives rise to the photoelectrons observed with a kinetic energy centered at $\approx 1.25\,\text{eV}$ in figure 4.4(a) with an energy spread of $\approx \pm 50\,\text{meV}$. This kinetic energy excludes the Xe^+ excited state $5s5p^6\,(^2S_{1/2})$ from being the corresponding ionization threshold. The Xe ionization threshold which would give rise to photoelectrons in the kinetic energy range where we observe them corresponds to the Xe^+ excited state $5s^25p^4\,(^3P)\,6s\,(^4P_{5/2})$ using the notation in reference [70]. Since there are no photoelectrons observed after 2-photon absorption with a kinetic energy which would correspond to $5s5p^6\,(^2S_{1/2})$ being the ionization threshold we may conclude that the Fano resonances corresponding to the Rydberg series $5s5p^6\,(^2S_{1/2})\,np$ $(n = 14, ..., 21)$ do play a minor role in the 2-photon ionization process of Xe with the harmonic H_{15} involved. As will be shown below the observed evolution in time of the wavepacket supports this conclusion.

With arguments similar to those presented above it is possible to attribute the photo-

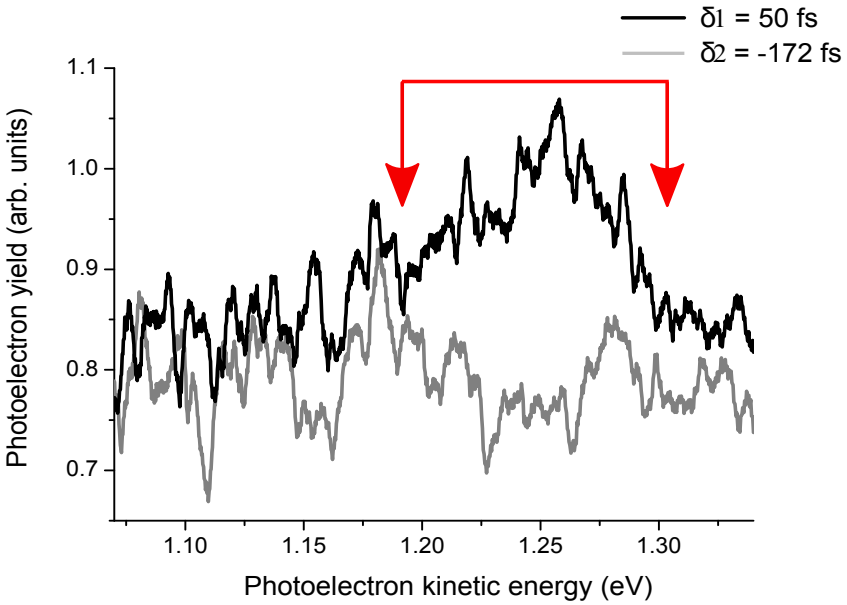

(a)

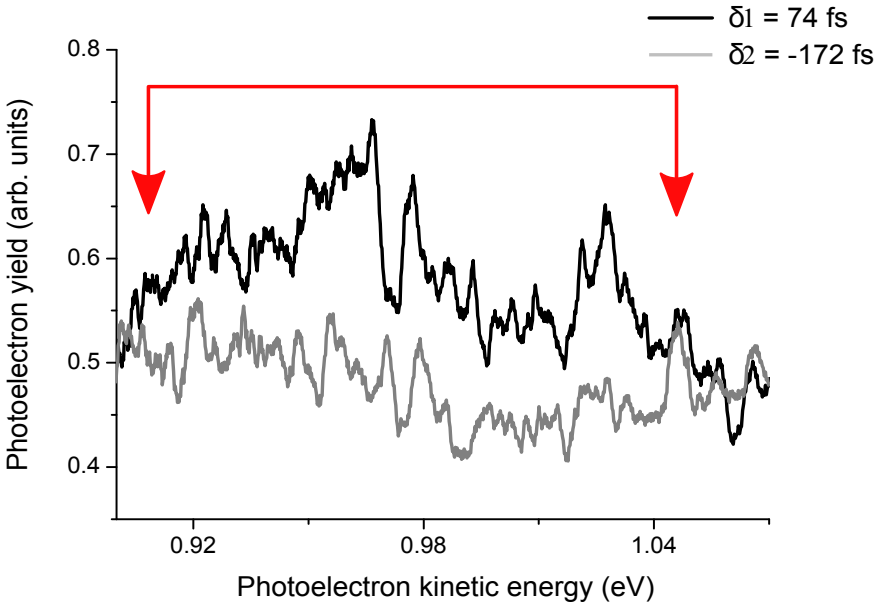

(b)

Figure 4.4: Photoelectron kinetic energy distributions in the energy ranges where photoelectrons from two-photon ionization of xenon are detected. In (a) the Xe atom absorbs one harmonic H_{15} followed by a further absorption of one infrared photon. In (b) the absorption of one H_{17} is followed by the absorption of one IR photon. Both distributions, (a) and (b), are shown at two delay times of the IR relative to the harmonic pulses (gray curves: at a delay $\delta = -172\,\text{fs}$; black curves: (a) for $\delta = 52\,\text{fs}$, (b) for $\delta = 74\,\text{fs}$). For the positive delay times the IR follow the harmonic pulses.

electron yield enhancement found in figure 4.4(b) for the IR pulses following the XUV ones to the absorption of one harmonic H_{17} photon followed by one IR photon. The harmonic H_{17} ($E_{H_{17}} = 26.41\,eV$) starts a continuum wavepacket in an energy range already significantly above the Xe ionization threshold $5s5p^6\,(^2S_{1/2})$ at 23.4 eV. Within the bandwidth of H_{17} we therefore find Fano resonances corresponding to electron configurations where two electrons are excited. The corresponding Rydberg series converge to ionization thresholds $5s^25p^4nl$ with $nl = 5d$ or $n \geq 6$. According to [67, 68] four Fano resonances are expected to be found within the spectral range of H_{17}. They are also listed in table 4.1 and are numbered 141 - 144 in the first column of the table, again according to the resonance numbering in [67, 68]. Codling and Madden tentatively assigned these resonances to be members of a Rydberg series $5s^25p^4\,(^3P)\,(6p)\,(^4D_{3/2})\,nd$ with the principal quantum numbers n ranging from 10 to 13 and ionization limit $5s^25p^4\,(^3P)\,6p\,(^4D_{3/2})$ at 26.61 eV [67, 68]. At this energy references [69, 71] locate the ionization threshold $5s^25p^4\,(^3P_2)\,6p\,(^2P_{3/2})$. Thus, the resonances more reasonably may be assigned to a Rydberg series $5s^25p^4\,(^3P_2)\,6p\,(^2P_{3/2})\,nd$.

The kinetic energy of the photoelectrons after 2-photon absorption of one H_{17} and one IR photon is spread over an energy range from $\approx 0.92\,eV$ to $\approx 1.03\,eV$ (figure 4.4(b)). This allows two excited Xe^+ states to be the final ionization channels after 2-photon absorption. They are the states $5s^25p^4\,(^3P_0)\,6p\,^2[1]^0$, $J = 1/2$ and $5s^25p^4\,(^1D_2)\,5d\,^2[3]$, $J = 5/2$ (notation according to [69]) with the corresponding Xe ionization potentials being 27.06 eV and 26.89 eV, respectively [69, 72]. Both of them may contribute to the photoelectron yield we observe.

4.3.2 The evolution in time of the wavepackets

In order to track the coherent dynamics of the atomic electrons in time we measure the yield of photoelectrons at different delay times for an accessible interval of delay times of the IR with respect to the XUV pulses of 1100 fs. Zero delay time means optimum overlap in time of the XUV and IR pulses and was determined in the same measurement by measuring the cross correlation of the IR and XUV pulses. This cross correlation curve is shown in figure 4.5. It is directly accessible via photoelectron sidebands, which are generated by absorption of one harmonic photon followed by one IR photon absorption or stimulated emission in the main Xe photoionization channel where one electron is removed from the $5p$ orbital (ionization channel $5s^25p^5\,(^2P_{1/2},\,^2P_{3/2})$) [14]. The shown cross correlation curve corresponds to the sideband 12 with the harmonics 11 and 13 contributing.

Figures 4.6(a) and (b) show the dependence of the photoelectron yields, integrated over the kinetic energy ranges marked in figures 4.4(a) and (b), respectively, on the time delay of the IR with respect to the high order harmonic pulses. Positive delay times in figure 4.6 mean the IR pulses follow the harmonic pulses. In both figures, 4.6(a) and 4.6(b), the black connected dots with the error bars represent the respective measured photoelectron yields corresponding to the absorption of one H_{15} and one IR photon [figure 4.6(a)] or one H_{17} followed by one IR photon [figure 4.6(b)].

Figures 4.6(a) and (b) both show similar characteristic features in the delay time interval covered by the experiment. The photoelectron yield reaches a maximum slightly delayed with respect to time zero, with this delay being somewhat larger in figure 4.6(b)

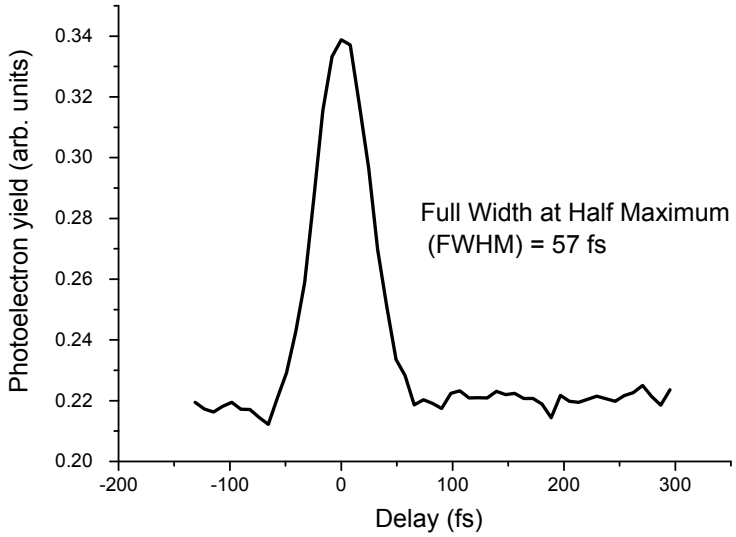

Figure 4.5: The cross correlation trace of the 11th and 13th harmonic and IR pulses. The optimum overlap (maximum photoelectron yield) in time indicates zero delay between these pulses.

than in (a). The rise of the yield at zero delay is also slightly less steep in figure 4.6(b) than it is in 4.6(a). The maximum is followed by a mean decrease of the yield with increasing time delay in a time interval up to ≈ 600 fs. On the average the photoelectron yield then becomes constant up to the largest accessible delay time at a level which is significantly higher than the background level, specifically in figure 4.6(b). The quite substantial background level of photoelectrons can be identified in the figures for negative time delays where the IR precede the harmonic pulses. As explained in the previous section these background photoelectrons are generated by one XUV-photon ionization of Xe by harmonics of order larger than H_{15} present in the beam. A further feature observed is an oscillatory structure superimposed on the overall monotonic decrease of the photoelectron yield with the time delay. As perceptible in the figures, the amplitude of this structure is larger than the noise level, represented by the error bars which were determined by taking the standard deviation at the time-delay independent part of the photoelectron spectrum from the same measurement. This oscillatory structure is caused by the coherent evolution in time of the wavepackets started by the harmonics H_{15} (in figure 4.6(a)) and H_{17} (in figure 4.6(b)), respectively, in the ionization continuum due to the presence of several Fano resonances within their spectral widths (see equation 4.25 above for the expected dependence of the ionization probability on the pump-probe time delay).

The shortest oscillation period which can be observed in the experiment is limited by the temporal width of the IR laser pulses. This oscillation period corresponds to the largest energy difference between Fano resonances lying within the bandwidth of the

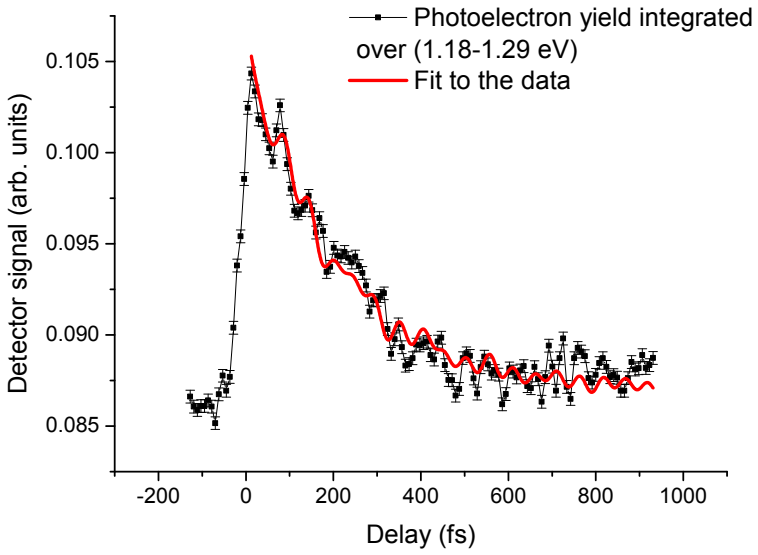

(a)

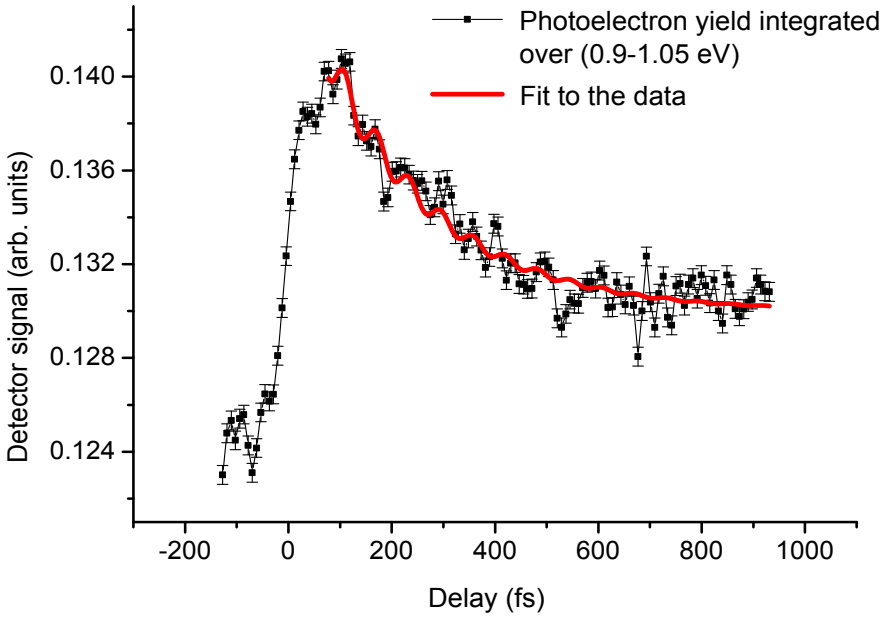

(b)

Figure 4.6: Measured XUV-IR delay-time dependences of the photoelectron yields in the kinetic energy ranges between the markers shown in figures 4.4(a) and 4.4(b), respectively. (a) the dependence of the photoelectron yield on the delay of the IR with respect to the harmonic H_{15} and (b) with respect to the harmonic H_{17} pulses. The black-dotted lines with the error bars represent the experimental data. The red lines reperesent fit curves which are based on the equations 4.25 and 4.26. A positive delay means the IR follow the XUV pulses.

respective harmonic. This difference approximately corresponds to the bandwidth of the individual harmonics of $\approx 100\,\mathrm{meV}$. From this bandwidth one derives $\approx 40\,\mathrm{fs}$ for this period. This value is practically equal to the width of the IR laser pulses.

A necessary precondition to detect the evolution in time of the full wavepacket started by the harmonic pulses H_{15} and H_{17}, respectively, is the existence of at least one final continuum state which can be reached after absorption of the IR probe photon with comparable probabilities from all of the Fano resonances of the Xe atom which contribute to the formation of the wavepacket. If this is not the case, or the contribution of such a final state to the whole two-photon transition probability is small, the coherent contributions to the overall transition probability will be largely suppressed, and thus also the visibility of the corresponding coherent evolution in time of the wavepacket [see equation 4.25]. If only part of the Fano resonances, which make up the wavepacket, contribute to the transition to one final state, only the coherent evolution in time of this part of the whole wavepacket can be observed in the pump-probe experiment. In the experiment presented here, we only restrict the kinetic energy of the photoelectrons contributing to the pump-probe signal. Thus, a possibly significant number of different degenerate final continuum eigenstates will contribute to the measured signal. These facts may be responsible for the smallness of the oscillatory structures, which map the coherent evolution in time of the wavepacket, observed in the experiment. The main feature observed is a mean exponential decay of the pump-probe signal, which represents a mere population decay [the first sum on the right hand side of equation 4.25] due to autoionization of the Fano resonances involved in the continuum wavepacket which is started by the XUV pulse.

The large number of Fano resonances found within the spectral bandwidths of the harmonics H_{15} and H_{17} according to previous spectroscopic investigations (Table 4.1) and their incomplete characterization hamper a full analysis of the evolution in time of the wavepackets. The basis for our analysis below is equation 4.26 above, i. e. the 2-photon transition probability [equation 4.25] integrated over the final spectral range where we detect the photoelectrons. To facilitate an analysis we will make several simplifying assumptions. We will assume that the phases $\phi_{\alpha,\beta}(\epsilon)$ appearing in the transition probability [equation 4.25] do not depend on the final state energy ϵ, i. e. the kinetic energy of the photoelectrons. They are replaced by mean values which will be used as fit parameters. A second set of fit parameters will then be the amplitudes $b_{\alpha,\beta}(\epsilon)$ of the coherent part in equation 4.25 integrated over the respective spectral kinetic energy ranges where the photoelectrons are detected.

The experimental findings shown in figures 4.6(a), (b), i. e. the course of the delay time dependence of the photoelectron yields, suggest two differing population decay rate ranges being involved. A range of high decay rates which gives rise to the initial decrease of the photoelectron yield within the time range investigated and a second one, with small decay rates, which gives rise to the residual photoelectron yield for large delay times. As a starting point we use a single rate constant to fit the initial mean decay of the experimental photoelectron yields in figures 4.6(a), (b). The best fit to the data is found with $\Gamma = 5.0 \pm 0.15\,\mathrm{ps}^{-1}$ for the decay in figure 4.6(a) and $\Gamma = 4.6 \pm 0.2\,\mathrm{ps}^{-1}$ for the one in figure 4.6(b). Trying to improve the fit by using two independently variable rate constants resulted in values for the two rates which differ by less than the error limits we get from the fitting procedure. This means that to within our experimental accuracy, the data are reasonably well represented by one decay rate constant for the initial mean

decay of the photoelectron yield.

Analysis of the electron dynamics in the wavepacket excited by H_{15}

Another interesting characteristic feature that can be extracted from the time evolution of the photoelectron yield is the coherent electron dynamics through analyzing the resonances involved in the wavepacket. The wavepacket started by the harmonic H_{15} encompasses contributions from Fano resonances attributable to the Rydberg series $5s5p^6\,(^2S_{1/2})\,np$ with $n = 14, ..., 21$ (see Table 4.1). The decay rates of these resonances may be extrapolated from known values for smaller principal quantum numbers using the relation $\Gamma(n^*)^3 \approx \text{const}$, which may be applicable [73, 74]. Here n^* is the effective principal quantum number of the respective resonance. This relation would not be applicable in case the higher n members of this Rydberg series are perturbed by other resonances. Based on $\Gamma(n^*)^3 \approx \text{const}$ and the Xe data of [73, 74] one gets $\Gamma \approx 0.72\,\text{ps}^{-1}$ for the $n = 14$ member of the Rydberg series and correspondingly smaller decay rates for the higher n members. These estimated rates are significantly smaller than the one obtained for the fast photoelectron yield decay in figure 4.6(a). Despite the fact that the difference of these rate constants and the one determined above is significantly larger than the error limits determined from the fitting routine a corresponding population decay cannot be retrieved from the data. We suspect the main reason for this being the smallness of the population of the resonances $5s5p^6\,(^2S_{1/2})\,np$ with $n = 14, ..., 21$. This is obviously in accordance with the small residual photoelectron yield enhancement found towards the end of the delay range investigated.

For extracting information about the coherent contribution to the photoelectron yield, we fit in a second step the second sum on the right hand side of equation 4.25 with the oscillatory part in figure 4.6(a). Only one fast population decay rate constant Γ was identified. However, there are 4 resonances this rate constant may be attributed to (res. nos. 52 - 54, 56 in Table 4.1). A Fourier transform of the photoelectron yield with respect to the delay time suggests four frequencies to contribute mainly to the oscillatory structure in a range $0.0045\,\text{fs}^{-1} \leq \nu \leq 0.025\,\text{fs}^{-1}$. The lower frequency limit is set by a steep rise of the magnitude of the Fourier transform towards $\nu = 0$, which masks possible oscillation frequencies in the range $\nu < 0.0045\,\text{fs}^{-1}$, and the upper limit by the bandwidth of the laser pulses which are involved. The identifiable oscillation frequencies closely resemble corresponding energy differences between pairs of Fano resonances with numbers 54/51, 57/54, 58/54 and 58/51 (see table 4.1 for the resonance numbering). More information on possible further resonance pairs contributing to the oscillatory structure in the experimental data for the wavepacket started by the harmonic H_{15} cannot be inferred from these data. This result indicates that the high population decay rate constant may be attributed to the resonance no. 54 with two $5p$-shell electrons excited. Assuming now $\Gamma(n^*)^3 = 0.81\,\text{fs}^{-1}$ (see [73, 74]) for the resonances with one $5s$-shell electron excited the best fit of equation 4.25 to the experimental data, based on the resonance pairs mentioned above, is represented by the red, solid curve in figure 4.6(a). It reproduces the course of the experimental data quite reasonably, specifically in the first half of the delay range. The main contribution to the appearance of an oscillatory structure on the fit curve towards the end of the delay range stems from the 58/51 resonance pair with both resonances being members of the Rydberg series with one $5s$-shell electron excited. For

the oscillation stemming from this resonance pair the coherence decay rate $(\Gamma_{58}+\Gamma_{51})/2$ expected from the relation $\Gamma(n^*)^3 = 0.81\,\mathrm{fs}^{-1}$ is $\sim 4.2\times10^{-4}\,\mathrm{fs}^{-1}$. This decay rate value is not detectable within our accessible delay time range.

Analysis of the electron dynamics in the wavepacket excited by H_{17}

For the second wavepacket excited by H_{17} a population decay rate constant of $\Gamma = 4.6\pm0.2\,\mathrm{ps}^{-1}$ was determined, as mentioned above, from fitting a single decay rate to the photoelectron yield in figure 4.6(b). This decay constant reproduces the fast decrease of the photoelectron yield. According to previous spectroscopic data [67, 68, 72], the Fano resonances contributing to this wavepacket are expected to belong to one Rydberg series $5p^46pnd$ with $n = 10, ..., 13$ as shown in Table 4.1, nothing else is known in this spectral range up to the time of writing this thesis.

In order to analyze a possible coherent contribution to the photoelectron yield we assume that only these resonances contribute to the wavepacket and all have the same decay rate constant $\Gamma = 4.6\,\mathrm{ps}^{-1}$. Thus we assume that Γ does not follow relation $\Gamma(n^*)^3 \approx$ const along this Rydberg series. Γ following this relation would have been detectable when we determined the population decay rate constant since the decay rate would change roughly by a factor of three from $n = 10$ to $n = 13$.

On the basis of these simplifications it is possible to retrieve a coherent contribution to the photoelectron yield at least partly. We arrive at the fit curve to the data shown in figure 4.6(b). As one would expect on the basis of the restrictions made, the fit is only reasonable for the first part of the dependence of the photoelectron yield on the delay time. The reason for this is the rate constant damping the amplitudes of the coherent contributions to the photoelectron yield being the same as the rate constant $\Gamma = 4.6\,\mathrm{ps}^{-1}$ for the population decay. The fit reveals that mainly the Fano resonance pair 142/144 (Table 4.1) gives rise to a coherent contribution to the photoelectron yield.

The analysis above did not take into account a possible coherent contribution to the photoelectron yield which may stem from the substantial yield we find towards the end of the delay time interval in figure 4.6(b). It indicates that there have to be further Fano resonances contributing to the wavepacket started by the harmonic H_{17}, which have substantially smaller population decay rate constants. These resonances do not reveal an obvious coherent contribution to the photoelectron yield in the delay time interval investigated. The reason for this behavior may be either that only one further resonance is involved, which has a small transition probability to the final state (after absorption of the IR photon) which is reached from the known resonances (Table 4.1). Or more than one further resonance is involved with energy level spacings so small that a coherent contribution would not be detectable within the accessible pump-probe delay-time range. This second scenario may apply since the bandwidth of the harmonic H_{17} spans the Xe ionization threshold identified as $5s^25p^4\,(^1D)\,5d\,(^2[4])$ in [69], thus possibly allowing the excitation of resonances corresponding to high Rydberg states ($n \gtrsim 20$) in a series converging at this threshold. From spectroscopy only the existence of the Fano resonances listed in Table 4.1 in the spectral range covered by the harmonic H_{17} is known. Our pump-probe experiment however indicates that there must be further resonances contributing within this spectral range which have not been detected in spectroscopic investigations.

4.4 Conclusion

Results presented in this chapter show experimental findings on tracking coherent two-electron dynamics in electronic wavepackets, that involved several Fano resonances, in the ionization continuum of Xe atoms. These continuum wavepackets have been excited by coherent extreme-ultraviolate (XUV) light pulses from high order harmonic generation of a Ti:Sapphire laser radiation. Their time evolution was tracked by inducing a further, continuum-continuum, transition by a delayed infrared (IR) pulse from the Ti:Sapphire laser. The time evolution of the wavepackets we have been able to observe revealed the autoionization dynamics of the wavepacket as well as the contribution of a coherent evolution in time brought about by the Fano resonances involved.

For the analysis of the experimental results we used time dependent two-photon transition probabilities derived on the basis of Fano's theory. In the specific case investigated here one continuum wavepacket which was launched by the harmonic H_{15}, covered several Fano resonances which are partly known from spectroscopic investigations. From the fitting analysis of its evolution in time (see fit equation 4.25) we were able to extract a single decay constant of $\Gamma = 5.0 \pm 0.15\,\mathrm{ps}^{-1}$ which may be assigned to one of the resonances contributing to the wavepacket and identify coherent oscillations superimposed on the wavepacket's autoionization decay. The analysis shows that one-electron excited configurations, with an inner valence $5s$-shell electron being excited, play only a minor role in this wavepacket. The dynamics seems to be influenced mainly by 2-valence-electron excited configurations. Similarly, the analysis of the time evolution of the wavepacket excited by the harmonic H_{17} indicates a single decay rate and a coherent contribution in the photoelectron yield corresponding to one pair of resonances (142/144). The resonances expected to contribute to these wavepackets are listed in table 4.1.

The analysis of the experimental data indicates that the coherent evolution in time of these wavepackets in the ionization continuum is mapped at least partly into the delay time dependence of the photoelectron yield detected in the pump-probe experiment after absorption of one XUV pump and one IR probe photon. This means that there are common final continuum states reached by pathways via at least part of the Fano resonances which contribute to the wavepackets. A complete identification of the coherent content of the dynamics has to rely on the possibility to reach at least one final state after absorption of the probe photon from all spectral components contributing to the wavepacket with similar probabilities. If this is not possible, there is only limited or possibly no access to the full dynamical evolution of the wavepacket. The experimental results show that we only had limited access to the coherent part of the evolution in time of the wavepackets launched. Reasons for this are the smallness of the coherent oscillatory structure contributing to the photoelectron yield and the limited delay range which basically did not allow to retrieve all possible contributions.

5 Phase Difference in the Photoemission from Krypton in the $^2P_{3/2}$ and $^2P_{1/2}$ Ionization Channels

Observation of ultrafast electronic dynamics accompanying the interaction of an atomic system with light in the time domain became accessible using ultrashort attosecond pulses generated from high harmonic generation. These pulses are currently the most precise trigger for timing electronic processes [1, 2, 4]. The investigation of temporal properties of photoemission from valence- and inner-shell levels in atoms is one of the hottest topics in this direction, where the time difference in emission of photoelectron wavepackets formed from different atomic subshells is obtained by employing attosecond and infrared (IR) pulses in a pump-probe detection scheme [4, 11]. (parts of this chapter have been published in [75].)

In order to rigorously define a time delay in photoionization let us assume that the atom is one-photon ionized from the initial state $|\psi_i\rangle$ to a continuum state $|\psi_l\rangle$, and that only one partial wave contributes to the wavepacket corresponding to an angular momentum l. The photoelectrons' wavepacket after the one-photon absorption will be an outgoing wavepacket and at large distance r from the ion core it takes the asymptotic form [12, 76]:

$$\lim_{r\to\infty} \psi_{l,k_0}(r,\theta,\varphi,t) = \frac{-\pi N}{r} Y_{lm}(\theta,\varphi) \int_0^\infty d\epsilon\, e^{i(k_l r - \frac{\pi l}{2} + \sigma_l(k) + \pi\mu_l(k) + ln(2kr)/k - \frac{k^2 t}{2})} D_{li}, \tag{5.1}$$

where $D_{li} = E(I_p+\epsilon)\langle\psi_l|r|\psi_i\rangle$ is the one-photon bound-free transition matrix element. $E(I_p+\epsilon)$ represents the Fourier transform of the electric field of the ionizing light pulse, with I_p the ionization potential and ϵ the photoelectron kinetic energy. $\sigma_l(k)$ is the Coulomb phase shift of the partial wave l at continuum energy $k^2/2$. This phase shift originates from the fact that the photoelectron departs the atom in the presence of the Coulomb potential of the left behind ion. $\pi\mu_l(k)$ is the short-range phase shift of the photoelectron wave function of the partial wave l due to the deviation of the ionic potential from the pure Coulomb potential [77, 12]. $Y_{lm}(\theta,\varphi)$ represents the emission angle dependent part of the wave function. The first energy derivative with respect to the photoelectron kinetic energy of the total phase shift $\delta_l(k) = \sigma_l(k) + \pi\mu_l(k)$ (i.e. $\frac{d\delta_l(k)}{kdk}$) represents a photoemission time delay which is also called Wigner time delay [78].

The phase-shift difference between photoelectrons emitted from different atomic subshells, as mentioned above, became experimentally accessible through a two-photon transition technique, reconstruction of attosecond beating by interference of two-photon transitions, named RABBITT. The basic principle of a RABBITT experiment is shown in figure 5.1. This method relies on measuring photoelectron spectra of an atom ionized by a train of high order odd-harmonics from HHG in the presence of a weak IR pulse at different temporal delays between these two fields [14]. The presence of the weak IR field induces a continuum-continuum transition through either an absorption or emission of one IR photon. This means that photoelectrons ionized by an odd-harmonic can either

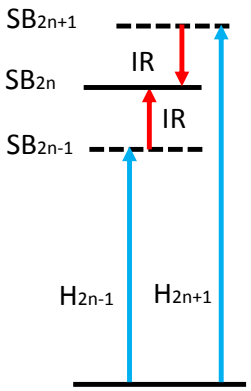

Figure 5.1: The excitation scheme with two interfering excitation pathways terminating at the same final state which is at the basis of the RABBITT technique.

absorb or emit an IR photon. The presence of two quantum paths, with one path the absorption of one harmonic H_{2n-1} photon followed by absorption of an IR-photon and the other one the stimulated emission of an IR photon following the absorption of the neighboring harmonic H_{2n+1} (see figure 5.1), terminating at the same final state leads to the appearance of what is called sidebands of photoelectrons at an order $2n$ between the two contributing harmonics. Their kinetic energies correspond to the absorption of an even number of IR photons. Moreover, these two quantum paths add up coherently.

Since the IR radiation contributes to each sideband through absorption and stimulated emission and thus with opposite phases, the sideband signal, when recorded as a function of the delay time between the XUV and IR pulses, oscillates at twice the IR frequency. A phase difference is usually observed in this oscillation of the photoelectron yield of neighboring sidebands. Two effects contribute to this phase difference, a phase difference in the two harmonic orders which contribute to the sideband and a phase difference related to the atom which is photoionized [11]. Provided photoionization of the atom by the harmonics terminates in one partial wave for the outgoing photoelectron this second phase difference can be related to the partial wave scattering phase difference at the kinetic energies corresponding to photoionization by the two harmonic orders involved in the formation of the sideband [11] (see figure 5.1). This difference in turn is then related to the Wigner time delay in photoemission [12, 78].

Apart from RABBITT, streaking [13] can be used to get time difference information on atomic photoemission. The principle of a streaking experiment is depicted schematically in figure 5.2. The atom is ionized by a single attosecond pulse in the presence of an intense IR field of a few-cycle laser pulse width. The photoelectron velocity v gets streaked by an amount that depends on the instantaneous IR electric field at the time t_0 when it is born. The photoelectron velocity measured at a detector $v_f(t)$ is then given by [1]:

$$v_f(t) = v_0 - A_L(t_0), \tag{5.2}$$

where $A_L(t) = -\int E(t')dt'$ is the vector potential of the IR laser field and v_0 the initial velocity the electron is born with due to photoionization by the attosecond XUV laser pulse. Assuming the XUV photon energy is high enough to free an electron from either

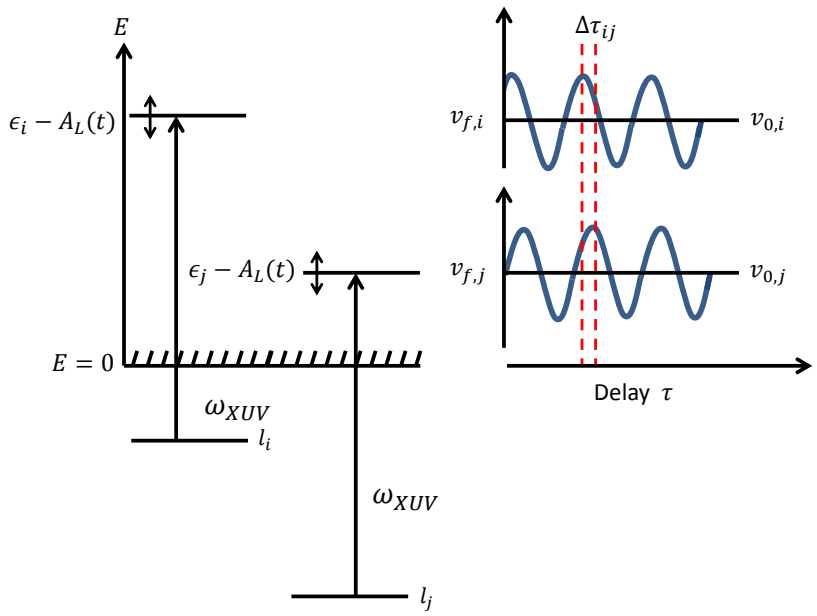

Figure 5.2: The streaking technique is based on ionizing an atom by an attosecond light pulse in the presence of an IR electric field of an ultra-short laser pulse with the temporal width of the attosecond pulse small compared to the oscillation period of the IR pulse. The photoelectron velocity after the IR pulse terminates changes depending on the value of the vector potential of the IR field at the instant of ionization by the attosecond pulse. The amount of the velocity change Δv measured at the detector thus oscillates with the time delay between the attosecond and IR pulses [13]. A time-delay difference $\Delta\tau_{ij}$ between photoelectrons emitted from different sub-shells (ϵ_i, ϵ_j) can be extracted by comparing the corresponding streaking traces. It may be interpreted as a difference in photoemission from the sub-shells.

one of two valence sub-shells (denoted l_i, l_j in figure 5.2) of the atom, the streaked photoelectron velocities measured as a function of the time delay between the XUV and IR streaking field may depend on the time delay, as shown in figure 5.2. A possible phase shift between the two oscillatory final velocities for the two ionization channels shown may then be interpreted as a time delay in photoemission from the two atomic shells involved [13]. This interpretation however is still under debate since the strong IR laser field may influence already the initial photoemission act [4].

For noble gases, results from RABBITT and streaking experiments indicate a small emission time delay difference for photoelectrons emitted from the p and those emitted from s valence orbitals [4, 11]. In neon Schultze *et al.* [4] used attosecond streaking [13] to report a difference in the photoemission time from $2p$ and from $2s$ orbitals. The difference amounts to 21 ± 5 as, meaning that photoelectrons are emitted from the s orbital prior to those from the p orbital. Klünder *et al.* [11] used the RABBITT technique [14] to study a corresponding time delay in argon for the $3s$ and $3p$ orbitals in the range

of excitation energies between 32 eV and 42 eV. This experiment shows a difference in photoemission time from these orbitals between 40 ± 10 as at a photoelectron energy of 15 eV and 110 ± 10 as at a photoelectron energy of 18 eV. Again, photoemission from the $3s$ orbital occurred prior to that from the $3p$ orbital.

The interpretation of the outcomes of the above mentioned experiments, specifically the experiments based on RABBITT, in terms of time delay differences occurring in photoionization is based on the assumption that only a single photoionization channel contributes to the photoionization step [11]. In the RABBITT experiment of Klünder et al. [11], the atomic contribution to the measured RABBITT phase shift was interpreted as a result of two contributions. One contribution originates from the continuum-continuum transition induced by the IR-field during the probe process. A second contribution is attributed to the scattering phase shift difference of the photoelectron wavepackets launched by the two harmonics which contribute to the sideband as already mentioned above [11, 12]. In case of only one partial wave for the outgoing electron contributing to the wavepacket a direct relation of this second phase shift difference to the Wigner time delay in photoionization exists [12]. In case of two or more partial waves contributing a simple relation of this second contribution to a Wigner time delay can no longer be established as was already indicated in [79].

In solids, delay time in photoelectron emission from single-crystal tungsten was measured in [10]. This measurement shows a difference in emission time of 100 as between photoelectrons emitted from localized core states and those emitted from delocalized conduction-band states. This delay time was interpreted to have a different physical origin from the one in atoms explained in the previous paragraph. The temporal shift here was attributed to the difference in the group velocities of the wavepackets, as well as to the depth below the surface of the solid where the photoelectrons are freed from the two different kinds of states.

All previous experimental investigations of a photoemission delay focused on a possible time difference in photoemission from subshells with different angular momentum quantum numbers within the valence shell of noble gas atoms or on photoemission from the valence shell of different noble gas atoms [4, 11, 15, 79]. In the analysis of these experiments no more than one partial wave contribution to the bound-continuum transition was taken into account. This allows to separate off the continuum-continuum transition induced contribution to the measured RABBITT phase and attribute the extracted residual RABBITT phase shift difference to a Wigner time delay in photoionization. On the basis of these previous results, it is interesting to experimentally look for answers to the following questions:

- What are possible limitations of the RABBITT technique in measuring the difference of photoemission times from different atomic orbitals?
- How does the continuum- continuum transition contribute to the result of the a RABBITT measurement?
- What is its dependence of the relative polarization settings of the ionizing and probing pulses, either parallel or perpendicular to each other? As will be shown a dependence would immediately indicate substantial contributions of different photoelectron partial waves to the wavepacket lauched by the ionizing XUV laser pulse.

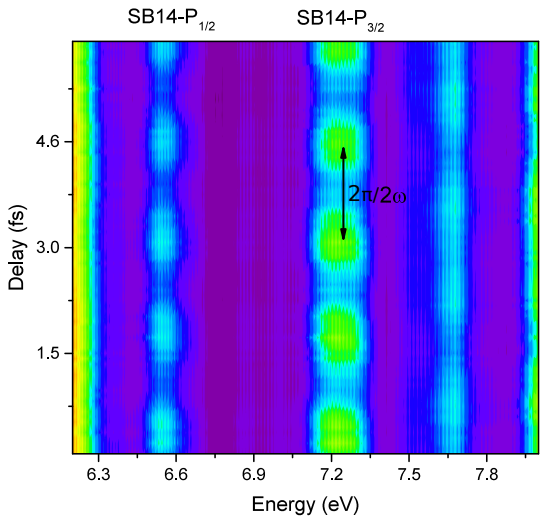

Figure 5.3: RABBITT XUV-IR delay time dependent photoelectron kinetic energy distributions oscillate at a frequency equal to 2ω, with ω the carrier frequency of the IR laser pulse.

The work in this chapter focuses on experimental evidence for answering these questions concerning the RABBITT technique [14] (see below for more details about RABBITT). The XUV-IR delay-time-dependent photolectron spectrum corresponding to sidebands between orders 12 and 18 is recorded for krypton atoms. Different from other noble gas ions Kr^+ has a fine structure splitting ($^2P_{1/2}$ and $^2P_{3/2}$) which can be resolved in the photoelectron kinetic energy distribution with our MBES when photoionizing Kr. As well the sideband photoelectron lines, split due to the ionic fine structure splitting, do not interfere with the also fine structure split lines from one-photon ionization by the XUV laser pulses. This allows to separately track their RABBITT traces. This is done for the photoelectron kinetic energy range between 4.6 eV nd 13.9 eV. The measurements are done for two settings of the polarization direction of the IR pulse with respect to that of the XUV one, either parallel or crossed. This allows to get direct insight into the contributions expected from continuum-continuum transition to the two-photon transitions leading to the photoelectron sidebands. Moreover, krypton allows a comparison of the experimentally determined RABBITT phase differences with calculated ones using experimental data for the bound-continuum dipole matrix elements and for the scattering phase shifts [77].

5.1 Background

The principle of measuring the RABBITT phase difference between photoelectrons emitted from Kr in the ionization channels $^2P_{3/2}$ and those from $^2P_{1/2}$ is schematically depicted in figure 5.5. In the two-photon transitions, which occur in RABBITT, two coherent pathways terminate at one final continuum state (see figure 5.1). The interference between

these two-photon quantum-paths appears in the photoelectron kinetic energy distribution in the sidebands in between the main photoelectron lines stemming from one-photon ionization. The photoelectron yield in these sidebands depends on the delay time between the XUV and IR pulses. If the delay between the XUV and IR pulses is varied, the photoelectron yield of this sideband will oscillate at a frequency equal to 2ω, where ω is the carrier angular frequency of the IR fundamental laser radiation.

The two-photon transition probability of detecting photoelectrons in a single sideband SB_{2n} can be written as:

$$T = \sum_f |M_{f,i}|^2. \tag{5.3}$$

The sum runs over all degenerate final states f. $M_{f,i}$ is defined by equation 2.19 in section 2.4 as:

$$M_{f,i}^{(2)}(t) \quad = \quad \sum_l \langle \phi_f | V(t') | \phi_l \rangle \langle \phi_l | V(t'') | \phi_i \rangle \times I \tag{5.4}$$

with

$$I = \int_{-\infty}^{\infty} dt' \int_{-\infty}^{t'} dt'' f(t') f(t'') e^{i(E_f - E_l)t'} e^{i(E_k - E_i)t''}, \tag{5.5}$$

here $f(t) = f_I(t) + a_x(t)\cos(\omega_x t + \phi_x)$ describes the electric fields of the IR and the XUV pulses at time t. It is assumed that $f_I(t)$ has no frequency components close to $E_l - E_i$, the energy difference between any excited state of Kr and the Kr ground state. The transition paths where the atom absorbs the IR photon first and then the XUV photon, as shown in figure 5.4(b), may therefore be neglected. On the other hand, the XUV light intensity is not high enough to induce any continuum-continuum transition. Therefore, only the time-order shown in figure 5.4(a), where the XUV photon is absorbed first is taken into account. Hence by applying the rotating wave approximation (RWA) for the transition from the Kr ground state to the ionization continuum ($E_l - E_i - \omega_x \sim 0$) one can write the integral in equation 5.5 in the form:

$$I = \frac{e^{-i\varphi_x}}{2} \int_{-\infty}^{\infty} dt' f_I(t') e^{i(E_f - E_l)t'} \int_{-\infty}^{t'} dt'' a_x(t'') e^{i(E_l - E_i - \omega_x)t''}. \tag{5.6}$$

Evaluating I in equation 5.6 leads to:

$$I \cong \frac{e^{-i\varphi_x}}{2} \lim_{\eta \to -0} \int_{-\infty}^{\infty} d\omega \tilde{a}_x(\omega) \frac{\tilde{f}_I(E_l - E_i - \omega_x - \omega)}{i(E_l - E_i - \omega_x - \omega + i\eta)}, \tag{5.7}$$

with

$$\tilde{f}_I(E_l - E_i - \omega_x - \omega) = \frac{1}{\sqrt{2\pi}} \int_{-\infty}^{\infty} dt' f_I(t') e^{i(E_l - E_i - \omega_x - \omega)t'}. \tag{5.8}$$

Substituting from equation 5.7 into equation 5.4 one can write $M_{fi}^{(2)}(t)$ as:

$$M_{f,i} = \frac{1}{4i} \left[e^{i(\omega\delta - \varphi_x^- - \varphi)} A^-(i \to f) f^- + e^{i(-\omega\delta - \varphi_x^+ + \varphi)} A^+(i \to f) f^+ \right], \tag{5.9}$$

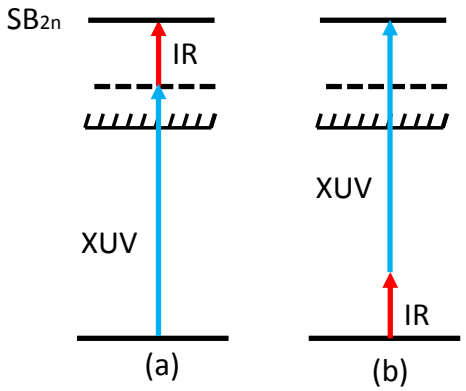

Figure 5.4: Two photon transition, (a) XUV is absorbed first and then the IR photon. In (b) this order is reversed.

with ω the frequency and φ the phase of the IR electric field which is given by:

$$f_I(t) = \hat{e}_I a_I(t-\delta)\cos\left[\omega(t-\delta)-\varphi\right]. \tag{5.10}$$

Here $a_I(t-\delta)$ is the amplitude of the IR pulse with a delay δ in time explicitly introduced. $A^{\pm}(i \to f)$ in equation 5.9 are the atomic parts of the matrix elements for the two-photon transitions depicted in figure 5.1. These transition matrix elements ($A^{\pm}(i \to f)$) are assumed to be constant over the spectral widths of the laser pulses. They can be represented by [11, 12, 80]:

$$A^{\pm}(i \to f) = \lim_{\eta \to -0} \sum\!\!\!\!\!\!\int_l \frac{\langle \psi_f | \mathbf{d}\hat{\mathbf{e}}_\mathbf{I} | \psi_l \rangle \langle \psi_l | \mathbf{d}\hat{\mathbf{e}} | \psi_i \rangle}{E_l - E_i - \omega_x^{\pm} + i\eta}, \tag{5.11}$$

the "$-$" sign is used for the pathway involving the absorption of the IR photon, the "$+$" for the transition which involves the stimulated emission of this photon. $\omega_x^{\pm} = (2n \pm 1)\omega$ being the frequencies of the two harmonics involved in the sideband. The summation and integration run over all discrete and continuum intermediate states with energies E_l of the atom. $\mathbf{d}$ is the atomic dipole operator. The carrier wave of each one of the pulses is assumed to have an individual, constant phase shift ($\varphi_x^{\pm}, \varphi$). The $f^{\pm}$ in equation 5.9 are defined to be:

$$f^{\pm} = \int_{-\infty}^{\infty} d\tilde{\omega}\; \tilde{a}_x^{\pm}(\tilde{\omega})\, \tilde{a}_I(E_f - E_i - \omega_x^{\pm} \pm \omega - \tilde{\omega}), \tag{5.12}$$

with $\tilde{a}_x^{\pm}(\omega)$ the Fourier transforms of the amplitudes of the harmonic pulses and $\tilde{a}_I(\omega)$ that of the amplitude $a_I(t)$ of the IR pulse. E_i and E_f are the energies of the initial and

final states of the atom which are coupled by the two-photon transition. Using equation 5.9, the transition probability T in equation 5.3 can be expressed as:

$$T = \sum_f |M_{f,i}|^2 = \frac{1}{16}\left\{ |f^-|^2 \sum_f |A^-(i\to f)|^2 + |f^+|^2 \sum_f |A^+(i\to f)|^2 \right. \\ \left. + 2\Re\left[f^- f^{+*} e^{-i\varphi_x^- + i\varphi_x^+ - 2i\varphi + 2i\omega\delta} \left(\sum_f A^-(i\to f) A^{+*}(i\to f) \right) \right] \right\}. \quad (5.13)$$

The terms in the first line of equation 5.13 are real values. For each individual sideband of fixed order in the two different Kr ionization channels ($^2P_{1/2}$ and $^2P_{3/2}$) φ_x^-, φ_x^+, φ and $f^- f^{+*}$ are identical and thus the RABBITT phase difference for these sidebands in the two ionization channels only depends on the phases of the corresponding sums over f in the second row of equation 5.13:

$$\phi_{sb} = \arg\left(\sum_f A^-(i\to f) A^{+*}(i\to f) \right). \quad (5.14)$$

In order to evaluate the right hand side of equation 5.11 we restrict the summation over the discrete and integration over the continuum part of the spectrum of the atomic Hamiltonian to an integration over the continuum part. This will give the main contribution since absorption of the harmonic photons directly excites continuum states. The intermediate and final continuum states are expanded into partial waves using the jj-coupling scheme:

$$\psi_{l j_e j_c}^{JM\varepsilon} = \sum_{\substack{m_e, m_c \\ m_l, m_s}} (j_e, m_e; j_c, m_c | j_e, j_c, J, M)(l, m_l; 1/2, m_s | l, 1/2, j_e m_e) \\ Y_{l m_l} \chi_{m_s} \psi_c^{j_c m_c} F_{l\varepsilon}(r). \quad (5.15)$$

Here $(j_1, m_1; j_2, m_2 | j_1, j_2, J, M)$ are Clebsch-Gordan coefficients which couple the total angular momenta j_e of the photoelectron and J_c of the ion core and the orbital angular momentum l of the photoelectron with its spin ($s = 1/2$), respectively. Y_{lm_l} are spherical harmonics and $F_{l\varepsilon}(r)$ the radial wave functions for the photoelectron in the continuum. $\psi_c^{j_c m_c}$ represents the ion core wave function and χ_{m_s} the spin wave function of photoelectron. According to the dipole selection rules, starting from the ground state of the Kr atom ($J = 0$, $M = 0$), the total angular momentum of the intermediate states is $J = 1$ and, choosing the angular momentum quantization axis along the direction of linear polarization of the XUV pulses, their magnetic quantum number is $M = 0$. Thus for the final states $M_f = 0$ for parallel and $M_f = \pm 1$ for crossed polarization of the XUV and IR beam.

The radial part of two-photon transition matrix element in equation 5.11 is evaluated using the asymptotic approximation detailed in the appendix. Using the asymptotic approximation for the continuum-continuum transition and taking into account that ionization is energetically possible by one XUV-photon absorption [80], i. e. $E_i + E_{xuv} > 0$, $A^\pm(i \to f)$ with $f = (j_{c,f}, l_f, j_{e,f}, J_f, M_f)$ can be expressed by:

$$A^{\pm}[i \to (j_{c,f}, l_f, j_{e,f}, J_f, M_f)] = \sum_{l,j_e} \frac{2}{\sqrt{k_{\pm} k_f}} \langle \frac{1}{r} \sin[\phi_{k_f,l_f}] |r| \frac{1}{r} \exp[i\phi_{k_{\pm},l}] \rangle \underbrace{\langle \psi^{10\varepsilon}_{l j_e j_c} | d | \psi_i \rangle}_{=: D^{J=1,M=0,k_{\pm}}_{l,j_e,j_{c,f}}} S^{j_{c,f},l_f,j_{e,f},J_f,M_f}_{l,j_e}. \quad (5.16)$$

The first line in equation 5.16 results from the continuum-continuum transition using the asymptotic approximation (see the appendix). $k_{\pm} = \sqrt{2\epsilon_{\pm}}$ is the continuum electron wave vector and $\epsilon_{\pm}$ its kinetic energy after the bound-continuum transition in a continuum channel characterized by the final ion core angular momentum $j_{c,f}$ which is assumed not to change during the continuum-continuum transition. k_f is the wave vector the photoelectron leaves the atom with after the two-photon transition. $D^{J=1,M=0,k_{\pm}}_{l,j_e,j_{c,f}}$ represents the dipole matrix elements associated with the bound-free one-photon transition from the ground state ψ_i to the intermediate states $\psi^{10\varepsilon}_{l j_e j_c}$ characterized by the angular momentum quantum numbers l and j_e. In our calculations these matrix elements are taken as experimental values from previous measurements which have been published in reference [77]. The coefficients $S^{j_{c,f},l_f,j_{e,f},J_f,M_f}_{l,j_e}$ in relation 5.16 represent the angular parts of the two-photon dipole transition matrix elements. These terms are responsible for a dependence of the RABBITT phases ϕ_{sb} (equation 5.14) on the relative direction of linear polarization of the harmonic and IR beams, either crossed or parallel to each other. These angular parts $S^{j_{c,f},l_f,j_{e,f},J_f,M_f}_{l,j_e}$ have the following form:

$$\begin{aligned} S^{j_{c,f},l_f,j_{e,f},J_f,M_f}_{l,j_e} = \sum_{m_s,m_c} & (j_e, -m_c; j_{c,f}, m_c | j_e, j_{c,f}, 1, 0) \\ & (l, -m_c - m_s; 1/2, m_s | l, 1/2, j_e, -m_c) \\ & (j_{e,f}, M_f - m_c; j_{c,f}, m_c | j_{e,f}, j_{c,f}, J_f, M_f) \\ & (l_f, M_f - m_c - m_s; 1/2, m_s | l_f, 1/2, j_{e,f}, M_f - m_c) \\ & \int d\mathbf{\Omega}\, Y_{l_f, M_f - m_c - m_s}(\theta, \varphi)\, d(\theta, \varphi)\, Y_{l, -m_c - m_s}(\theta, \varphi), \end{aligned}$$

where $Y_{l,m}(\theta, \varphi)$ are spherical harmonics. $d(\theta, \varphi) = \cos\theta$ or $d(\theta, \varphi) = \sin\theta \cos\varphi$ are the angular parts of the atomic dipole operator for parallel and crossed polarizations of the harmonic and IR laser pulses, respectively. The summation runs over the two electron spin angular momentum components $m_s = \pm 1/2$ and over $m_c = -j_{c,f}, -j_{c,f}+1, \ldots, j_{c,f}$. The integration runs over the whole solid angle. Equation 5.16 to within our approximation can be rewritten as:

$$A^{\pm}(i \to (j_{c,f}, l_f, j_{e,f}, J_f, M_f)) = \frac{2}{\sqrt{k_{\pm} k_f}} \sum_{l,j_e} \underbrace{\int_0^{\infty} dr\, r \sin(\phi_{k_f,l_f}(r)) \exp(i\phi_{k_{\pm},l}(r))}_{I_r} \times S^{j_{c,f},l_f,j_{e,f},J_f,M_f}_{l,j_e} D^{J=1,M=0,k_{\pm}}_{l,j_e,j_{c,f}}, \quad (5.17)$$

where I_r represents the radial integral of the continuum-continuum transition in the asymptotic approximation. This integral is evaluated in the appendix. $\phi_{k,l}(r) = kr + \ln(2kr)/k - l\pi/2 + \sigma_l(k) + \pi\mu_l(k)$ is the asymptotic phase of the radial wavefunction for a continuum electron with orbital angular momentum l, exposed to the sum of the Coulomb and a short range potential of the ion core (ion core charge: $Z = +1$). $\sigma_l(k) = \arg(\Gamma[l+1-iZk^{-1}])$ is the scattering phase shift due to the Coulomb potential of the singly charged ion core. This phase is shown in figure 5.6 for photoelectron kinetic energies in the range between $\sim 3\,\text{eV}$ and $\sim 30\,\text{eV}$ for $l = 0$ (black line) and $l = 2$ (red line). $\pi\mu_l(k)$, the additional phase shift, occurs because of an additional short range electron ion-core interaction [77]. Substituting the result of the continuum-continuum radial integral I_r from equation 7.12 (see the appendix) into equation 5.17 we obtain the final expression of $A^{\pm}(i \to (j_{c,f}, l_f, j_{e,f}, J_f, M_f))$:

$$\begin{aligned} A^{\pm}(i \to (j_{c,f}, l_f, j_{e,f}, J_f, M_f)) \quad = \quad & \frac{-i}{\sqrt{k_{\pm}k_f}} e^{i[\frac{-1}{k_f}\ln(2k_f)+\frac{1}{k_{\pm}}\ln(2k_{\pm})+\frac{\pi}{2}l_f-\sigma_{l_f}(k_f)-\pi\mu_{l_f}(k_f)]} \\ & \times \frac{1}{(k_{\pm}-k_f)^2}\sqrt{\frac{2\pi \mid \frac{1}{k_f}-\frac{1}{k_{\pm}} \mid \left[1+(\frac{1}{k_f}-\frac{1}{k_{\pm}})^2\right]}{1-e^{-2\pi\mid\frac{1}{k_f}-\frac{1}{k_{\pm}}\mid}}} \\ & \times e^{i\left\{\arg\Gamma\left[2+i(\frac{1}{k_{\pm}}-\frac{1}{k_f})\right]-(\frac{1}{k_{\pm}}-\frac{1}{k_f})\ln\mid k_f-k_{\pm}\mid\right\}} \\ & \times \sum_{l,j_e} S_{l,j_e}^{j_{c,f},l_f,j_{e,f},J_f,M_f} D_{l,j_e,j_{c,f}}^{J=1,M=0,k_{\pm}} \\ & \times e^{i[\sigma_l(k_{\pm})+\pi\mu_l(k_{\pm})-l\pi/2]}. \end{aligned} \tag{5.18}$$

This equation will be used for our numerical calculation of the RABBITT time delay differences obtained by the experiment presented in this chapter. The first line of equation 5.18 includes the total phase of the final continuum states. It involves the Coulomb long-range and short-range phase shifts. The second line represents the strength of the continuum-continuum transition induced by the absorption or emission of the IR photon and the third line in this expression describes a complex valued factor that depends on the photoelectron kinetic energy in the intermediate and final state. The fifth line includes the total phase of the intermediate continuum states which involves the Coulomb long-range and short-range phase shifts that depend on the orbital angular momentum l.

The photoelectron yields, measured in the experiment in the two ionization channels with $j_{c,f} = 1/2, 3/2$ for each sideband $2n$ do not represent a two-photon transition to one single final state of the system. Several degenerate states contribute to these photoelectron yields. Taking this into account, the measured atomic RABBITT phase differences for photoemission into the two ionization channels where the ion core is left in the states with total angular momentum $j_{c,f} = 1/2, 3/2$ in each individual sideband can be determined from equation 5.14, where the sum runs over all degenerate final states.

5.2 Experimental Procedure

The experimental results presented in this chapter are based on data acquired by using an XUV pulse train combined with IR laser pulses in a RABBITT experiment. The

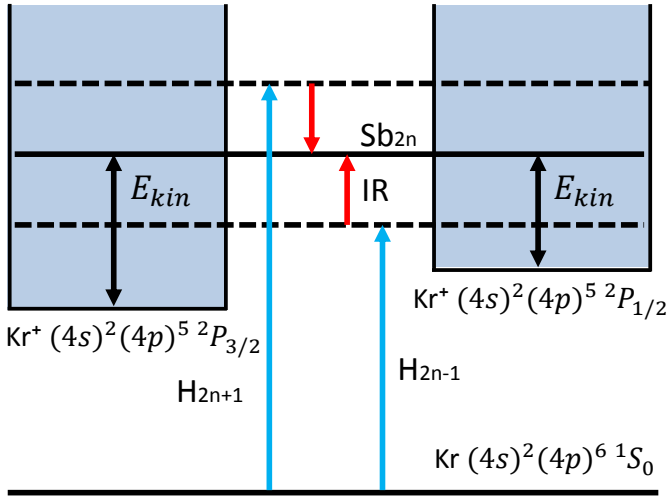

Figure 5.5: RABBITT excitation scheme of the krypton atom. The two ionization thresholds correspond to leaving the ion core either in the $^2P_{1/2}$ or in the $^2P_{3/2}$ state with a difference in the ionization potentials of 0.666 eV.

XUV pulses are high order harmonics of the laser radiation delivered by the laser system described in section 3.1. This laser delivers pulses at a central carrier frequency of $\omega = \mathrm{E_L}/\hbar$, $\mathrm{E_L} = 1.55\,\mathrm{eV}$ with a pulse energy of 2.6 mJ. Most part of the laser's output beam power is used to generate the high harmonic pulse train in argon gas with an applied Ar gas pressure between 35 and 45 mbar and at a focused light intensity of $\sim 2 \times 10^{14}\,\mathrm{Wcm^{-2}}$. The high harmonic beam is spatially and temporally overlapped with a second weak part of the IR beam to induce a two-photon transition in krypton. Krypton gas is supplied at a flow rate so as to keep the background pressure in the ionization chamber between of 1×10^{-6} and 6×10^{-6} mbar. It is important to keep this pressure as low as possible in order to obtain a high signal to noise ratio in the experiment. Krypton atoms are one-photon ionized by the XUV photons of the harmonic pulses and the freed photoelectron is probed with the low intensity IR pulses through a continuum-continuum transition. The IR intensity was estimated to be around $10^{11}\,\mathrm{Wcm^{-2}}$. The continuum-continuum transition occurs either through an absorption or stimulated emission of an IR photon by the photoelectrons. The MBES described in section 3.5 is used to measure the time of flight of the photoelectrons stemming from one- and two-photon ionization. The energy of the photoelectrons is calculated from the time of flight spectrum in a separate offline analysis. The data acquisition records photoelectron time of flight spectra at a sequence of discrete settings of the delay time between the XUV and IR pulses. The delay time between the XUV and IR pulses is controlled by the delay stage described in section 3.2. The total acquisition time at each time delay is 250 s. In order to minimize the

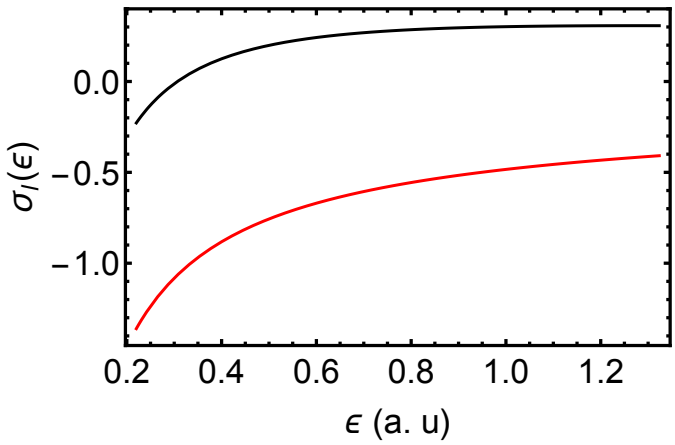

Figure 5.6: Coulomb scattering phase $\sigma_l(k)$ as a function of the photoelectron kinetic energy $\epsilon = k^2/2$ for $l = 0$ (black line) and for $l = 2$ (red line).

uncertainty in determining the RABBITT phase differences of interest here, final results are obtained by averaging over several independent measurements.

The final state in Kr reached after the two photon transition may either have the ion core in a $^2P_{3/2}$ or $^2P_{1/2}$ state. The spin-orbit splitting energy difference in Kr^+ is 0.666 eV. This allows distinguishing photoelectrons stemming from these two ionization channels and thus tracking the dependence of respective photoelectron yields on the delay-time between the XUV and IR pulses separately. Choosing krypton in this study allows a comparison of the experimentally determined RABBITT phase differences with calculated ones using experimental data for the bound-continuum dipole matrix elements and for the scattering phase shifts [77].

5.3 Experimental Results

Figure 5.7 shows the kinetic energy distribution of photoelectrons from ionization of the Kr atom by absorption of one photon from the odd high order harmonic pulses. As shown in the figure, for every harmonic two peaks of the photoelectron yield, corresponding to one-photon ionization of an electron from the $4p$ shell with leaving the ion core either in the $^2P_{3/2}$ or in the $^2P_{1/2}$ state, are clearly identified. The two ionization channels per harmonic order are energetically resolved in the spectrum up to the harmonic H_{19}. The lowest harmonic order passing through the aluminum filter and contributing noticeably to photoionization of Kr is H_{11} and the highest one contributing is the cutoff harmonic H_{23}. The resolution of the MBES was optimized for low energy photoelectrons since the RABBITT phase difference we study is expected to be more pronounced for lower energy sidebands owing to its dependence on the potential of the ionic core.

Figure 5.8 shows a photoelectron kinetic energy spectrum resulting from two-photon ionization of Kr with XUV and IR pulses set on top of each other (time delay = 0). Comparing this spectrum to the one shown in figure 5.7, one notices additional photoelectron lines corresponding to sidebands in between those lines which correspond to one photon ionization by the odd order harmonics. These sidebands result from the additional ab-

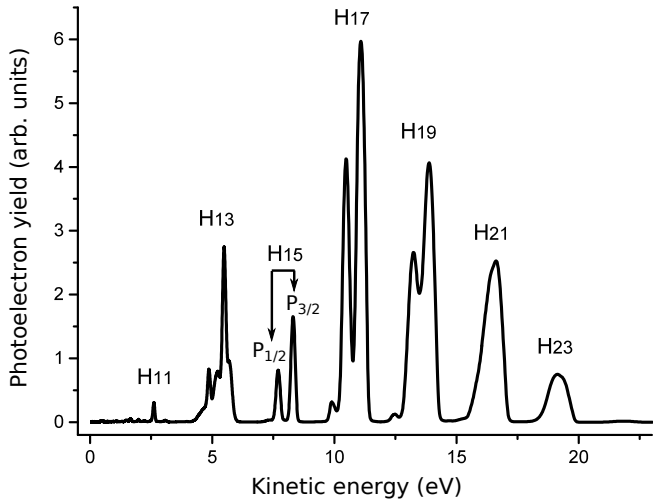

Figure 5.7: Photoelectron kinetic energy spectrum obtained by one-photon ionization of the Kr atom by high harmonic pulses. The harmonic orders responsible for each observed structure is denoted by H_{2n+1}

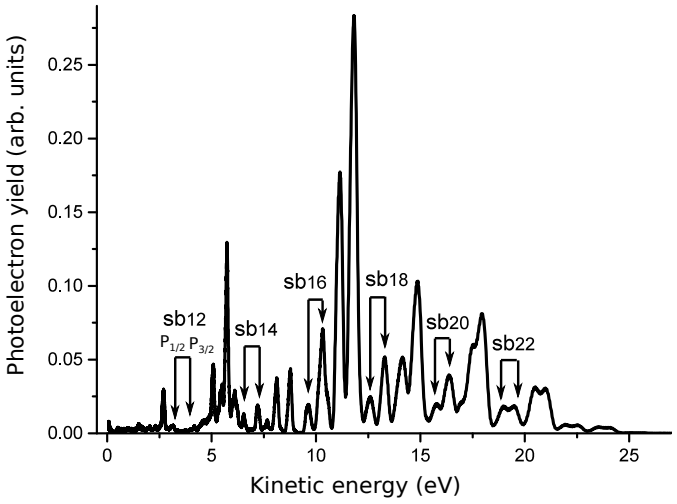

Figure 5.8: Photoelectron kinetic energy spectrum obtained from two-photon ionization of the Kr atom by overlapping the high harmonic pulses with the IR fundamental laser pulse. The sidebands sb_{2n} formed by two-photon absorption are identified in the spectrum. Each sideband signal consists of two branches stemming from the fine structure splitting in the ion.

sorption or stimulated emission of an IR photon by the photoelectron. Each sideband consists of two components from the two ionization channels which leave the ion core in either the $^2P_{1/2}$ or the $^2P_{3/2}$ state. They are clearly distinguishable from each other and from the main photoelectron lines. This allows to investigate their dependence on the delay time between the XUV-pump and IR-probe pulses individually.

The overall dependence of the spectrum shown in 5.8 on the delay time between the XUV and IR pulses, is shown in Figure 5.9. The oscillation of the photoelectron yield with the delay time between the XUV and IR pulses is shown color coded. The photoelectrons corresponding to either one of the ionization channels with the ion core left in the states $^2P_{1/2}$ and $^2P_{3/2}$ are indicated explicitly in the figure. This figure represents the typical dependence of the photoelectron spectra on the harmonic-IR pulse delay time. The shown delay time range is around 7 fs which covers $\sim$ 2.6 cycles of the IR laser pulse. Along the vertical delay time axis the typical RABBITT oscillations of the photoelectron yield in the sidebands of orders 14 to 20 are clearly visible. This means both the adjacent odd harmonics participate in these sidebands. The photoelectron yield in each sideband oscillates with the delay time according to

$$sb_{n,j_{c,f}}(\delta) = a_{n,j_{c,f}} + b_{n,j_{c,f}} \cos(2\omega\delta - \phi_n - \phi_{j_{c,f}}), \tag{5.19}$$

with $a_{n,j_{c,f}}$ and $b_{n,j_{c,f}}$ being constant coefficients independent of the delay time between the IR and XUV pulses. δ is the delay between the XUV and fundamental IR pulses. ϕ_n is a phase which depends only on the characteristics of the adjacent harmonics of orders $2n-1$ and $2n+1$ contributing to the sideband $2n$, and of the fundamental IR pulse. The additional phase $\phi_{j_{c,f}}$ with $j_{c,f} = 1/2,\ 3/2$ is determined by the atom alone in RABBITT experiment (see section 5.1 for more details about the RABBITT phase). We identify this atomic phase by the total angular momentum $j_{c,f}$ of the ion core finally reached. To each sideband pair of order $2n$, observed in the the two ionization channels with the ion core left in the states $^2P_{1/2}$ and $^2P_{3/2}$, the same harmonic pair of orders $2n-1$ and $2n+1$ contributes. Thus, any measured difference in the phases of the RABBITT oscillations of the photoelectron yields stemming from these two ionization channels just equals $\phi_{1/2} - \phi_{3/2}$, i. e. is a characteristic of the atom alone. This phase difference may be related to a time delay difference via $\tau_a = (\phi_{1/2} - \phi_{3/2})/2\omega$ [11].

Figure 5.10 shows the dependence of the total photoelectron yield of the sidebands between Sb_{12} and Sb_{18} on the delay time between the harmonic and the IR laser pulses. The shown RABBITT traces are obtained by integrating the photoelectron yield over the respective kinetic energy ranges in the photoelectron spectrum. The measurement was done with the directions of linear polarization of the harmonic and IR pulses aligned parallel to each other. Each sub-figure in figure 5.10 represents a comparison between the XUV-IR delay time dependence of the measured photoelectron yields corresponding to the two fine structure components in one sideband. Photoelectron yields stemming from the ionization channels $^2P_{1/2}$ and $^2P_{3/2}$ are represented by blue dots and black squares, respectively. The time-delay dependence of the sidebands is tracked for a delay range covering approximately 3 oscillation periods of the yield with the XUV and IR pulses close to perfect overlap in time. The two pathways contributing to each one of these sidebands are (1) absorption of one harmonic H_{2n-1} followed by absorption of one IR photon, and (2) absorption of one H_{2n+1} followed by stimulated emission of one IR

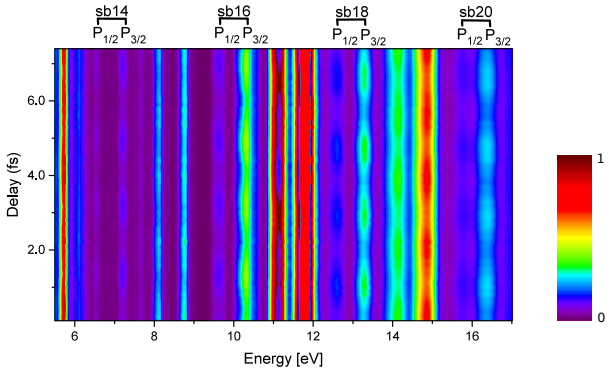

Figure 5.9: XUV-IR delay time dependence of the kinetic energy spectrum of the photoelectrons obtained from RABBITT measurements on krypton atom. The spectra shown encompass the photoelectron yield corresponding to photoionization by the harmonic orders between 13 and 21 including their respective sidebands in between. The fine structure components of each sideband and their oscillation in intensity with the time delay of the IR laser pulse with respect to the harmonics are clearly visible. The photoelectron yield is shown color coded.

photon, where $2n$ is the number of the sideband. Since both ionization channels involve the same harmonic orders any phase difference in the fit functions directly represents the atomic phase difference $\phi_{1/2} - \phi_{3/2}$. It is used to determine corresponding time delay difference $\tau_a = (\phi_{1/2} - \phi_{3/2})/2\omega$.

Figure 5.11 shows the XUV-IR delay-time dependence, similar to that shown in figure 5.10, of the photoelectron yields in the sidebnads $12-18$ for the case where the directions of linear polarization of the XUV and IR pulses are chosen to be perpendicular with respect to each other. Again each sub-figure in figure 5.11 compares RABBITT oscillations of the photoelectron yield in the two ionization channels corresponding to leaving the ion core either in the state $^2P_{1/2}$ or $^2P_{3/2}$. Red and green solid lines shown in each sub-figure in figures 5.11 and 5.10 represent global fits to the data using equation 5.19.

The extracted time delay differences for sidebands $12-18$ for the two relative polarization states of the XUV and IR pulses, parallel and perpendicular, are summarized in table 5.1. These data points represent mean values of 6 experimental runs. The time delay differences in each experimental run have been determined by fitting a Gaussian function to each maximum and minimum in the oscillatory photoelectron yield within each sideband and ionization channel. Time delay differences τ_a then have been obtained from each individual maximum and minimum position. The mean values of all these τ_a values together with the corresponding statistical standard deviations are summarized in table 5.1.

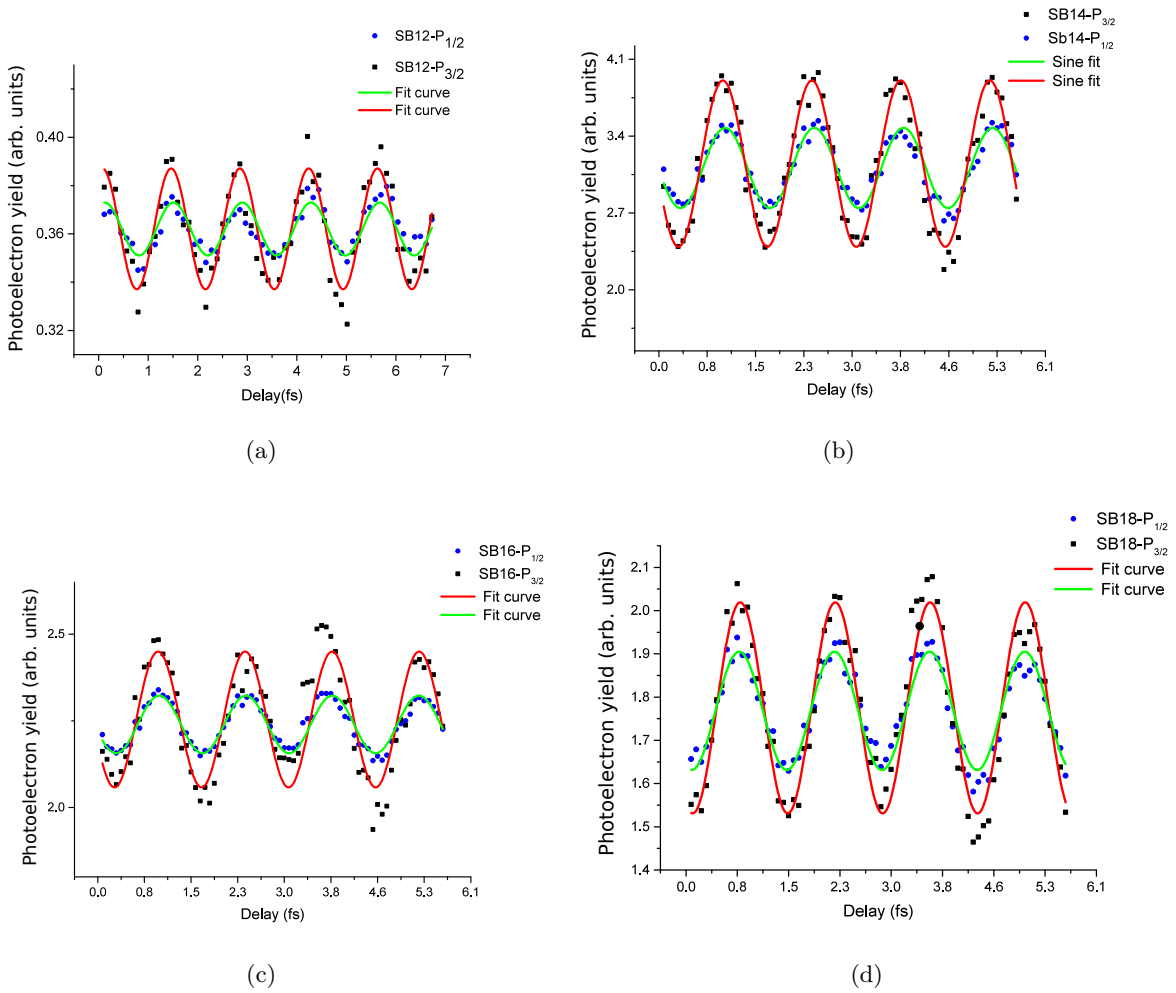

Figure 5.10: Comparison of RABBITT traces measured for the sidebands $12-18$ in the two ionization channels with the Kr ion core left in the states $^2P_{1/2}$ (blue dots) and $^2P_{3/2}$ (black squares). The axes of linear polarization of the harmonics and IR beams are chosen to be parallel.

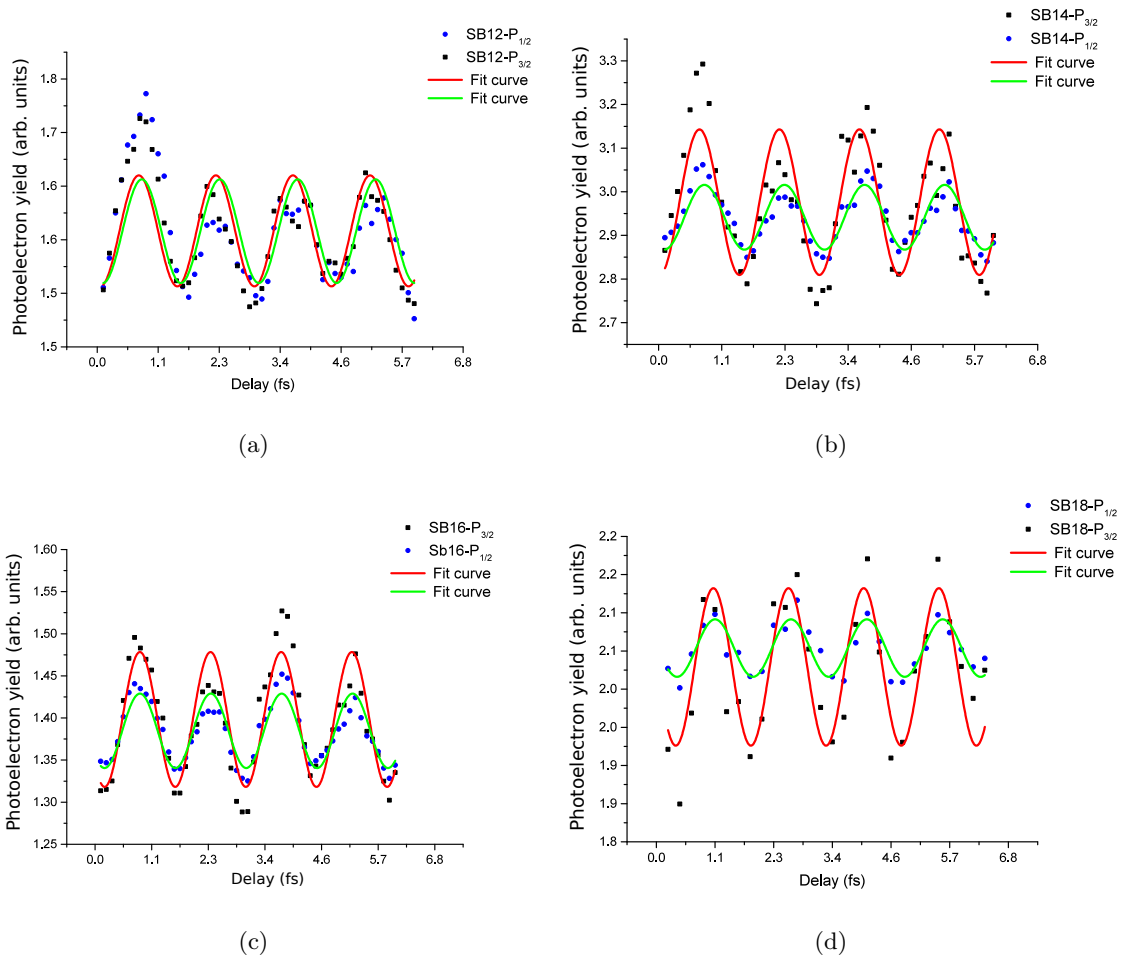

Figure 5.11: Comparison of RABBITT traces measured for the sidebands $12-18$ in the ionization channels with the Kr ion core left in the states $^2P_{1/2}$ (blue dots) and $^2P_{3/2}$ (black squares). The axes of linear polarization of the harmonics and IR beams are aligned to be perpendicular.

Figure 5.12 shows the measured time-delay differences $\tau_a = (\phi_{1/2} - \phi_{3/2})/2\omega$ for parallel and perpendicular relative directions of polarization of the XUV and IR pulses over the kinetic energy of the photoelectrons in the final ionization channel $^2P_{3/2}$ for the sideband orders $12-18$. The data points are grouped according to the directions of polarization: one group (red dots) includes the time delay differences $\tau_a^{\parallel}$ for the directions of linear polarization of the harmonic and IR pulses chosen to be parallel and the second one, $\tau_a^{\perp}$ (black squares), is for crossed beam polarizations. The lines connecting the data points are only intended to guide the eye. The time delay differences are all below 100 as and depend quite significantly on the photoelectron kinetic energy. Additionally a significant dependence of the time delay differences on the polarization states of the light pulses with respect to each other is observed. The time delay differences for crossed polarization directions are always larger than those for parallel beam polarizations. However, both

Sideband no.	Continuum energy (eV)	τ_a (|| pol.) (as)	τ_a ($\perp$ pol.) (as)
12	4.6	71± 10	86 ± 15
14	7.7	32 ± 10	62 ± 10
16	10.8	-8 ± 8	20 ± 10
18	13.9	38 ± 7	44 ± 6

Table 5.1: Time delay differences between RABBITT traces corresponding to photoelectrons emitted in the ionization channels with Kr ion core left in the states $^2P_{1/2}$ and $^2P_{3/2}$ given as $\tau_a = \tau_{P_{1/2}} - \tau_{P_{3/2}}$. The continuum energies in the second column represent the photoelectron kinetic energies in the $^2P_{3/2}$ ionization channel for each one of the sidebands $12 - 18$. The time delay differences are shown for the two states of the linear polarization directions of the two pulses, either parallel (||) or perpendicular ($\perp$) with respect to each other.

show a very similar dependence on the photoelectron kinetic energy. For both states of relative polarizations, the time delay difference τ_a has the highest values close to the ionization threshold for sideband 12 (see table 5.1). The differences both first decrease with increasing kinetic energy of the photoelectron with this trend being reversed in passing from Sb_{16} to Sb_{18}. The time delay difference measured at crossed polarization is systematically larger than that for parallel polarization by about 20 as. This shift in the time delay difference between the two states of relative polarization decreases at higher photoelectron kinetic energy.

According to the interpretation of the time delay differences derived from previous RABBITT measurements [4, 11, 12] a dependence of the time delay differences on the relative beam polarizations is puzzling at first sight. According to the physical analysis given in these papers, time delay differences should be determined exclusively by the scattering phase shifts of those atomic states which are reached in the bound-continuum transition, induced by the harmonic XUV pulses. These states actually are the same for parallel and crossed beam polarization directions if one arbitrarily fixes the quantization axis for angular momenta to point along the direction of polarization of the harmonics beam (the z-axis in what follows). Only in the following continuum-continuum transition the final states reached are different in the two cases of relative polarization: for parallel beam polarizations $M_f = 0$ final states are reached, with M_f being the magnetic quantum number corresponding to the z-component of the total angular momentum of the atomic system (ion core plus photoelectron), on the other hand, for crossed beam polarizations, $M_f = \pm 1$ final states are reached. The dependence of the two-photon transition matrix elements on the final-state magnetic quantum number M_f causes the RABBITT time delay difference to be different in the two states of relative polarization.

The observed change in the slope of the kinetic energy dependence of the time delay differences (figure 5.12) with increasing photoelectron kinetic energy may be caused by the fact that with increasing harmonic photon energy the ionization continuum becomes increasingly structured by Fano resonances which one may expect to have an effect on the scattering phase shifts and dipole matrix elements [68]. An influence can be expected to start with ionization by the harmonic 17 ($E_{H_{17}} = 26.41\,\text{eV}$). It excites the Kr atom close to two resonances based on the electron configuration $(4s)(4p)^6(6p)$. This harmonic

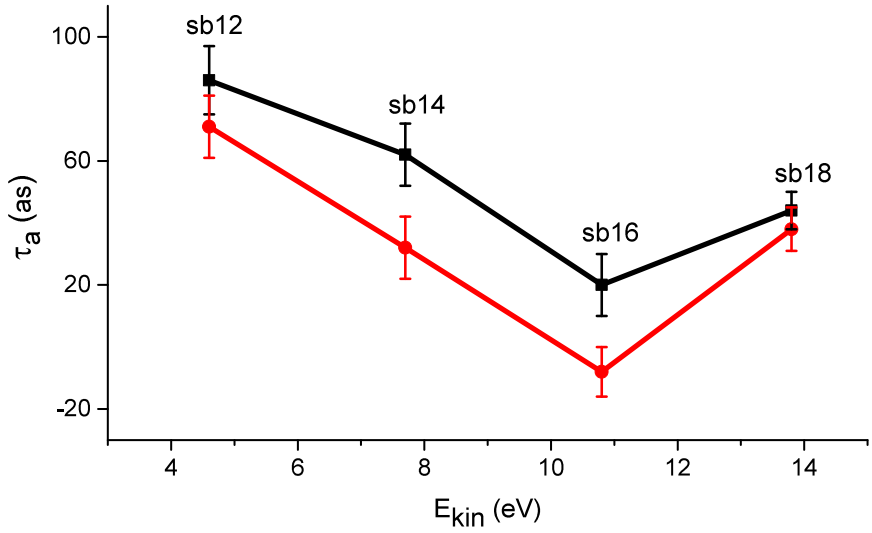

Figure 5.12: Measured time delay differences as a function of the photoelectron kinetic energy with the linear polarizations of the XUV and IR pulses parallel (red dots) and perpendicular (black squares) with respect to each other.

is involved in the sidebands 16 and 18. Even more affected by resonance structures is the Kr ionization continuum reached by the harmonic 19 ($E_{H_{19}} = 29.52\,\text{eV}$) which is involved in the formation of sideband 18. The photon energy of the harmonic 19 is higher than the threshold for ionization of an electron from the $4s$ inner valence shell with a dense manifold of two-electron excited states of the atom found beyond this threshold. Therefore, the significant increase in the measured time delay differences when passing from sideband 16 to sideband 18 may be expected to be due to this dense manifold of resonances [68].

5.3.1 Analysis: numerical calculation of time delay differences

The analysis of the presented experimental results relies on calculating the time delay differences using experimentally determined values for the dipole matrix elements of the bound-continuum transition and for the scattering phase shifts of the continuum states reached in this transition [77]. The derivation of the RABBITT phase using the two-photon transition matrix element is presented in section 5.1. For the continuum-continuum transition the asymptotic approximation (see section 5.1) is used. We also assume that the continuum-continuum transition does not change the total angular momentum of the ion core reached after the bound-free transition, i. e. $j_c = j_{c,f}$. The intermediate states reached after the bound-free transition and the final states reached after the continuum-continuum transition, are characterized using the approximate jj angular momentum coupling scheme [77]. In this coupling scheme an individual continuum

state is characterized by the set of discrete quantum numbers (j_c, l, j_e, J, M). It is also characterized by the continuous kinetic energy ϵ of the photoelectron in the ionization channel identified by the total angular momentum of the ion core j_c. J indicates the total angular momentum of the whole system, M the magnetic quantum number with respect to a suitably chosen angular momentum quantization axis, l the orbital angular momentum of the electron in the continuum and j_e its total angular momentum.

Simplifying equation 5.16 in section 5.1 leads to the final form for the two-photon transition matrix element:

$$\begin{aligned} A^{\pm}(i \to (j_{c,f}, l_f, j_{e,f}, J_f, M_f)) &= \frac{2}{\sqrt{k_{\pm} k_f}} \left(\int_0^{\infty} dr\, r \sin(\phi_{k_f,l_f}(r)) \exp\left(i\phi_{k_{\pm}}(r)\right) \right) \\ &\quad \times \sum_l \left(\sum_{j_e} S_{l,j_e}^{j_{c,f},l_f,j_{e,f},J_f,M_f} D_{l,j_e,j_{c,f}}^{J=1,M=0,k_{\pm}} \right) \\ &\quad \times \exp\left(i\delta_l(k_{\pm}) - il\pi/2\right). \end{aligned} \tag{5.20}$$

The summations in equation 5.20 run over all possible intermediate states characterized by the angular momentum quantum numbers l and j_e. $D_{l,j_e,j_{c,f}}^{J=1,M=0,k_{\pm}}$ are the dipole matrix elements associated with the bound-free transition. These dipole matrix elements are linearly interpolated from the experimental data in reference [77]. The interpolated matrix elements, which are used in our calculations of the RABBITT phase differences, are plotted in figure 5.13 over the exciting photon energy range between 15 eV and 30 eV. The transition matrix elements leaving the ion core in the state $^2P_{3/2}$ are shown in figure 5.13(a) while those leaving the ion core in the state $^2P_{1/2}$ are shown in figure 5.13(b).

All accessible intermediate and final continuum states involved in the two-photon transition are listed in tables 5.2 and 5.3. Krypton continuum states which are reached in the bound-continuum transition from the Kr ground state (total angular momentum $J_i = 0$ and $M_i = 0$) are gathered in table 5.2. The final continuum states reached upon the continuum-continuum transition starting at these intermediate states are listed in table 5.3. As mentioned above, the states are identified by the set of discrete angular momentum quantum numbers (j_c, l, j_e, J, M) using the jj angular momentum coupling scheme. The states with ion core angular momentum $j_{c,f} = 1/2$ are separated energetically from those with $j_{c,f} = 3/2$ in the photoelectron spectrum due to spin-orbit coupling in the ion core. The corresponding states are separated by a horizontal line in the two tables.

The last two columns of table 5.3 show the real valued weight factors

$$SD = \sum_{j_e} S_{l,j_e}^{j_{c,f},l_f,j_{e,f},J_f,M_f} D_{l,j_e,j_{c,f}}^{J=1,M=0,k_{\pm}} \tag{5.21}$$

of equation 5.20 above for the two states of the relative polarizations of the XUV and IR pulses at one specific value of the wavevector k which corresponds to the bound-continuum transition induced by the harmonic H_{15} with photon energy $E_{H_{15}} = 23.31$ eV. In the last but one column of table 5.3 the directions of linear polarization of the harmonic and IR laser beams are assumed to be parallel to each other, meaning $M_f = 0$. Whereas

state no.	l	j_e	j_c	J	M
1	0	1/2	3/2	1	0
2	2	3/2	3/2	1	0
3	2	5/2	3/2	1	0
4	0	1/2	1/2	1	0
5	2	3/2	1/2	1	0

Table 5.2: The discrete quantum numbers of the intermediate continuum states reached in the bound-continuum transition from the Kr ground state. The first column numbers the states from 1 to 5. The magnetic quantum number M is equal to zero since we assume the polarization direction of the harmonics beam to be parallel to the angular momentum quantization axis.

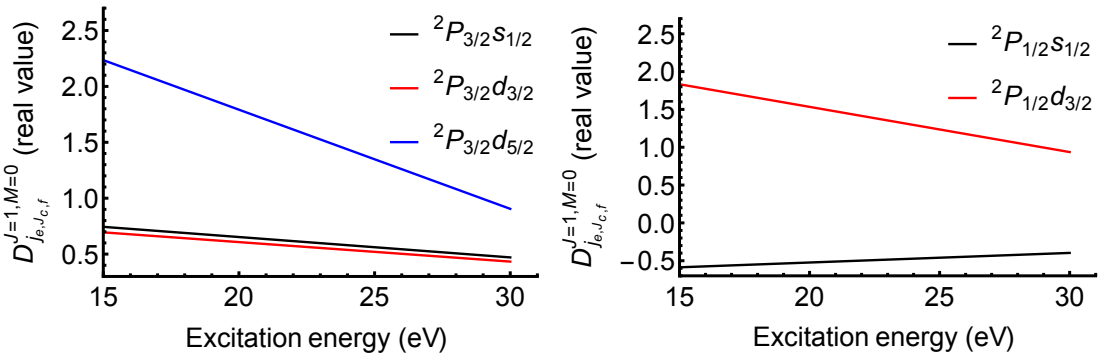

(a) (b)

Figure 5.13: The linearly interpolated dipole matrix elements of the one photon transition from the ground state of Kr atom to the ionization continuum [77]. In (a) the ion core is left in the $^2P_{3/2}$ state and in (b) in the $^2P_{1/2}$ state.

in the last column we assumed the linear polarization directions of the harmonic and IR beams are crossed, leading to $M_f = \pm 1$ and thus to final states and weight factors differing from those for parallel polarization setting. For example: the states with final total angular momentum $J = 0$ are inaccessible in the case of crossed polarizations. For each intermediate state listed in the first column of table 5.3 there exists one weight factor corresponding to this state. Therefore, in each line the weight factor ordering is according to the ordering of the intermediate states in the first column. No entry means all corresponding weight factors are zero for this specific final state. As can be seen in each line of the table, where the intermediate state numbered 1 or 4 ($l = 0$ [see table 5.2]) contributes to the two-photon transition, the weight factor of this state is of the same order of magnitude as the weight factors for the $l = 2$ intermediate states. Corresponding weight factors differ for the $j_{c,f} = 1/2$ and $j_{c,f} = 3/2$ ion core total angular momenta, i. e. for the two ionization channels investigated in the experiment. This fact means, the RABBITT time delays in the $j_{c,f} = 1/2$ and $j_{c,f} = 3/2$ ionization channels are expected to be different, i. e. $\tau_a = (\phi_{1/2} - \phi_{3/2})/2\omega \neq 0$ as observed in the experiment.

The calculated RABBITT time delays τ_a are shown in figure 5.15 . The red dashed

via	l_f	$j_{e,f}$	$j_{c,f}$	J_f	$M_f^{\parallel}$	$M_f^{\perp}$	SD ($\parallel$ pol.)	SD ($\perp$ pol.)
1, 2	1	1/2	3/2	2	0	±1	-0.2, -0.08	±0.12, ±0.05
1, 2, 3	1	3/2	3/2	0	0	forbidden	-0.2, -0.08, 0.67	forbidden
1, 2, 3	1	3/2	3/2	2	0	±1	0.2, -0.07, -0.13	±0.12, ±0.04, ±0.08
1, 2	1	1/2	3/2	1	0	±1	-	0.07, -0.14
1, 2, 3	1	3/2	3/2	1	0	±1	-	-0.15, -0.025, -0.3
2, 3	3	5/2	3/2	2	0	±1	0.23, -0.09	∓0.14, ±0.052
3	3	7/2	3/2	2	0	±1	0.71	∓0.44
2, 3	3	5/2	3/2	1	0	±1	-	-0.11, -0.1
4, 5	1	1/2	1/2	0	0	forbidden	-0.15, 0.62	forbidden
4, 5	1	1/2	1/2	1	0	±1	-	-0.11, 0.22
4, 5	1	3/2	1/2	2	0	±1	-0.2, -0.09	±0.13, ±0.052
4, 5	1	3/2	1/2	1	0	±1	-	0.08, -0.15
5	3	5/2	1/2	2	0	±1	0.63	-0.38

Table 5.3: The final continuum states reached in the continuum-continuum transition starting from the intermediate continuum states $1-5$ listed in table 5.2. In the first column the intermediate state numbers (see first column of table 5.2) are listed via which the respective final state can be reached in a dipole transition. The magnetic quantum number M_f characterizes the final state total angular momentum component along the direction of linear polarization of the XUV harmonics beam for parallel and crossed polarization settings of the harmonic and IR laser beams, respectively. The last two columns give the corresponding weight factors SD (see equation 5.21) for parallel $\parallel$ (last but one column) and crossed $\perp$ (last column) polarization directions of the XUV and IR pulses.

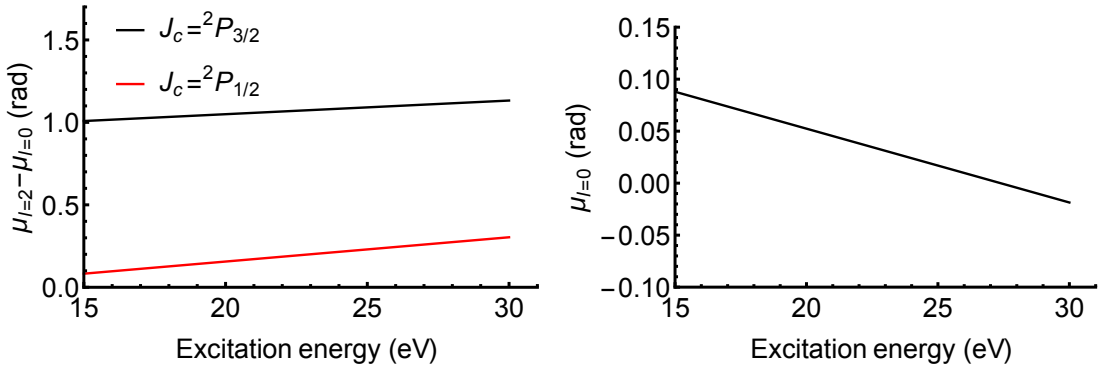

(a) (b)

Figure 5.14: The linearly interpolated scattering phase difference $\pi\mu_{l_2=2} - \pi\mu_{l_1=0}$ (a) [77], and the scattering phase $\pi\mu_{l_1=0}$ (b) [81].

curve displays the calculated $\tau_a^{||}$ for parallel and the black solid one $\tau_a^{\perp}$ for crossed polarization directions. In [77] experimental data are only available for the scattering phase differences $\pi\mu_{l_2} - \pi\mu_{l_1}$ $(l_1 = 0, l_2 = 2)$ for the ionization channels $j_{c,f} = 1/2, 3/2$. Since we need the individual scattering phases for the calculation of τ_a we use also interpolated values (see figure 5.14(b)) for $\pi\mu_0(k)$ from [81]. We find a possible inaccuracy in this scattering phase to have only a minor effect on the calculated time delay differences. However, the time delay differences react very sensitive to changes in the experimentally known scattering phase differences $\pi\mu_2(k) - \pi\mu_0(k)$. The linearly interpolated scattering phase difference $\pi\mu_{l_2} - \pi\mu_{l_1}$ is shown in figure 5.14(a) over the exciting photon energy in the range between 15 eV and 30 eV [77]. Scattering phase shifts for the finally reached continuum states, which are indeed not known, are not needed since they drop out of the calculation. In the low photoelectron kinetic energy range up to $E_{kin} \approx 5\,\text{eV}$ the calculated time delay differences rapidly decrease with increasing E_{kin} (see figure 5.15). Here both, $\tau_a^{||}$ and $\tau_a^{\perp}$, show a very similar behavior. A significant difference for the two polarization directions develops with further increasing E_{kin}. Both, $\tau_a^{||}$ and $\tau_a^{\perp}$ develop a minimum and then increase again with $\tau_a^{\perp}$ staying below $\tau_a^{||}$ for $E_{kin} \gtrapprox 5\,\text{eV}$ by $\approx 13\,\text{as}$.

5.3.2 Comparison between measured and calculated atomic RABBIT time delay differences

For a comparison with the experimental data, figure 5.16 shows both the experimental and calculated RABBITT time delay differences τ_a for both directions of polarization of the XUV relative to that of the IR pulses. There are quite significant differences observable in the characteristics of the experimental and calculated time delay differences. While the values of $\tau_a^{||}$ are smaller than those of $\tau_a^{\perp}$ for all E_{kin} in the experiment the situation is just opposite for the calculated time delay differences. In the experimental time delay differences the minimum seems to develop at a higher kinetic energy than for the calculated ones. The main discrepancies found may have their origin in the asymptotic approximation used to calculate the two-photon transition matrix elements

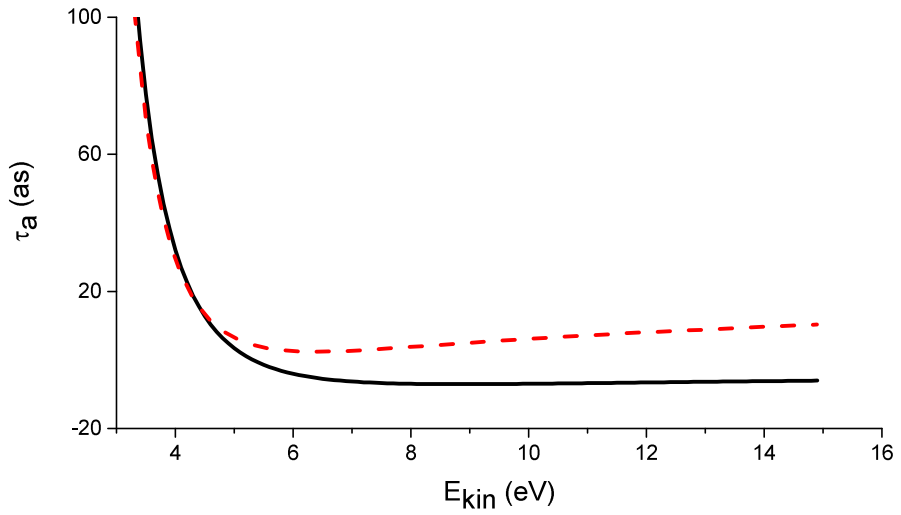

Figure 5.15: RABBITT time delay differences τ_a calculated numerically using the theoretical approach presented above as a function of the photoelectron kinetic energy. Results are shown for the directions of linear polarization of the XUV and IR pulses being either parallel (dashed red curve) or crossed (black line).

in equation 5.20 close to the Kr ionization thresholds. This asymptotic approximation breaks down at low kinetic energy because of the strong influence of the Coulomb potential on these electrons. This can be seen from the asymptotic form of the wave function (see appendix 7) which implies that only at large distance r from the core this expression gives a reasonable approximation to the full wave function [82, 11]. A comparison of the time delay differences calculated with the asymptotic approximation and those obtained by an exact calculation for the hydrogen atom is given in [11]. These calculations indicate an error caused by the asymptotic approximation of about 50 as in the photoelectron kinetic energy range between 5 eV and 10 eV (see [11] for more details). Other contributions to the discrepancies may come from the experimentally determined bound-continuum dipole matrix elements and scattering phase differences in the high energy range. In the experimental data used the effect of Fano resonances, which depends critically on the energy of the XUV harmonic photons, is not accounted for in [77]. Thus the effects originating from such structures are not reflected by the linearly interpolated data from reference [77], which are used in the calculations carried out here. Two further approximations entering equation 5.20 are the jj angular momentum coupling [1] and the assumption that the ion core angular momentum does not change, i. e. $\Delta j_c = 0$, in the continuum-continuum transition. Both these approximations may also be expected to

[1] This coupling scheme takes the ionization channels (loose-coupling states) of the ion core plus the photoelectron into account.

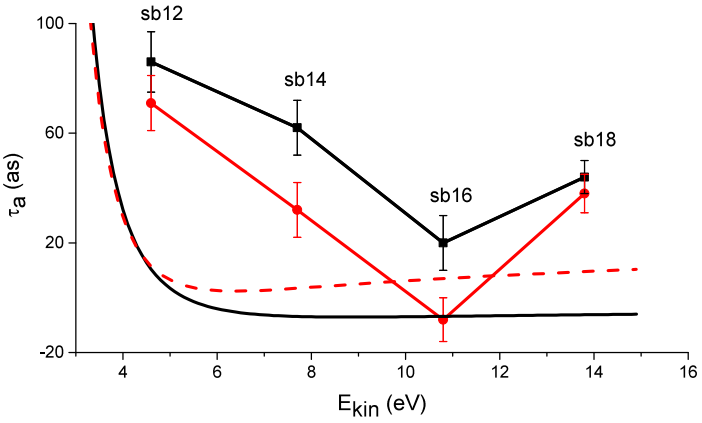

Figure 5.16: Comparison of measured and calculated RABBITT time delay differences for the photoelectrons emitted into the ionization channels $^2P_{1/2}$ and $^2P_{3/2}$. The measured and calculated time delay differences are shown for parallel (red circles and dashed red line) and crossed (black squares and black line) polarizations, respectively.

contribute to the discrepancies between the experiment and the calculations.

In order to estimate the contribution of the continuum-continuum phase difference $[\phi_{\pm}^{cc}(k_{\pm}, k_f)]_{P_{1/2}} - [\phi_{\pm}^{cc}(k_{\pm}, k_f)]_{P_{3/2}}$, with $\phi_{\pm}^{cc}(k_{\pm}, k_f)$ as defined in equation 5.25, to the total measured RABBITT phase differences, we have calculated the continuum-continuum phase differences for the sidebands between 12 and 18 and subtracted the result from the corresponding measured total phase differences. The resulting phase differences are shown in figure 5.17 for the two states of relative polarizations, i. e. the directions of linear polarization of the IR and the XUV pulses being parallel (red dots) and perpendicular (black squares).

5.3.3 Interpretation

To physically explain the reason for $\tau_a = (\phi_{1/2} - \phi_{3/2})/2\omega$ being different from zero, i. e. for a non-zero time delay difference between RABBITT traces corresponding to the ionization channels $^2P_{1/2}$ and $^2P_{3/2}$, we refer to equation 5.20. From this equation one can clearly see that the origin of the time delay differences is basically the fact that the bound-continuum transition reaches two ionization channels with different scattering phase shifts δ_l ($l = 0, 2$). This gives rise to two complex numbers $\exp[i\delta_l(k_{\pm}) - l\pi/2]$ with differing arguments, which are summed (sum over l) with real weight factors SD (the sum over j_e in equation 5.21). The summands of the sum over j_e explicitly depend on the ion core angular momenta $j_{c,f}$ (see table 5.3). These sums over j_e (SD) are therefore different for the two ion core angular momenta $j_{c,f} = 1/2,\ 3/2$ (see the SD values presented in the last two columns in table 5.3). A second contribution to the non-zero time delay differences originates from the difference in the continuum electron wave vectors $k_{\pm}$ and

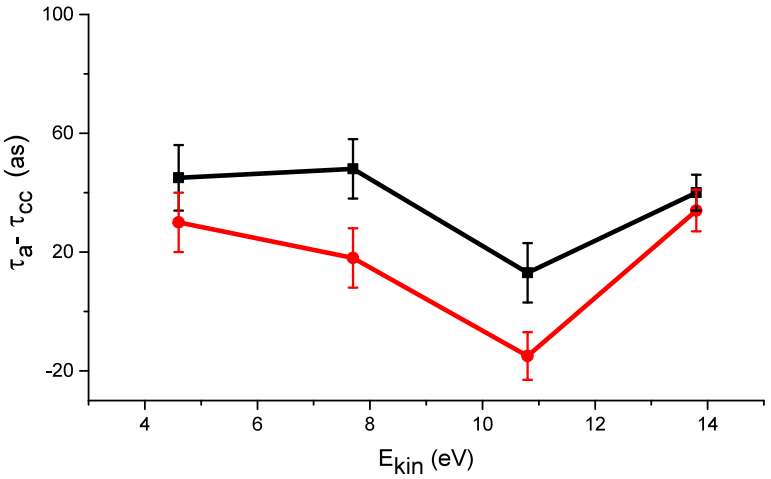

Figure 5.17: Measured time delay differences with the calculated continuum-continuum phase differences subtracted from the total measured RABBITT phase differences. The linear polarizations of the XUV and IR pulses are parallel (red dots) and perpendicular (black squares) with respect to each other.

k_f , i. e. in the different kinetic energies in the two ionization channels with ion core angular momenta $j_{c,f} = 1/2,\ 3/2$. This difference causes a difference in the dipole matrix elements for the bound-continuum transition and in the scattering phase shifts for the ionization channels $j_{c,f} = 1/2,\ 3/2$, since both depend on the photoelectron wave vectors. Both these two contributions determine the final values of the time delay difference. The non-zero RABBITT time delay difference is here not the result of removing an electron from two different orbitals but the result of different continuum "orbitals" with differing scattering phase shifts reached in the bound-continuum transition.

In a similar way the dependence of the time delay differences on the relative directions of polarization of the XUV and IR pulses occurs. At its basis are again the different scattering phase shifts in the two ionization channels with $l = 0,\ 2$ reached in the bound-continuum transition. Now the dependence of the real weight factors SD, i. e. of the sums over j_e (equation 5.21) included in the sum over l (equation 5.20), on the final state magnetic quantum number M_f causes the time delay differences for parallel polarization directions $\tau_a^{\parallel}$ to be different from those for crossed polarizations $\tau_a^{\perp}$. This difference in the real weight factors can clearly be seen from the last two columns in table 5.3 ($SD \parallel$ pol. and $SD \perp$ pol.). There, the values of these factors for every final state are listed for the two choices of polarization states. Only in case the scattering phase shifts in the ionization channels with $l = 0$ and $l = 2$ were identical or the weight factors (the sum over j_e in equation 5.20) for one of the orbital angular momenta l were negligible compared to the other one, such a dependence of the difference in the RABBITT time delays on the state of polarization of the laser pulses would not appear. The two-photon excitation pathways contributing to the sensitivity of the time delay difference τ_a to the setting of the relative

polarization can be identified in table 5.3 (first column). In this column the intermediate states contributing to the two-photon transition to each individual accessible final state are listed. Every final state reached via an $l = 0$ as well as via an $l = 2$ intermediate state contributes to τ_a depending on the relative directions of polarization of the laser pulses since the real valued weight factors SD listed in the last two columns of table 5.3 in general differ significantly.

Comparing our analysis with the interpretation and analysis of RABBITT time delay differences given in [11] one observes the decisive difference to be that in [11] only the contribution from the ionization channel $p \to d \to p$ to the final photoelectron yield is taken into account. The argument for neglecting the contribution from the ionization channel $p \to s \to p$ was the small cross section for the $p \to s$ bound-free transition compared to that of the $p \to d$ photoionization path. However, this may be a poor approximation since the bound-free dipole transition matrix elements entering the expression for the two-photon transition matrix element (equation 5.20) are proportional to the the square root of the cross section. As figure 5.13 shows the values for the $p \to s$ dipole matrix elements are approximately 30% of the largest $p \to d$ one in the whole energy range of interest to us ($\sim 17\,\mathrm{eV} \sim 30\,\mathrm{eV}$ in figure 5.13). The complexity of the contributions to the RABBITT phase shift difference in the $^2P_{1/2}$ and $^2P_{3/2}$ ionization channels can be seen from the individual contributions to the sideband signal: for the Kr atom, as schematically depicted in figure 5.18, in addition to the contribution of different ionization continua to the finally measured photoelectron yield in the corresponding sideband, another contribution results as an interference between the ionization channel $p \to d \to p$ and the ionization channel $p \to s \to p$ in this final continuum. This contribution appears as an interference term in the total two photon ionization matrix element. To make this point more clear let us write the measured sideband signal as follows:

$$S^{sb} = \sum_f A^{+*}(i \to f) A^{-}(i \to f), \tag{5.22}$$

with $A^{\pm}$ given by:

$$A^{\pm}(i \to f) = C_{\pm}(k_{\pm}, k_f) e^{i\phi_{\pm}^{cc}(k_{\pm},k_f)} \left[a^{\pm}_{l_1,J_f}(k_{\pm})\; e^{i\delta_{l_1}(k_{\pm})} + a^{\pm}_{l_2,J_f}(k_{\pm})\; e^{i(\delta_{l_2}(k_{\pm})-\pi)} \right] \tag{5.23}$$

in the specific RABBITT experiment on Kr here, S^{sb} can be expressed as (using equation 5.22):

$$\begin{aligned} S^{sb} = {} & C_{\pm}(k_{\pm}, k_f) e^{i(\phi_{-}^{cc}(k_{-},k_f) - \phi_{+}^{cc}(k_{+},k_f))} \\ & \left[\sum_{J_f} a^{+}_{l_1,J_f}(k_{+})\; e^{-i\delta_{l_1}(k_{+})} + \sum_{J_f} a^{+}_{l_2,J_f}(k_{+})\; e^{-i(\delta_{l_2}(k_{+})-\pi)} \right] \\ & \times \left[\sum_{J_f} a^{-}_{l_1,J_f}(k_{-})\; e^{i\delta_{l_1}(k_{-})} + \sum_{J_f} a^{-}_{l_2,J_f}(k_{-})\; e^{i(\delta_{l_2}(k_{-})-\pi)} \right]. \end{aligned} \tag{5.24}$$

Here $l_1 = 0$ (s-partial wave) and $l_2 = 2$ (d-partial wave). The amplitudes $a^{\pm}_{l_1,l_2,J_f}(k_{\pm})$ are real valued amplitudes which are determined by equation 5.21, i. e. (in our case) by the bound-free dipole transition matrix elements and the angle dependent part (equation

5.17) of the continuum-continuum transition matrix elements. $C_\pm(k_\pm, k_f)$ are real valued constants which depend on the intermediate and final momentum. $\phi_\pm^{cc}(k_\pm, k_f)$ are the continuum-continuum transition phases induced by an absorption (+) or emission (−) of one IR photon. These continuum-continuum phases are given by:

$$\phi_\pm^{cc}(k_\pm, k_f) = \arg\Gamma\left[2 + i(\frac{1}{k_\pm} - \frac{1}{k_f})\right] - (\frac{1}{k_\pm} - \frac{1}{k_f})\ln \mid k_f - k_\pm \mid - \frac{1}{k_f}\ln(2k_f) + \frac{1}{k_\pm}\ln(2k_\pm). \tag{5.25}$$

This equation indicates that the continuum-continuum phases depend only on the intermediate and final states momentum and therefore can be taken out of the brackets in equation 5.23. Expanding the product of the two bracketed expressions in equation 5.24 results in:

$$\begin{aligned} S^{sb} &= C_\pm(k_\pm, k_f) e^{i(\phi_-^{cc}(k_-,k_f) - \phi_+^{cc}(k_+,k_f))} \\ &\times \left[\sum_{J_f} a^+_{0,J_f}(k_+) a^-_{0,J_f}(k_-) e^{i[\delta_0(k_-) - \delta_0(k_+)]} + \sum_{J_f} a^+_{2,J_f}(k_+) a^-_{2,J_f}(k_-) e^{i[\delta_2(k_-) - \delta_2(k_+)]} \right. \\ &\left. + \sum_{J_f} a^+_{0,J_f}(k_+) a^-_{2,J_f}(k_-) e^{i[\delta_2(k_-) - \pi - \delta_0(k_+)]} + \sum_{J_f} a^+_{2,J_f}(k_+) a^-_{0,J_f}(k_-) e^{i[\delta_0(k_-) + \pi - \delta_2(k_+)]} \right]. \end{aligned} \tag{5.26}$$

The two terms in the second line of this equation represent pure s- and d-partial wave contributions, respectively. The two terms in the third line represent interference contributions from the two partial waves s and d. As an example we calculated the amplitudes and total scattering phases for the sideband order 14 with the ion core left in the state $^2P_{1/2}$. The results are substituted in equation 5.26:

$$\begin{aligned} S^{sb14}_{j_c=1/2} &= C_\pm(k_\pm, k_f) e^{i(\phi_-^{cc}(k_-,k_f) - \phi_+^{cc}(k_+,k_f))} \\ &\times \left[\left(0.08\, e^{i(0.0241)}\right)_{l_1 l_1 = 00} + \left(0.8994\, e^{i(0.3587)}\right)_{l_2 l_2 = 22} \right. \\ &\left. - \left(0.1275\, e^{i(-3.8667)}\right)_{l_1 l_2 = 02} - \left(0.1319\, e^{i(4.2504)}\right)_{l_2 l_1 = 20} \right]. \end{aligned} \tag{5.27}$$

It is obvious from this equation that the weight factors multiplying the complex exponentials in the square brackets which correspond to the interfering s- and d-pathways (the last two summands in the square brackets) are significant compared to the main pure $p \to d \to (p, f)$ pathway (second summand). This proves that the ionization channel $p \to s$ has to be taken into account in any analysis of the RABBITT time-delay difference. This in turn prevents any extraction of the scattering phase difference (Wigner time delay difference) of the d partial waves from our RABBITT measurements, since these contributions can not be separated.

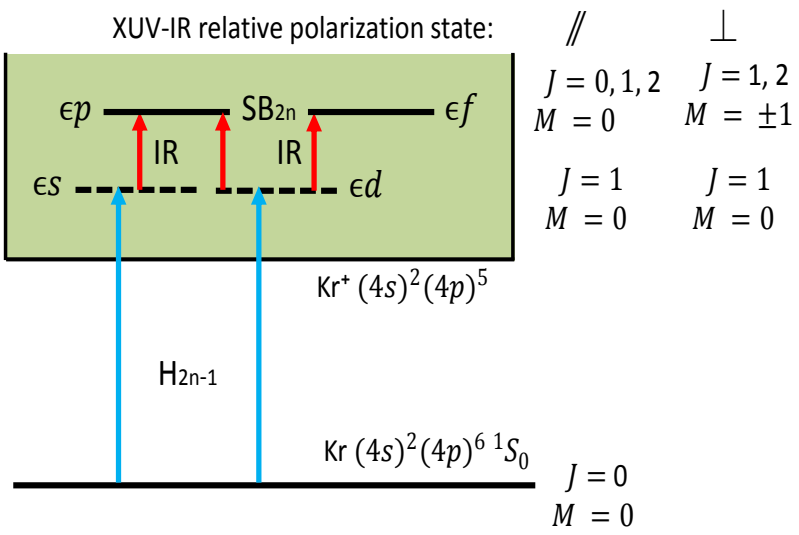

Figure 5.18: Influence of multiple channel contributions to one sideband on the delay time difference in photoemission measured in RABBITT. Two ionization channels contribute to the final photoelectron yield with different ionization continua $p \to d \to f$, $p \to s \to p$ and an interference contribution $p \to (d + s) \to p$. The presence of such multichannel contribution to the final photoelectron yield prevents to attribute the measured time delay difference to the Wigner time delay.

5.4 Conclusion

In conclusion, the experimental and calculated results presented in this chapter indicate a RABBITT time-delay difference for removing an electron from the $4p$ shell of Kr while leaving the ion core in either the state $^2P_{1/2}$ or $^2P_{3/2}$. This difference in RABBITT time delay is experimentally derived from the phase difference in the oscillatory RABBITT signal and it is calculated from phase differences of the corresponding two-photon transition matrix elements. It depends explicitly on the final continuum states as its dependency on the laser beams relative directions of polarization clearly shows. This dependence persists even if one removes that contribution to the total RABBITT phase difference attributed to the continuum-continuum transition, since this contribution depends only on the continuum electron momentum in the intermediate and final states and not on angular momenta (equation 5.23). This means that the RABBITT phase differences we revealed are not a mere result of the bound-continuum transition and thus do not directly represent a time delay difference attributable to the ionization step of the atom alone in an obvious way. The decisive reason for this is the presence of s- and d-partial waves both contributing to the continuum electron states reached after the bound-continuum transition. A direct relation between RABBITT phase shifts and corresponding Wigner time delay differences only exists provided the ionization transition reaches continuum states characterized by a single partial wave, i. e. scattering phase shift. Different RABBITT phase shifts obtained with parallel and crossed polarizations of the two laser pulses involved immediately allow one to state that differences in RABBITT phase shifts in different ionization channels do can not directly map Wigner time delay differences for the ionization step of any atomic/molecular system in a simple way.

6 Summary and outlook

This work presents results of experimental investigations of tracking atomic electron dynamics in the time domain. The investigations aimed at real-time observation of electron-electron interaction and correlation in electronic wavepackets that involve several Fano resonances. The wavepackets were launched using extreme ultraviolet (XUV) harmonic pulses in xenon atoms. Their evolution in time was probed by delayed weak infrared (IR) pulses. A second goal was the study of the RABBITT phase difference for two-photon ionization into the $^2P_{1/2}$ and $^2P_{3/2}$ ionization channels in the Kr atom.

In the first part of this thesis a real-time tracking of two-electron dynamics in electronic wavepackets excited in the ionization continuum of xenon was presented. In this experiment, XUV-light pulse trains produced by high harmonic generation were used to coherently excite electronic wavepackets that involve several Fano resonances. Specifically the harmonic 15 ($\mathrm{E_{H_{15}}} = 23.31\,\mathrm{eV}$) starts one electronic wavepacket consisting of a number of resonances of the type $5s5p^6nl$ with n in the range $14-21$ and one resonance with the configuration $5s^25p^4nln'l'$, where n and n' have the values 6 and 10 respectively. At the same time the harmonic 17 ($\mathrm{E_{H_{17}}} = 26.41\,\mathrm{eV}$) launches a second wavepacket well above the ionization threshold $5s5p^6$ where only resonances based on configurations $5p^45pnd$, with n ranging from 10 to 13, are involved. The resonances contributing to both wavepackets are listed in table 4.1. The evolution in time of the electron dynamics in each of these wavepackets, which eventually terminates in single ionization of the atom, was probed by inducing a continuum-continuum transition with a delayed infrared (IR) laser pulse. Measuring changes in the corresponding photoelectron yield as a function of the time delay between the harmonic and IR pulses made it possible not only to observe the autoionization dynamics of the wavepackets but also to track and partly identify the coherent dynamics in the time evolution of the wavepackets. The time evolution in each wavepacket shows quantum oscillations superimposed on its autoionization decay, i. e. the character of the excited electron pair may change with time, evolve into a situation where only a single inner valence shell $5s$-electron is excited, or only a single $5p$-electron. This last situation eventually terminating in autoionization. These oscillations result from the coherent interaction between electrons excited to different configurations which contribute to the wavepacket.

The experimental results are described and analyzed through two-photon transition matrix elements derived on the basis of Fano's theory. A condition for the ability to extract the full information contained in the wavepacket is that all excitation channels contributing to the wavepacket must terminate at one single final continuum with similar probabilities after the absorption of the IR-probe photon. If this is not the case it is only possible to partly map the wavepacket dynamics into the corresponding photoelectron yield detected. The analysis of the experimental results shows that there is only a limited access to the coherent part of the evolution in time of the wavepackets launched. In the analysis of the time evolution of the wavepackets, the resonances contributing to the coherent dynamics in the wavepacket as well as the widths of the strongest resonances in

each wavepacket are identified. The analysis of the evolution in time of the wavepacket launched by the harmonic H_{17}, which happens within a spectral range where one expects a dense resonance structure, must contain contributions from resonances which have not yet been revealed in spectroscopic experiments.

In the second part of this work, interference in two-photon transitions (RABBITT[1]) was employed to investigate a phase difference between RABBITT traces corresponding to photoelectrons in the $^2P_{1/2}$ and $^2P_{3/2}$ fine-structure-split ionization channels in krypton atoms. This investigation is done in the excitation energy (pump-photon energy) range $\approx 18 - 29\,\mathrm{eV}$. The measured RABBITT time-delay difference critically depends on the excitation energy specifically in the low kinetic energy range of the photoelectrons. It also exhibits a significant dependence on the relative states of the linear polarization directions of the pump and probe pulses whether they are parallel or perpendicular with respect to each other. This RABBITT time-delay difference originates from the presence of two ionization continua with differing scattering phase shifts reached upon the bound-continuum transition. Both ionization channels participate differently in the subsequent continuum-continuum probe transition. This is also the origin for the dependence of the RABBITT time-delay difference on the relative states of linear polarization directions of the pump and probe pulses. This dependence on the relative directions of polarization shows that the RABBITT time-delay differences do not give direct insight into Wigner time delay differences for the bound-continuum transition.

Calculations of time delay differences have been done on the basis of dipole matrix elements for photoionization and scattering phase shifts known for krypton atoms from former experiments. The calculated RABBITT time-delay differences show a discrepancy compared to the measured ones. This discrepancy may originate from the asymptotic approximation used to calculate the two-photon transition matrix elements close to the Kr ionization thresholds. Another contribution to this discrepancy may arise from the linearly interpolated values of the experimentally determined bound-continuum dipole matrix elements and scattering phase shift differences in the high energy range. In this energy range one expects a dense structure of Fano resonances whose possible effect is not taken into account in these interpolated values.

A limitation faced in the experiment of tracking electron dynamics in the wavepackets excited in xenon is the limited range of the accessible time delay between the pump and probe pulses. This limitation hampers the tracking of confined electron dynamics that lives longer than the accessible delay range. This limitation could be overcome by using glass wedges or alternative methods to time delay the probe pulses that allow for a longer delay time. To increase the time resolution and track electron dynamics on time scales as short as 10 fs, few-cycle laser pulses are required. Such laser pulses can be obtained by compressing the laser pulses available in our laboratory. In such a range of pulse durations it is also necessary to stabilize the carrier envelops phase (CEP) of the pulses. For the RABBITT investigation, it may be possible to get access to Wigner time delay if an angle resolved detection of the photoelectron spectrum is employed.

In this work, it was shown that, through the analysis of the presented experimental results, it is possible to real-time track ultrafast electron dynamics in many-electron atoms. This work also pointed out the limitations of using the RABBITT technique

[1] for more information about this technique see [14]

in determining Wigner time delay differences in photoemission using a concrete simple atomic system. The presented experimental results and theoretical models represent a step in pushing the frontier limits of tracking atomic electron ultrafast-dynamics and they can be used in the future as a basis to track and extract more basic knowledge about ultrafast processes in any quantum system.

7 Appendix

The approximate asymptotic behavior ($r \to \infty$ for the electron in the ionization continuum) of the perturbed and final state wave functions is used in the numerical calculations [80, 83, 12, 76]. The radial part of the two-photon transition matrix element appearing in equation 5.11 is given by [80]:

$$\begin{aligned} T_l(nl_i \to k_f l_f) &= \langle R_{l_f k_f}|r|F'_{lk}\rangle \\ &\quad + i\pi \langle R_{l_f k_f}|r|R_{lk}\rangle\langle R_{lk}|r|R_{l_i n}\rangle. \end{aligned} \tag{7.1}$$

Here it is assumed that absorption of one photon already photoionizes the electron which is assumed to be initially in an orbital characterized by the radial wave function $R_{l_i n}(r)$ (l_i: the orbital angular momentum quantum number, n: the principle quantum number). All the matrix elements which appear in equation 7.1 are real valued, since all wavefunctions involved are real valued functions of the radial coordinate r. $R_{l_f k_f}$ is the radial wave function of the final state with angular momentum l_f which in the asymptotic limit $r \to \infty$ takes the form:

$$\lim_{r\to\infty} R_{l_f k_f}(r) = \sqrt{\frac{2}{\pi k_f}} \frac{1}{r} \sin(\phi_{k_f, l_f}(r)) \tag{7.2}$$

with $\phi_{k,l}(r)$ as defined in equation 5.17 and explained in the text in section 5.1. $\sqrt{\frac{2}{\pi k_f}}$ is the normalization constant (i. e. $\int_0^\infty r^2 dr R_{lk} R_{lk'} = \delta(\frac{k^2}{2} - \frac{k'^2}{2})$). $R_{l_f k_f}(r)$ solves the following radial Schrödinger equation in the asymptotic limit $r \to \infty$:

$$\frac{d^2 R_{l_f k_f}}{2dr^2} - \left[\frac{l(l+1)}{2r^2} + V(r) - k^2/2\right] R_{l_f k_f} = 0. \tag{7.3}$$

The first term in equation 7.1 represents a transition from an intermediate state reached by absorption of one XUV photon, which is described by a perturbed radial wave function $F'_{lk}(r)$, to the final state $R_{l_f k_f}(r)$ with continuum energy $\epsilon_f = k_f^2/2$ after absorption or emission of one IR photon. The second term is purely imaginary and gives a product of two one-photon matrix elements: the transition from the initial state characterized by l_i and n to continuum intermediate states l and the transition from this state further to the final state $R_{l_f k_f}(r)$. The perturbed state $F'_{lk}(r)$ in equation 7.1 solves the following inhomogeneous differential equation [80]:

$$\frac{(k^2/2 - H_l) F'_{lk}(r)}{r} = R_{l_f k_f}(r), \tag{7.4}$$

with $H_l = -\frac{-i}{r}\frac{d}{dr} r - \frac{l(l+1)}{2r^2} - \frac{-1}{r}$. In the asymptotic limit $r \to \infty$, $F'_{lk}(r)$ takes the asymptotic form:

$$F'_{lk}(r) = \pi \sqrt{\frac{2}{\pi k}} \langle R_{l,k}|r|R_{l_i n}\rangle \cos(\phi_{lk}(r)). \tag{7.5}$$

Substituting from equations 7.5 and 7.2 in equation 7.1 one obtains the radial part of the transition matrix element as:

$$\begin{aligned} T_l(nl_i \to k_f l_f) &= \pi\sqrt{\frac{2}{k_f k}}\langle R_{l,k}|r|R_{l_i,n}\rangle \\ &\quad \underbrace{\int_0^\infty dr\ r\ e^{i\phi_{lk}(r)}\sin(\phi_{l_f,k_f}(r))}_{I_r}, \end{aligned} \tag{7.6}$$

where the integral part can be rewritten as:

$$\begin{aligned} I_r &= \int_0^\infty dr\ r\ e^{i\phi_{lk}(r)}\sin(\phi_{l_f,k_f}(r)) \\ &= \frac{1}{2i}\int_0^\infty dr\ r\left[e^{i(\phi_{lk}+\phi_{l_f,k_f})} - e^{i(\phi_{lk}-\phi_{l_f,k_f})}\right]. \end{aligned} \tag{7.7}$$

Here the first term on the right hand side, which involves the sum of the phases $(\phi_{lk} + \phi_{l_f,k_f})$ in the exponent, oscillates much faster than the second one and may be neglected. Thus one is left with the second term:

$$\begin{aligned} I_r \cong -\frac{1}{2i}\int_0^\infty dr\ r\ e^{i(\phi_{lk}-\phi_{k_f,l_f})} &\cong \frac{i}{2}e^{i[\frac{-1}{k_f}\ln(2k_f)+\frac{1}{k}\ln(2k)+\frac{\pi}{2}(l_f-l)+\sigma_l(k)-\sigma_{l_f}(k_f)]} \\ &\quad \times \underbrace{\int_0^\infty dr\, r e^{i[(k-k_f)r+ln(r)(\frac{1}{k}-\frac{1}{k_f})]}}_{I_1}, \end{aligned} \tag{7.8}$$

where I_1 can be expressed as:

$$I_1 = \lim_{\xi\to+0}\underbrace{\int_0^\infty dr\ r^{1+i(\frac{1}{k}-\frac{1}{k_f})}\, e^{i(k-k_f)r-\xi r}}_{I_\xi}. \tag{7.9}$$

Evaluating the integral I_ξ results in:

$$I_\xi = \frac{\Gamma\left[2+i(\frac{1}{k}-\frac{1}{k_f})\right]}{\left[\xi - i(k-k_f)\right]^{2+i(\frac{1}{k}-\frac{1}{k_f})}}. \tag{7.10}$$

Substituting the result of I_ξ in equation 7.9 one obtains:

$$\begin{aligned} I_1 &= \lim_{\xi\to+0}\frac{\Gamma\left[2+i(\frac{1}{k}-\frac{1}{k_f})\right]}{\left[\xi - i(k-k_f)\right]^{2+i(\frac{1}{k}-\frac{1}{k_f})}} \\ &= -\frac{\Gamma\left[2+i(\frac{1}{k}-\frac{1}{k_f})\right]\, e^{\frac{\pi}{2}|\frac{1}{k_f}-\frac{1}{k}|}\, e^{-i(\frac{1}{k}-\frac{1}{k_f})\ln|k-k_f|}}{(k-k_f)^2}. \end{aligned} \tag{7.11}$$

Simplifying this expression and putting the result into equation 7.8 one obtains the final form of I_r:

$$
\begin{aligned}
I_r \quad \approx \quad & \frac{i}{2} e^{i[\frac{-1}{k_f}\ln(2k_f)+\frac{1}{k}\ln(2k)+\frac{\pi}{2}(l_f-l)+\sigma_l(k)-\sigma_{l_f}(k_f)]} \\
& \times \frac{-1}{(k-k_f)^2}\sqrt{\frac{2\pi \mid \frac{1}{k_f}-\frac{1}{k} \mid \left[1+(\frac{1}{k_f}-\frac{1}{k})^2\right]}{1-e^{-2\pi|\frac{1}{k_f}-\frac{1}{k}|}}} \\
& \times e^{i\left\{\arg\Gamma\left[2+i(\frac{1}{k}-\frac{1}{k_f})\right]-(\frac{1}{k}-\frac{1}{k_f})\ln|k_f-k|\right\}}.
\end{aligned}
\tag{7.12}
$$

Inserting expression 7.12 into equation 7.6 the radial part of the two-photon transition matrix element takes the final form:

$$
\begin{aligned}
T_l(nl_i \to k_f l_f) \quad = \quad & \frac{\pi i}{2}\sqrt{\frac{2}{k_f k}}\langle R_{l,k}|r|R_{l_i,n}\rangle \\
& e^{i[\frac{-1}{k_f}\ln(2k_f)+\frac{1}{k}\ln(2k)+\frac{\pi}{2}(l_f-l)+\sigma_l(k)-\sigma_{l_f}(k_f)]} \\
& \times \frac{-1}{(k-k_f)^2}\sqrt{\frac{2\pi \mid \frac{1}{k_f}-\frac{1}{k} \mid \left[1+(\frac{1}{k_f}-\frac{1}{k})^2\right]}{1-e^{-2\pi|\frac{1}{k_f}-\frac{1}{k}|}}} \\
& \times e^{i\left\{\arg\Gamma\left[2+i(\frac{1}{k}-\frac{1}{k_f})\right]-(\frac{1}{k}-\frac{1}{k_f})\ln|k_f-k|\right\}}.
\end{aligned}
\tag{7.13}
$$

Bibliography

[1] F. Krausz and M. Ivanov, "Attosecond physics," *Rev. Mod. Phys.*, vol. 81, pp. 163–234, 2009.

[2] M. F. Kling and M. J. J. Vrakking, "Attosecond electron dynamics," *Annu. Rev. Phys. Chem.*, vol. 59, pp. 463–492, 2008.

[3] M. Drescher, M. Hentschel, R. Kienberger, M. Uiberacker, V. Yakovlev, A. Scrinzi, T. Westerwalbesloh, U. Kleineberg, U. Heinzmann, and F. Krausz, "Time-resolved atomic inner-shell spectroscopy," *Nature*, vol. 419, pp. 803–7, 2002.

[4] M. Schultze, M. Fieß, N. Karpowicz, J. Gagnon, M. Korbman, M. Hofstetter, S. Neppl, A. L. Cavalieri, Y. Komninos, T. Mercouris, C. A. Nicolaides, R. Pazourek, S. Nagele, J. Feist, J. Burgdörfer, A. M. Azzeer, R. Ernstorfer, R. Kienberger, U. Kleineberg, E. Goulielmakis, F. Krausz, and V. S. Yakovlev, "Delay in photoemission," *Science*, vol. 328, no. 5986, pp. 1658–1662, 2010.

[5] P. B. Corkum, N. H. Burnett, and F. Brunel, "Above-threshold ionization in the long-wavelength limit," *Phys. Rev. Lett.*, vol. 62, pp. 1259–1262, 1989.

[6] A. H. Zewail, "Femtochemistry: Atomic-scale dynamics of the chemical bond using ultrafast lasers (nobel lecture)," *Angewandte Chemie International Edition*, vol. 39, no. 15, 2000.

[7] J. L. Krause, K. J. Schafer, and K. C. Kulander, "High-order harmonic generation from atoms and ions in the high intensity regime," *Phys. Rev. Lett.*, vol. 68, pp. 3535–3538, 1992.

[8] J. J. Macklin, J. D. Kmetec, and C. L. Gordon, "High-order harmonic generation using intense femtosecond pulses," *Phys. Rev. Lett.*, vol. 70, pp. 766–769, 1993.

[9] H. Geiseler, H. Rottke, N. Zhavoronkov, and W. Sandner, "Real-time observation of interference between atomic one-electron and two-electron excitations," *Phys. Rev. Lett.*, vol. 108, p. 123601, 2012.

[10] A. L. Cavalieri, N. Müller, T. Uphues, V. S. Yakovlev, A. Baltuška, B. Horvath, B. Schmidt, L. Blümel, R. Holzwarth, S. Hendel, M. Drescher, U. Kleineberg, P. M. Echenique, R. Kienberger, F. Krausz, and U. Heinzmann, "Attosecond spectroscopy in condensed matter," *Nature*, vol. 449, pp. 1029–1032, 2007.

[11] K. Klünder, J. M. Dahlström, M. Gisselbrecht, T. Fordell, M. Swoboda, D. Guénot, P. Johnsson, J. Caillat, J. Mauritsson, A. Maquet, R. Taïeb, and A. L'Huillier, "Probing single-photon ionization on the attosecond time scale," *Phys. Rev. Lett.*, vol. 106, p. 143002, 2011.

[12] J. Dahlström, D. Guénot, K. Klünder, M. Gisselbrecht, J. Mauritsson, A. ĹHuillier, A. Maquet, and R. Taïeb, "Theory of attosecond delays in laser-assisted photoionization," *Chem. Phys.*, vol. 414, pp. 53 – 64, 2013.

[13] J. Itatani, F. Quéré, G. L. Yudin, M. Y. Ivanov, F. Krausz, and P. B. Corkum, "Attosecond streak camera," *Phys. Rev. Lett.*, vol. 88, p. 173903, 2002.

[14] P. M. Paul, E. S. Toma, P. Breger, G. Mullot, F. Augé, P. Balcou, H. G. Muller, and P. Agostini, "Observation of a train of attosecond pulses from high harmonic generation," *Science*, vol. 292, p. 1689, 2001.

[15] D. Guénot, K. Klünder, C. L. Arnold, D. Kroon, J. M. Dahlström, M. Miranda, T. Fordell, M. Gisselbrecht, P. Johnsson, J. Mauritsson, E. Lindroth, A. Maquet, R. Taïeb, A. L'Huillier, and A. S. Kheifets, "Photoemission-time-delay measurements and calculations close to the 3s-ionization-cross-section minimum in ar," *Phys. Rev. A*, vol. 85, p. 053424, 2012.

[16] L. Keldysh, "Ionization in the field of a strong electromagnetic wave," *Sov. Phys. JETP*, vol. 20, pp. 1307–1314, 1965.

[17] G. S. Voronov and N. Delone, "Many-photon ionization of the xenon atom by ruby laser radiation," *Sov. Phys-JETP*, vol. 23, p. 54, 1966.

[18] P. Agostini, F. Fabre, G. Mainfray, G. Petite, and N. K. Rahman, "Free-free transitions following six-photon ionization of xenon atoms," *Phys. Rev. Lett.*, vol. 42, pp. 1127–1130, 1979.

[19] Y. Gontier and M. Trahin, "Energetic electron generation by multiphoton absorption," *J. Phys. B: Atomic and Molecular Physics*, vol. 13, no. 22, p. 4383, 1980.

[20] L. A. Lompré, A. L'Huillier, G. Mainfray, and C. Manus, "Laser-intensity effects in the energy distributions of electrons produced in multiphoton ionization of rare gases," *J. Opt. Soc. Am. B*, vol. 2, no. 12, pp. 1906–1912, 1985.

[21] R. R. Freeman, P. H. Bucksbaum, H. Milchberg, S. Darack, D. Schumacher, and M. E. Geusic, "Above-threshold ionization with subpicosecond laser pulses," *Phys. Rev. Lett.*, vol. 59, pp. 1092–1095, 1987.

[22] K. Burnet, F. C. Reed, and P. L. knight, "Atoms in ultra-intense laser fields," *J. phys. B: At. Mol. Opt. Phys.*, vol. 26, pp. 561–598, 1993.

[23] R. R. Freeman and P. H. Bucksbaum, "Investigations of above-threshold ionization using subpicosecond laser pulses," *J. Phys. B: At., Mol. and Opt. Phys.*, vol. 24, no. 2, pp. 325–347, 1991.

[24] D. Ruben, C. Bo, W. Garth, M. Harry, A. Keith, T. Sven, H. Peter, V. Lap, and A. G. Peele, "Diffractive imaging using a polychromatic high-harmonic generation soft-x-ray source," *J. Appl. Phys.*, vol. 106, p. 023110, 2009.

[25] L. DAO, S. TEICHMANN, B. CHEN, D. R., K. DINH, and H. P., "Extreme ultraviolet radiation for coherent diffractive imaging with high spatial resolution," *Science China Physics, Mechanics and Astronomy*, vol. 53, p. 1065, 2010.

[26] *Strong Field Laser Physics (Springer Series in Optical Sciences)*. Springer, 2008.

[27] A. M. Perelomov, V. S. Popov, and M. V. Terent'ev, "Ionization of atoms in an alternating electric field," *Sov. Phys. JETP*, vol. 23, pp. 924–934, 1966.

[28] M. V. Ammosov, N. B. Delone, and V. P. Kraĭnov, "Tunnel ionization of complex atoms and of atomic ions in an alternating electromagnetic field," *Sov. Phys. JETP*, vol. 64, pp. 1191–1194, 1986.

[29] P. B. Corkum, "Plasma perspective on strong field multiphoton ionization," *Phys. Rev. Lett.*, vol. 71, pp. 1994–1997, 1993.

[30] M. Quack and Frédéric, "Handbook of high-resolution spectroscopy," *John Wiley & Sons, Ltd*, vol. ISBN: 978-0-470-74959-3, 2011.

[31] U. Mohideen, M. H. Sher, H. W. K. Tom, G. D. Aumiller, O. R. Wood, R. R. Freeman, J. Boker, and P. H. Bucksbaum, "High intensity above-threshold ionization of he," *Phys. Rev. Lett.*, vol. 71, pp. 509–512, 1993.

[32] D. N. Fittinghoff, P. R. Bolton, B. Chang, and K. C. Kulander, "Observation of nonsequential double ionization of helium with optical tunneling," *Phys. Rev. Lett.*, vol. 69, pp. 2642–2645, 1992.

[33] T. Nubbemeyer, K. Gorling, A. Saenz, U. Eichmann, and W. Sandner, "Strong-field tunneling without ionization," *Phys. Rev. Lett.*, vol. 101, p. 233001, 2008.

[34] U. Eichmann, A. Saenz, S. Eilzer, T. Nubbemeyer, and W. Sandner, "Observing rydberg atoms to survive intense laser fields," *Phys. Rev. Lett.*, vol. 110, p. 203002, 2013.

[35] W. Becker, F. Grasbon, R. Kopold, D. Milošević, G. Paulus, and H. Walther, "Above-threshold ionization: From classical features to quantum effects," vol. 48 of *Advances In Atomic, Molecular, and Optical Physics*, pp. 35 – 98, Academic Press, 2002.

[36] M. Lewenstein, P. Balcou, M. Y. Ivanov, A. L'Huillier, and P. B. Corkum, "Theory of high-harmonic generation by low-frequency laser fields," *Phys. Rev. A*, vol. 49, pp. 2117–2132, 1994.

[37] K. Varjú, Y. Mairesse, B. Carré, M. B. Gaarde, P. Johnsson, S. Kazamias, R. López-Martens, J. Mauritsson, K. J. Schafer, P. Balcou, A. L'Huillier, and P. Salières, "Frequency chirp of harmonic and attosecond pulses," *J. Mod. Opt.*, vol. 52, pp. 379–394, 2005.

[38] H. Geiseler, *Untersuchung der Dynamik von Elektronenwellenpaketen in angeregten Zuständen atomarer Systeme*. PhD thesis, 2012.

[39] M. Lewenstein, P. Salières, and A. L'Huillier, "Phase of the atomic polarization in high-order harmonic generation," *Phys. Rev. A*, vol. 52, pp. 4747–4754, 1995.

[40] P. Salières, A. L'Huillier, and M. Lewenstein, "Coherence control of high-order harmonics," *Phys. Rev. Lett.*, vol. 74, pp. 3776–3779, 1995.

[41] Y. Mairesse, A. de Bohan, L. J. Frasinski, H. Merdji, L. C. Dinu, P. Monchicourt, P. Breger, M. Kovačev, R. Taïeb, B. Carré, H. G. Muller, P. Agostini, and P. Salières, "Attosecond synchronization of high-harmonic soft x-rays," *Science*, vol. 302, pp. 1540–1543, 2003.

[42] A. L'Huillier, K. J. Schafer, and K. C. Kulander, "Higher-order harmonic generation in xenon at 1064 nm: The role of phase matching," *Phys. Rev. Lett.*, vol. 66, pp. 2200–2203, 1991.

[43] J. Peatross, M. V. Fedorov, and K. C. Kulander, "Intensity-dependent phase-matching effects in harmonic generation," *J. Opt. Soc. Am. B*, vol. 12, pp. 863–870, 1995.

[44] A. Rundquist, C. G. Durfee, Z. Chang, C. Herne, S. Backus, M. M. Murnane, and H. C. Kapteyn, "Phase-matched generation of coherent soft x-rays," *Science*, vol. 280, pp. 1412–1415, 1998.

[45] C. Winterfeldt, C. Spielmann, and G. Gerber, " ***Colloquium*** : Optimal control of high-harmonic generation," *Rev. Mod. Phys.*, vol. 80, pp. 117–140, 2008.

[46] A. L'Huillier and P. Balcou, "High-order harmonic generation in rare gases with a 1-ps 1053-nm laser," *Phys. Rev. Lett.*, vol. 70, pp. 774–777, 1993.

[47] C. Kan, C. E. Capjack, R. Rankin, and N. H. Burnett, "Spectral and temporal structure in high harmonic emission from ionizing atomic gases," *Phys. Rev. A*, vol. 52, pp. R4336–R4339, 1995.

[48] E. Constant, D. Garzella, P. Breger, E. Mével, C. Dorrer, C. Le Blanc, F. Salin, and P. Agostini, "Optimizing high harmonic generation in absorbing gases: Model and experiment," *Phys. Rev. Lett.*, vol. 82, pp. 1668–1671, 1999.

[49] M. Böttcher, H. Rottke, N. Zhavoronkov, W. Sandner, P. Agostini, M. Gisselbrecht, and A. Huetz, "Reaction microscope study of near-threshold photo double ionization of xenon using high harmonics," *J. Phys. B: At. Mol. Opt.*, vol. 38, p. L389, 2005.

[50] M. Böttcher, H. Rottke, N. Zhavoronkov, W. Sandner, P. Agostini, M. Gisselbrecht, and A. Huetz, "Routes to multiphoton double ionization in combined extreme ultraviolet and infrared laser pulses," *Phys. Rev. A*, vol. 75, p. 033408, 2007.

[51] M. Böttcher, B. Manschwetus, H. Rottke, N. Zhavoronkov, Z. Ansari, and W. Sandner, "Interferometric long-term stabilization of a delay line: a tool for pump–probe photoelectron–photoion-coincidence spectroscopy on the attosecond time scale," *Appl. Phys. B: Lasers O.*, vol. 91, pp. 287–293, 2008.

[52] H. Geiseler, H. Rottke, G. Steinmeyer, and W. Sandner, "Quantum beat oscillations in the two-color-photoionization continuum of neon and their dependence on the intensity of the ionizing laser pulse," *Phys. Rev. A*, vol. 84, p. 033424, 2011.

[53] H. Igarashi, A. Makida, and T. Sekikawa, "Electron trajectory selection for high harmonic generation inside a short hollow fiber," *Opt. Express*, vol. 21, p. 18, 2013.

[54] P. Kruit and F. H. Read, "Magnetic field paralleliser for 2π electron-spectrometer and electron-image magnifier," *J. Phys. E: Sci. Instrum.*, vol. 16, p. 313, 1983.

[55] T. Tsuboi, E. Y. Xu, Y. K. Bae, and K. T. Gillen, "Magnetic bottle electron spectrometer using permanent magnets," *Rev. Sci. Instrum.*, vol. 59, pp. 1357–1362, 1988.

[56] A. M. Rijs, E. H. G. Backus, C. A. de Lange, N. P. C. Westwood, and M. H. M. Janssen, "'magnetic bottle spectrometer' as a versatile tool for laser photoelectron spectroscopy," *J. Electron Spectrosc.*, vol. 112, pp. 151–162, 2000.

[57] J. Ladislas Wiza, "Microchannel plate detectors," *Nuclear Instruments and Methods*, vol. 162, pp. 587–601, 1979.

[58] M. Baggash and H. Rottke, "Real-time tracking of two-electron dynamics in the ionization continuum of xe," *Phys. Rev. A*, vol. 91, p. 053403, 2015.

[59] U. Fano, "Effects of configuration interaction on intensities and phase shifts," *Phys. Rev.*, vol. 124, pp. 1866–78, 1961.

[60] H. Wang, M. Chini, S. Chen, C.-H. Zhang, F. He, Y. Cheng, Y. Wu, U. Thumm, and Z. Chang, "Attosecond time-resolved autoionization of argon," *Phys. Rev. lett.*, vol. 105, p. 143002, 2010.

[61] C. Ott, A. Kaldun, P. Raith, K. Meyer, M. Laux, J. Evers, C. H. Keitel, C. H. Greene, and T. Pfeifer, "Lorentz meets fano in spectral line shapes: A universal phase and its laser control," *Science*, vol. 340, pp. 716–720, 2013.

[62] B. Bernhardt, A. R. Beck, X. Li, E. R. Warrick, M. J. Bell, D. J. Haxton, C. W. McCurdy, D. M. Neumark, and S. R. Leone, "High-spectral-resolution attosecond absorption spectroscopy of autoionization in xenon," *Phys. Rev. A*, vol. 89, p. 023408, 2014.

[63] B. Doughty, L. H. Haber, C. Hackett, and S. R. Leone, "Photoelectron angular distributions from autoionizing $4s^1 4p^6 6p^1$ states in atomic krypton probed with femtosecond time resolution," *J. Chem. Phys.*, vol. 134, pp. 094307–1–11, 2011.

[64] B. Doughty, L. H. Haber, and S. R. Leone, "Pump-probe velocity-map imaging of autoionizing singly excited $4s^1 4p^6 np^1$ (n = 7,8) and doubly excited $4s^2 4p^5 5s^1 6p^1$ resonances in atomic krypton," *Phys. Rev. A*, vol. 84, pp. 043433–1–8, 2011.

[65] Z. X. Zhao and C. D. Lin, "Theory of laser assisted autoionization by attosecond light pulses," *Phys. Rev. A*, vol. 71, pp. 060702–1–4, 2005.

[66] W.-C. Chu and C. D. Lin, "Theory of ultrafast autoionization dynamics of fano resonances," *Phys. Rev. A*, vol. 82, pp. 053415–1–9, 2010.

[67] K. Codling and R. P. Madden *Phys. Rev. A*, vol. 4, no. 6, p. 2261, 1971.

[68] K. Codling and R. P. Madden *J. of Res. Nat. Bureau of Standards*, vol. 76A, no. 1, p. 1, 1972.

[69] A. Kramida, Y. Ralchenko, J. Reader, and N. A. Team, "Nist atomic spectra database (ver. 5.1)," 2013.

[70] V. L. Sukhorukov, I. D. Petrov, B. M. Lagutin, H. Schmoranzer, W. Kielich, P. V. Demekhin, and A. Ehresmann, "Photoionization of xe near 5s threshold: I. theoretical study of 5s–np resonance structure in 5$p-$ photoabsorption," *Eur. Phys. Jour. D*, vol. 59, pp. 151 – 159, 2010.

[71] J. E. Hansen and W. Persson, "Revised analysis of singly ionized xenon, xe ii," *Physica Scripta*, vol. 36, p. 602, 1987.

[72] M. Ukai, N. Terazawa, Y. Chikahiro, K. Kameta, N. Kouchi, Y. Hatano, and K. Tanaka, "Optical threshold excitation functions of xe 5s, 5p photoionization sattelites near the $5s^{-1}$ cooper minimum," *Phys. Rev. A*, vol. 45, p. R15, 1992.

[73] D. L. Ederer *Phys. Rev. A*, vol. 4, no. 6, p. 2263, 1971.

[74] D. L. Ederer *Phys. Rev. A*, vol. 14, p. 1936, 1976.

[75] M. Baggash and H. Rottke, "Phase differences in the photoemission from krypton in the fine-structure-split ionization channels $^2p_{3/2}$ and $^2p_{1/2}$," *Phys. Rev. A*, vol. 92, p. 013424, 2015.

[76] P. G. Burke, "R-matrix theory of atomic collisions: Application to atomic, molecular and optical processes," *Springer Series on Atomic, Optical, and Plasma Physics*, vol. 61, pp. ISBN–13: 978–3642159305, 2011.

[77] F. Schäfers, G. Schönhense, and U. Heinzmann, "Analysis of ar 3p6 and kr 4p6 photoionization from photoelectron-spin-polarization data," *Phys. Rev. A*, vol. 28, no. 2, pp. 802–814, 1983.

[78] E. P. Wigner, "Lower limit for the energy derivative of the scattering phase shift," *Phys. Rev.*, vol. 98, pp. 145–147, 1955.

[79] D. Guénot, D. Kroon, E. Balogh, E. W. Larsen, M. Kotur, M. Miranda, T. Fordell, P. Johnsson, J. Mauritsson, M. Gisselbrecht, K. Varjù, C. L. Arnold, T. Carette, A. S. Kheifets, E. Lindroth, A. L'Huillier, and J. M. Dahlström, "Measurements of relative photoemission time delays in noble gas atoms," *Journal of Physics B: Atomic, Molecular and Optical Physics*, vol. 47, p. 245602, 2014.

[80] M. Aymar and M. Crance, "Two-photon ionisation of atomic hydrogen in the presence of one-photon ionisation," *J. Phys. B: At. Mol. Opt. Phys.*, vol. 13, no. 9, p. L287, 1980.

[81] D. J. Kennedy and S. T. Manson, "Photoionization of the noble gases: Cross sections and angular distributions," *Phys. Rev. A*, vol. 5, pp. 227–247, 1972.

[82] J. M. Dahlström, A. L'Huillier, and A. Maquet, "Introduction to attosecond delays in photoionization," *Journal of Physics B: Atomic, Molecular and Optical Physics*, vol. 45, no. 18, p. 183001, 2012.

[83] M. Edwards, X. Tang, and R. Shakeshaft, "Multiphoton absorption by alkali-metal atoms above the ionization threshold. ii. further results on cs and rb ionization," *Phys. Rev. A*, vol. 35, pp. 3758–3767, 1987.

Acknowledgments

I would like to express my special gratitude and thanks to my advisor Dr. Horst Rottke for giving me the opportunity to carry out this research in his group, for his invaluable support throughout the PhD work and for always being open to discussions. The success of this research would not be possible without his enormous support.

I would like to thank Prof. Dr. Maria Krikunova for supporting my thesis as a first referee and guiding me through the process of submitting the thesis. I would also like to thank Prof. Dr. Emad Aziz for his willingness to be the second referee for my thesis and Prof. Dr. Janina Maultzsch for her support as a committee chairman for the promotion procedures.

I would like to thank Anton von Veltheim for the great memories at the MBI, Henri Zimmermann and Sebastian Eilzer for the wonderful times in the laboratory and for helping me with the laser system. Additionally, I am thankful for all the people and friends who assisted me. Your help is greatly appreciated.

Finally, special acknowledgement also goes to my parents and wife for their lifelong support and prayers.